

**Bioactivity and Surface Reactivity of
RF-sputtered
Calcium Phosphate Thin Films**

Bioactivity and Surface Reactivity of RF-sputtered Calcium Phosphate Thin Films

**Bioactiviteit en Oppervlaktreactiviteit van RF-gesputterde
Dunne Calciumfosfaat Films**

(met een samenvatting in het Nederlands)

PROEFSCHRIFT

TER VERKRIJGING VAN DE GRAAD VAN DOCTOR
AAN DE UNIVERSITEIT UTRECHT OP GEZAG VAN
DE RECTOR MAGNIFICUS, PROF. DR. W.H. GISPEN,
INGEVOLGE HET BESLUIT VAN HET COLLEGE VOOR
PROMOTIES IN HET OPENBAAR TE VERDEDIGEN OP
WOENSDAG 15 OKTOBER 2003 DES MIDDAGS TE 12.45 UUR

DOOR

Edwin van der Wal

GEBOREN OP 1 NOVEMBER 1972 TE BENNEKOM

PROMOTOREN: PROF. DR. F.H.P.M HABRAKEN
Faculteit Natuur- en Sterrenkunde
Universiteit Utrecht

PROF. DR. J.A. JANSEN
Faculteit Tandheelkunde
Katholieke Universiteit Nijmegen

COPROMOTOREN: DR. A.M. VREDENBERG
Faculteit Natuur- en Sterrenkunde
Universiteit Utrecht

DR. J.G.C. WOLKE
Faculteit Tandheelkunde
Katholieke Universiteit Nijmegen

The work described in this thesis was supported by the Technology Foundation STW, applied science division of NWO and the technology programme of the Ministry of Economic Affairs.



Druk: PrintPartners Ipskamp, Enschede.

ISBN 90-393-3491-9

Contents

1	Introduction	9
1.1	Biomaterials for bone replacement	9
1.1.1	Tissue reaction	10
1.2	Formation of the implant-bone interface	11
1.3	Bioceramics	12
1.4	Dissolution and formation of CaP crystals	14
1.4.1	Precursor phases	15
1.5	Deposition of CaP coatings	16
1.5.1	RF-sputter deposition of CaP coatings	16
1.6	Simulated body fluids	17
1.7	Aims and outline of this thesis	17
2	Materials and Methods	19
2.1	Introduction	19
2.2	Deposition	19
2.3	Immersion studies	22
2.3.1	SBF protocol	22
2.3.2	Immersion protocol	23
2.4	Analysis	23
2.4.1	IBA	23
2.4.2	Light scattering	26
2.4.3	XRD	29
3	Description of the CaP Coatings and Solutions	31
3.1	Introduction	31
3.2	Part I: RF-sputter deposited CaP thin films	31

3.2.1	Graded Ca/P ratios	33
3.2.2	Coating integrity	35
3.3	Part II: Thermodynamics of simulated body fluids	37
4	Dissolution of As-deposited CaP Coatings	41
4.1	Introduction	41
4.1.1	Diffusion	42
4.2	Experimental considerations	43
4.2.1	Immersion studies	43
4.2.2	Coating application	44
4.3	Static dissolution of as-deposited coatings	44
4.4	Diffusion	45
4.5	Discussion	45
4.6	Conclusions	47
5	Precipitation on Heat-treated CaP Coatings	49
5.1	Introduction	49
5.1.1	Classical nucleation theory	50
5.2	Experimental considerations	51
5.2.1	Scanning electron microscopy	52
5.3	Heat-treated coatings in SBFs	52
5.3.1	Formation and growth of a precipitate	52
5.3.2	Part I: the induction period	57
5.3.3	Part II: the growth period	66
5.4	Discussion	68
5.5	Conclusions	71
6	Adsorption	73
6.1	Introduction	73
6.2	Adsorption and the electrical double layer	74
6.2.1	Reprecipitation	76
6.3	Experimental considerations	77
6.3.1	Setup of the experiments	77
6.3.2	LEIS	79
6.3.3	Radionuclides	79
Calibration and quenching	80	
6.3.4	Coating application	81
6.4	Adsorption	82
6.5	Desorption and reprecipitation	87
6.6	Discussion	90
6.7	Conclusions	93

Contents	7
7 Application in a Cell Model	95
7.1 Introduction	95
7.1.1 Introduction to osteogenesis	96
7.2 Materials and Methods	98
7.2.1 Cell culture	98
7.2.2 Cell proliferation	98
7.2.3 Cell differentiation	99
7.2.4 Mineralization	99
7.2.5 Scanning electron microscopy	100
7.2.6 Coating application	100
7.2.7 Statistical treatment	100
7.3 Part I: Biocompatibility	101
7.3.1 Setup of the study	101
7.3.2 Results of the biocompatibility study	103
7.4 Part II: Effect of prenucleation	109
7.4.1 Setup of the study	109
7.4.2 Results of the prenucleation study	110
7.5 Discussion	115
7.6 Conclusions	118
A Thermodynamics of Dissolution and Precipitation of Sparingly Soluble Salts	119
Bibliography	123
Summary	135
Samenvatting	139
Dankwoord	143
Curriculum Vitae	145
Notations	147

Introduction

1.1 Biomaterials for bone replacement

The increase in life span of people, which, for example, in The Netherlands has doubled since 1900 [1], is accompanied by the progressive deterioration of the skeletal system, like hip and knee joints. Due to evolving medical knowledge and increase in wealth, annually over a million of joint replacement procedures are performed worldwide [2].

For the purpose of joint replacements, synthetic materials have to be used, that possess suitable mechanical and wear properties, and show optimal tissue response. Artificial bone substitutes have been constructed from many sorts of metals, ceramics, and polymers [3]. The required material properties depend on the function of the implant. For example, in a hip prosthesis the shaft of a femoral stem must have good bone-bonding properties, in contrast to temporary pins used for fracture fixation. We focus on materials intended to form a strong and stable bone contact, like a tooth implant or the shaft of the femoral stem in a hip prosthesis mentioned above. For these long-term implants, a strong and reliable interface is essential to prevent loosening of the implant and loss of functionality.

Calcium phosphate (CaP) ceramics form the major inorganic constituent of bone, and are therefore an obvious candidate to be used as a bone-bonding biomaterial. Indeed, CaP ceramics are known to form a strong and continuous interface with bone. Major drawback of CaPs is their limited fracture toughness and brittleness. By application of CaP as thin films, the advantage of a good tissue response of the CaP can be combined with suitable mechanical properties of the bulk material.

The formation of the bone material interface involves numerous and complex pro-

cesses, partly protein- and cell-driven and partly controlled by inorganic, surface-solution interactions. This thesis describes the physicochemical processes involved in the formation of a stable interface between thin films of CaP and a bone-forming environment. These processes include dissolution of coating species, adsorption and crystal formation of CaP, and structuring of the interface. For the deposition of these CaP thin films, radio frequency magnetron sputtering is used. This technique is suitable for the production of thin, dense, and well adhering coatings.

In the remaining of this section, an overview is given of the bone-bonding properties that are required for a bone-substituting material. A classification for the biocompatibility of a material is introduced.

Further, in this chapter the principal concepts of bone-bonding are treated. Both cell-driven processes and physicochemical aspects are being discussed. Then, the importance of bioceramics is explained, in particular the use of calcium phosphates. Also the application of CaP as a thin film material is treated.

Thereafter, an overview is given of the dissolution and precipitation behavior of CaP in water-based solutions. To isolate the effects that do not involve cells or proteins, solutions are introduced that mimic the inorganic part of physiological fluids.

Finally, the aims of this thesis are formulated.

1.1.1 Tissue reaction

Besides mechanical and stability issues, an important property of a biomaterial is the tissue response upon implantation. Depending on the function of the implant, this determines the biocompatibility of a material. For a load-bearing bone-substituting material, it is essential to have a solid bone contact.

Various systems have been adopted to classify non-toxic material-tissue reactions, e.g., by Hench [4] and Black [5]. The classification we adopted in this work was proposed by Osborn and Newesely [6, 7], and is presented in table 1.1. This classification was designed to group bone replacement materials according to their bony tissue response. Note that all classifications refer to *in vivo* tissue reactions. Much effort has

Degree of compatibility	Characteristics of bony tissue.
Biotolerant	Implants separated from adjacent bone by a soft tissue layer along most of the interface: distance osteogenesis.
Bioinert	Direct contact to bony tissue: contact osteogenesis.
Bioactive	Bonding to bony tissue: bonding osteogenesis.

Table 1.1: Biocompatibility classification as proposed by Osborn and Newesely. Also tissue reaction has been indicated.

been made to translate the classifications above to *in vitro* measures. In this context it is more appropriate to address the various types of cell behavior as cytocompatibility.

Thus, we see that an essential prerequisite for bioactivity is the bone-bonding ability of the material. During the second consensus conference on definitions in biomaterials it was decided that bone-bonding is the establishment, by physicochemical processes, of continuity between implant and bone matrix [8].

It is observed that for many materials that show a strong bone material interface after implantation, an interfacial carbonate apatite is present, also referred to as a *biological apatite*. This layer binds to both the implant and bone matrix. Examples of these materials are calcium phosphate, some glass ceramics, and (some) surface activated silica and titania. In testing the bioactive potential of materials, this relation is often inverted, and the property of a material to allow the formation of a tightly bonded CaP layer *in vitro* is used to identify promising bioactive materials.

It was observed that biotolerant materials (e.g., most metals), that exhibit distant osteogenesis, i.e., the formation of bone *towards* the material, often show the formation of fibrous layer of soft tissue between bone and implant. This layer can be up to hundreds of microns thick. It is this layer that is thought to be responsible for a poor bone implant adherence. The formation of soft tissue is also enhanced by mechanical friction between implant and tissue.

1.2 Formation of the implant-bone interface

Before exploring the details of the processes leading to formation of the implant-bone interface, we first give a short background on the structure and composition of bone (refer to [9] for further reading).

Bone is a supportive tissue and is composed of a carbonate-containing calcium apatite (~43 weight percent) and type I collagen (~36 weight percent). Further, it contains about 14 percent water. Two types of bone can be distinguished, cortical bone, which is constructed of ~90 percent solid bone tissue, and trabecular bone which is spongy and contains 80 percent marrow filled voids. Bone is a dynamic tissue subject to constant remodeling, i.e., deposition by osteoblast activity and subsequent resorption by osteoclasts.

When a surface is introduced into bone tissue, a sequence of complex interactions takes place [4, 9–12]. Some of these interactions were schematically outlined in figure 1.1. In the first seconds, ions and proteins from the surrounding fluid are adsorbed on the surface [14, 15]. Various surface properties govern the adsorption process, like morphology, composition, energy, and charge. These properties determine not only the concentration of adsorbed proteins but also their functionality. Since proteins act as contacts for the attachment of cells, selective adsorption of certain proteins may significantly alter cell behavior. In addition, at the same time the surface can also be altered just by the physicochemical interaction between the (ionic) surface and the adjacent solution. The surface can (partly) be dissolved or restructured, or crystals can be

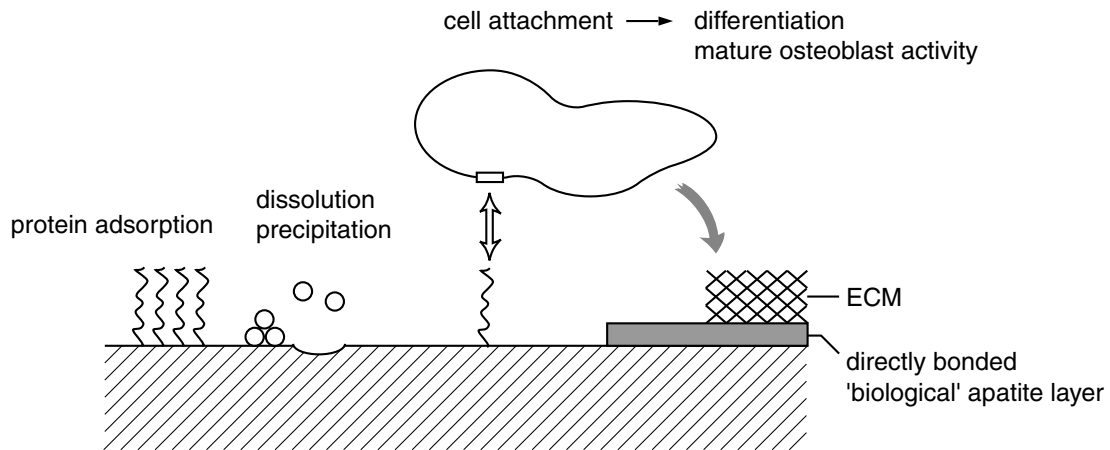


Figure 1.1: Some of the surface processes relevant to the formation of the bone material interface. The surface interacts with the ionic solution, proteins adhere to the surface, and cells interact with the adsorbed proteins. After differentiation, mature osteoblasts produce the extracellular matrix (ECM). Adapted from [10, 13].

formed from the solution. Both processes compete for available surface binding sites.

After protein adsorption, a cascade of reactions recruit osteoblasts to the implant. Communication of the cell with the adjacent surface proceeds via receptors in the cell membrane, the so-called integrins. The integrins bind to the adhesive proteins on the surface and thus connect the cell to the surface.

Cells attached to the surface spread within hours. Important for good cell spreading are surface topology and surface charge. Cells may now proliferate or migrate. Given the right stimuli, osteoblasts can now differentiate to active, extracellular matrix (ECM) forming mature osteoblasts. The extracellular matrix is a network of collagen fibrils, proteins, and polysaccharides that can be calcified, to form the connective framework of the bone tissue. A typical timescale for this process to start ranges from days to weeks. The ECM provides cell anchorage and supports the apposition of CaP, giving strength to the newly formed bone tissue.

It is important to realize that interfacial conditions, especially in the vicinity of attached cells, may differ considerably from bulk fluid conditions. Ion concentrations, pH, and diffusive properties may all deviate substantially.

1.3 Bioceramics

An important class of bone-substituting biomaterials are bioceramics, like Al_2O_3 , ZrO_2 , CaP, and glass ceramics. As mentioned earlier, advantage of these materials over e.g. most metals is their corrosion resistance. In addition, extensive research has shown unambiguously that some of these bioceramics, like some of the CaP phases

are bioactive. Also some glass ceramics (mixtures of SiO_2 , CaO , and P_5O_5) can be bioactive.

The application of CaPs is straightforward, since the main inorganic constituent of bone is a poorly crystallized, Na-, Mg-, and CO_3 -containing calcium apatite. In table 1.2 most of the CaP phases relevant for biomineralization are listed together with acronyms, formulas, and Ca over P ratios. A short description of some of these phases is given below, details can be found in [16–18].

Name	Acronym	Formula	Ca/P
monocalcium phosphate monohydrate	MCPM	$\text{Ca}(\text{H}_2\text{PO}_4)_2 \cdot \text{H}_2\text{O}$	0.5
monocalcium phosphate anhydrate	MCPA	$\text{Ca}(\text{H}_2\text{PO}_4)_2$	0.5
dicalcium phosphate dihydrate	DCPD	$\text{CaHPO}_4 \cdot 2\text{H}_2\text{O}$	1.0
dicalcium phosphate anhydrate	DCPA	CaHPO_4	1.0
calcium pyrophosphate	pyro	$\text{Ca}_2\text{P}_2\text{O}_7 \cdot 2\text{H}_2\text{O}$	1.0
octacalcium phosphate	OCP	$\text{Ca}_8(\text{HPO}_4)_2(\text{PO}_4)_4 \cdot 5\text{H}_2\text{O}$	1.33
tricalcium phosphate	TCP	$\text{Ca}_3(\text{PO}_4)_2$	1.5
amorphous calcium phosphate	ACP	$\text{Ca}_x(\text{PO}_4)_y \cdot n\text{H}_2\text{O}$	1.2-2.2
calcium deficient hydroxyapatite	CDHA	$\text{Ca}_{10-x}(\text{HPO}_4)_x(\text{PO}_4)_{6-x}(\text{OH})_{2-x}$	1.5-1.67
hydroxyapatite	HAP	$\text{Ca}_{10}(\text{PO}_4)_6(\text{OH})_2$	1.67
tetracalcium phosphate	TTCP	$\text{Ca}_4(\text{PO}_4)_2\text{O}$	2.0

Table 1.2: List of CaP phases most relevant for biomaterials and biomineralization. Ca/P refers to the Ca over P ratio, a measure widely used in the field of CaP bioceramics to address compositional differences.

MCPM, MCPA Crystallize from very acidic solutions only. The anhydrous form is formed at temperatures above 100°C .

DCPD, DCPA DCPD (brushite) has been proposed as intermediate phase in precipitation reactions. It can be formed at pH 6 and 37°C . DCPA is the anhydrous form of DCPD and is formed by drying DCPD or by precipitation from solutions above 60°C .

OCP OCP has also been proposed as an intermediate reaction product in the precipitation of CaP from oversaturated solutions. It can be formed similar to DCPD but at somewhat lower pH.

HAP Most stable CaP phase, end-product of precipitation reactions under physiological composition, pH, and temperature.

TCP TCP can not be directly obtained from aqueous solutions. It is somewhat more soluble than HAP, and is being used as a bioceramic, pure or mixed with HAP (biphasic calcium phosphate). Both α -TCP and β -TCP are high temperature phases, only formed above 800°C .

pyro, TTCP Can not be precipitated from calcium (ortho)phosphate solutions. Pure phases have only limited biocompatibility.

Besides the observed formation of a tightly bonded biological apatite layer, and their *osteopromotive* properties (able to guide bone along their surface), some CaP surfaces, some in combination with growth factors or pre-seeded cells, also proved to be *osteopromotive*. That is, they induce the formation of bone on their surface even when implanted in ectopic (outside bone tissue) locations.

1.4 Dissolution and formation of CaP crystals

As mentioned, important aspects of a CaP surface are its dissolution and precipitation behavior upon immersion in body fluids. In this section we give an outline of some of the research that has been done to describe the dissolution and precipitating properties of CaPs. Most of the basic research has been conducted on fastly stirred powder suspensions. It is important to note that the mechanisms observed in powder experiments are not necessarily the same for thin films.

In the seventies and early eighties, extensive work was done to describe the dissolution of CaPs in water based solutions. Depending on the experimental conditions, transport controlled models were developed, or surface controlled models. Higuchi et al. proposed a diffusion-limited model in combination with a two-site binding model [19–21] for HAP dissolution. This model is valid only at low stirring rates and high over-/undersaturation.

Christoffersen et al. [22–26], were the first to propose a polynuclear dissolution model for fastly stirred HAP powder. The rate-limiting step is thought to be surface diffusion of ions to reach a kink step. This model was shown to be valid for $5.0 < \text{pH} < 7.2$.

Also for HAP powders, Thomann, Voegel, Gramain, and coworkers [27–32], observed a considerable decrease in dissolution rate after several minutes. This was explained by the accumulation of Ca in the diffusive layer during dissolution. The dissolution rate is hampered by diffusion of Ca and/or PO_4 through this layer.

Nancollas and coworkers treated the dissolution of some other CaP phases in detail, like CO_3 -HAP [33], OCP [34–36], tooth-enamel [37–39], DCPD [40–42]. They used a (dual) constant composition method which is essential when studying the dissolution of powders. Two ion-selective electrodes are coupled to a Ca and a PO_4 reservoir to guarantee a constant composition during the experiment. No buffers can be used with this technique, and the effective dissolution area must be large enough to obtain a detectable signal. Different dissolution mechanisms were found to be responsible for the dissolution of the various CaP phases. Again, the description of the process varied as a result of the hydrodynamical conditions and the over/under-saturation. Although this method was occasionally used for a plasma sprayed HAP coating [43], the majority of this research was done on CaP suspensions.

Concluding, the mechanism controlling the dissolution rate depends on the exact transport properties of the experiment. Results found for CaP powders may be different for thin films. A review of different dissolution models can be found in reference [18].

From oversaturated Ca- and PO_4 -containing solutions CaPs can be nucleated both homo- and heterogeneously [44–49]. This process has mostly been described in terms of classical nucleation theory. Models for HAP growth have been proposed by, amongst others, Christoffersen and Nancollas [50, 51].

Important inhibitors of CaP nucleation and growth are Mg [52–55], CO_3 [56], proteins and other organic additives [26, 57–59], and metals like Zn, Cd, and Pb.

1.4.1 Precursor phases

As stated in section 1.3, the thermodynamically most stable CaP phase is HAP. It is expected that after precipitation of CaP from oversaturated solutions (Ca/P ratio of ~ 1.6) eventually HAP is formed (at pH 7 and temperatures of 20–40°C). However, in numerous studies it was found that intermediate phases were formed [60]. Kemenade et al. showed convincingly that the formation of HAP is always preceded by the formation of at least one precursor phase [61, 62]. The order in which the precursor phases were observed was according to Ostwald's rule of stages. ACP, DCPD, OCP, and CDHA have been proposed as precursor phases in the formation of HAP. The number of precursor phases, and the exact reaction path depend on the temperature, pH, supersaturation, the presence of crystal seeds or inhibitors, and the hydrodynamics. Observed reaction paths are plotted in figure 1.2.

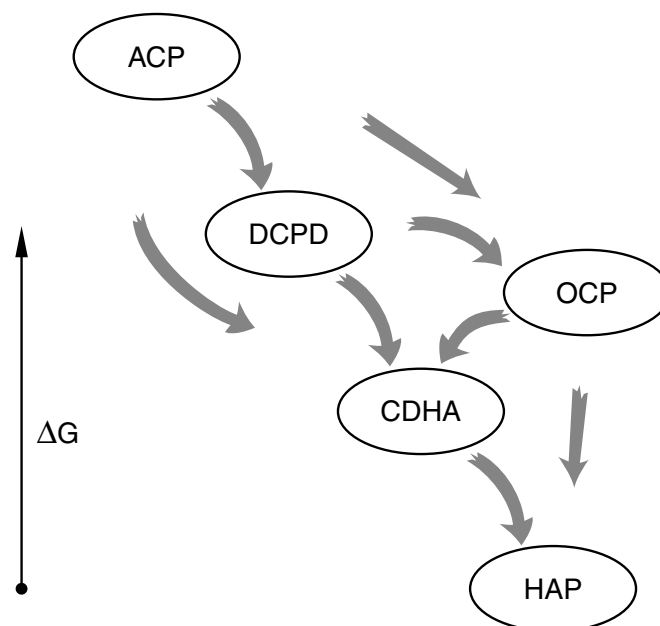


Figure 1.2: Observed reaction paths in the precipitation of HAP from oversaturated CaP solutions. The followed path depends on temperature, pH, supersaturation, presence of seeds/inhibitors, and hydrodynamics. Adapted from [63].

1.5 Deposition of CaP coatings

Calcium phosphate ceramics are often not very suitable in load-bearing applications due to their brittleness. Coating of a metal alloy by CaP combines the advantage of the strength and fracture-toughness of the metal with the biocompatibility of CaP.

In the past decades almost all known deposition techniques have been applied to deposit CaP coatings. Plasma spray deposition (see amongst others [43, 64–70]) is by far the most popular technique due to its simplicity and versatility. Another advantage of plasma spray deposition is a relative high deposition rate as compared to other techniques (up to microns per minute). A disadvantage of this technique is the heterogeneity in crystal phase and composition of the coating.

Other widely used deposition techniques include electrophoretic deposition [71–74], ion beam (assisted) deposition [75–77], pulsed laser deposition [78–81], sol-gel deposition [82, 83], and biomimetic deposition [84–87]. Of course, all techniques have their benefits and limitations. Coatings have been deposited on every material that has been suggested as a biomaterial, especially on Ti and its alloys. In this work we have used radio frequency (RF) magnetron sputter deposition to produce thin films of CaP coatings. RF-sputtering is used to produce thin films of conductive and isolating target materials in many fields of research and industry [88, 89].

1.5.1 RF-sputter deposition of CaP coatings

Jansen et al. [90] were the first to exploit the benefits of RF-sputter deposition for the production of thin, dense, and well-adhering CaP coatings on Ti substrates. These coatings were shown to be bioactive both *in vivo* and *in vitro* [90–93]. Extensive research has been done to relate the coating properties to the deposition parameters [94–97]. Recently, these coatings have also successfully been applied on polymers [98]. RF-sputter deposition has some clear advantages compared to other deposition techniques like plasma spraying. It is possible to deposit thin (~ 1 nm), uniform, dense, and well-adhering CaP coatings at reasonable temperatures ($< 100^\circ\text{C}$ substrate temperature). Since the coating is formed by sputtering atoms or small clusters of atoms, the coating structure is much more homogeneous in structure and composition when compared to plasma sprayed coatings, making them very suitable for research purposes. Further, the technique provides good control over coating thickness, composition, and to some extent, over coating structure.

Cell response to RF-sputtered CaP thin films were reported by ter Brugge et al. [93, 99]. They studied differences in expression of various osteogenic markers and expression of integrins between RF-sputtered CaP coatings on titanium and uncoated titanium. Osteocalcin levels were found to be higher for coated titanium than for uncoated titanium.

1.6 Simulated body fluids

To test biomaterials for their bioactive potential, Kokubo et al. studied the calcification behavior of materials in inorganic solutions mimicking physiological conditions [100–102]. As hypothesized by Ducheyne [103], the formation of a directly bonded biological apatite might be indicative of possible bioactivity. For this purpose, Kokubo introduced a solution with ion concentrations similar to human blood plasma (HBP), designated simulated body fluid (SBF). Ion concentrations can be found in table 2.1 in section 2.3.1.

For CaP coatings deposited with various techniques, both the dissolution properties [96, 104–107] and the precipitation properties [56, 67, 70, 108] were investigated in SBFs.

Nowadays, simulated body fluids based on the formulation by Kokubo are used routinely to test the bioactive potential of materials [67, 70, 96, 105–107, 109–122]. The time needed to cover the surface and the abundance of CaP crystals are thought to be indicative of bone-bonding properties *in vivo*.

1.7 Aims and outline of this thesis

As outlined in section 1.2 the formation of the interface between a surface and a bone-forming environment is controlled by biochemical processes on the one hand, such as interaction of proteins and cells with the surface. On the other hand, interaction of the CaP coating with adjacent solution also alters the structure and composition at the interface. Especially the bonding between the ECM and the coating is crucial to obtain a good bone material contact.

It is not our aim to reduce the expected bioactivity of RF-sputtered CaP thin films to a set of physicochemical processes at the coating interface. However, it is of utmost importance to recognize the relative contribution of such processes during the early interaction of these CaP coatings with a bone-forming environment. We describe the processes relevant for the construction of the interface between the RF-sputtered CaP thin film and a physiological environment in terms of fundamental physicochemical processes. These processes include dissolution of the coating, thermodynamics of the adjacent fluids, and the formation of CaP crystals at the coating interface.

Simulated body fluids are used to investigate the dissolution and precipitation properties of CaP thin films. We investigate the interface in the presence of rat bone marrow cells that are stimulated to differentiate towards bone-forming cells. An effort is made to find similarities between the results obtained from studies in SBF and the cell-culture studies.

Finally, we study the relationship between the formation of CaP crystals at the coating interface and the cytocompatibility, and couple this to the bioactivity of the material.

The outline of this thesis is as follows. In chapter 2 some background is presented

on the techniques used throughout this work, such as details on the RF-sputter deposition technique and ion beam analysis. In chapter 3 the properties of the sputtered CaP coatings are investigated. It is established how the coating composition can be controlled by varying deposition parameters, and what the effect of a heat treatment on the coating structure is. In this chapter also the thermodynamic properties of the simulated body fluids are addressed. In chapter 4 the dissolution properties of the as-deposited coatings are studied, followed by the precipitation of CaP crystals from the solution on heat-treated coatings in chapter 5. Here we investigate the dissolution and precipitation behavior under simulated physiological conditions. We study the effect of coating structure, coating composition, diffusion properties, and temperature on the nucleation and growth of CaP crystals and the dissolution of the coating. Also sedimentation aspects from the solutions on the coating surface are addressed. The formation of CaP crystals starts with the adsorption of ions on the surface; in chapter 6 the adsorptive properties of the CaP coatings are investigated in relation to their ability to nucleate CaP crystals. The effect of coating composition on the composition of the adsorptive layer is studied. Also desorption and supersaturation of the diffusive layer by coating species are investigated. Finally, in chapter 7 the formation of the CaP coating interface is studied in a cell-culture model using rat bone marrow cells. Here, the cytocompatibility is compared to other materials, which can again be related to the concepts of biocompatibility as described in table 1.1. The concepts treated in chapter 5 are applied and the relative contribution to the formation of the cell-culture/coating interface is determined.

Materials and Methods

2.1 Introduction

In this chapter experimental details are given for the deposition of the CaP coatings and the preparation of the simulated body fluids. Also the analysis techniques that are used throughout this thesis will be described. When deemed necessary, background is provided on some of the techniques.

2.2 Deposition

RF magnetron sputtering

CaP thin layers were deposited using radio frequency (RF) magnetron sputtering. The technique is based on the ionization of a gas (often Ar) at low pressure by a radio frequent voltage, thus generating a plasma. Some of the energetic ions transfer their kinetic energy to the target material, causing ejection of target atoms and heating. Some of the ejected atoms make their way to the substrates on the substrate holder, and may be deposited at the surface of the growing film.

By applying a radio frequent voltage also insulating materials can be sputtered. Compared to DC-sputtering problems with charging of both target and substrates can be overcome. In a typical sputtering setup, a net negative charge is built up on the target which acts as the cathode. The anode is the substrate holder which is usually grounded.

The efficiency of the sputter process can be dramatically improved by the use of

a magnetron, a magnet configuration under the target, resulting in the confinement of electrons in a region near the surface. This increases the ionization probability of the gas near the surface and therefore improves the sputter-rate of target material, resulting in a so-called *racetrack* along the surface. The sputtering of target material is atomically or in small clusters of atoms. Generally, this technique is able to produce thin, homogeneous, and dense coatings with a good adhesion. Drawbacks are the relatively low deposition rate (e.g., compared to plasma spraying) and the need for vacuum equipment.

Equipment

In figure 2.1 we see a schematic outline of the used deposition equipment, an Edwards High Vacuum ESM100. The sputter chamber is cylindrical (diameter 32 cm), containing two sputter targets, a sample holder, shutters for both targets, and a pressure feedback gas-inlet control. An oil diffusion pump is connected to the sputter chamber to maintain a base pressure of $1 \cdot 10^{-5}$ mbar. Both targets and substrate holders are water-cooled. A matching network is used to couple the 13.56 MHz signal of the power supply in the plasma. The target shielding is grounded, as well as the sample holder. The sample holder can be rotated at 30 revolutions per minute.

Coatings

For the coatings produced in the following chapters, a sputter power of 200-600 W was used at an Ar pressure of $5 \cdot 10^{-3}$ mbar. The sample holder was rotated. For most depositions, granulated hydroxyapatite was used as a target material. Silicon (100) strips of 2 times 8 cm² were used as a substrate material. As explained in section 2.4.1, for the analysis of Ca and P with ion beam techniques it is convenient to use a light substrate material.

To obtain CaP coatings with different compositions, different materials were used for both targets (e.g., Ca₂P₂O₇, and CaO). By applying a different sputter power to the targets, Ca/P ratios can be tuned to the desired value.

As illustrated in figure 2.1, the Si sample strips were mounted radially on the sample holder. Rotation of the sample holder guaranteed a constant thickness and composition over the width of the strips and among different strips. At the bottom of the figure we see how the strips were divided in separate samples of 1 cm². From each adjacent pair of samples, one was saved as a reference. Substrate temperatures did not exceed $\sim 100^\circ\text{C}$.

To crystallize the CaP coatings, the coated strips were subjected to a 30 minutes post heat treatment at 650°C . This should suffice to crystallize most of the CaP in an apatite structure without significant presence of high temperature phases like β -TCP or CaO [95]. Annealing was done in an Ar flushed tube furnace.

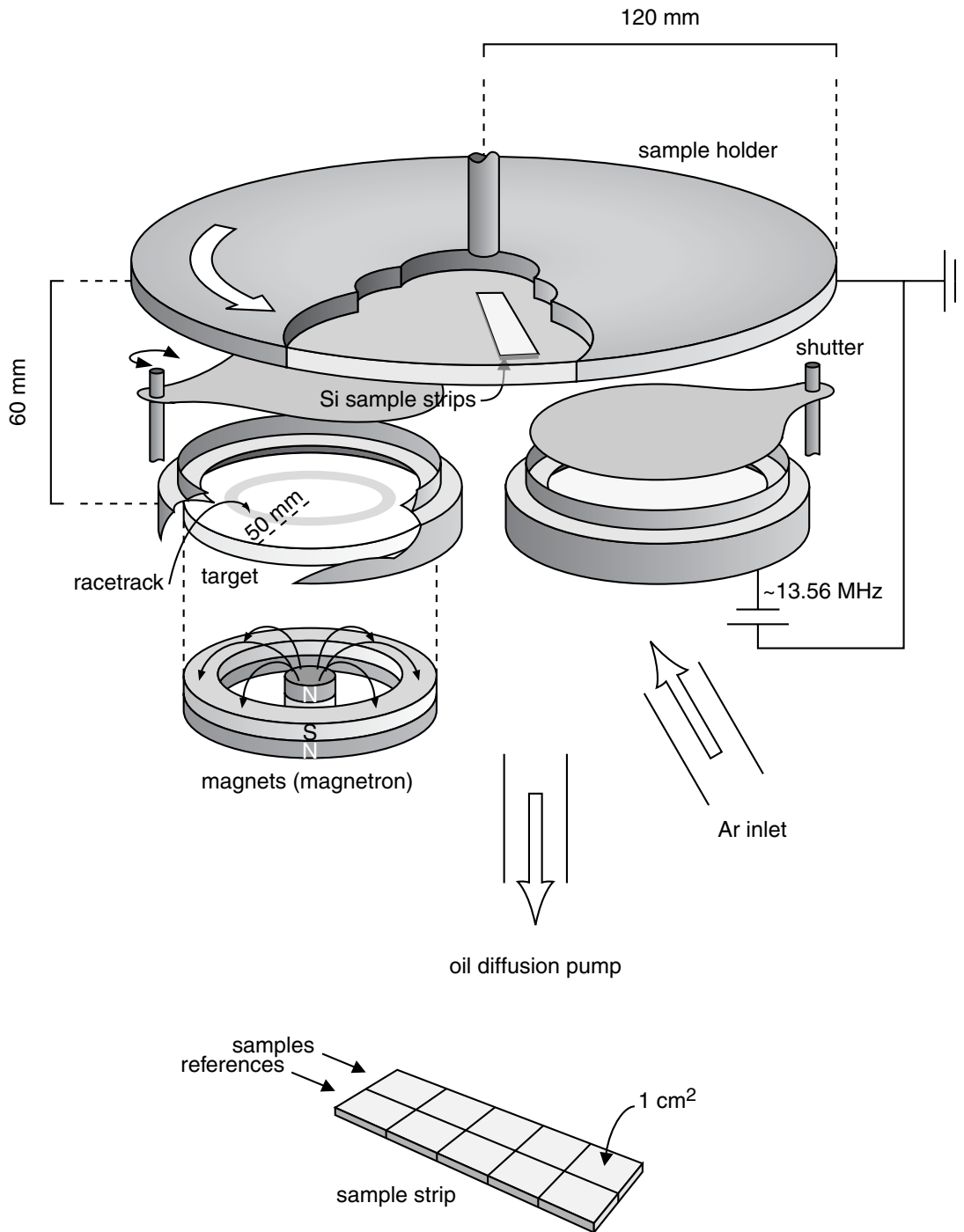


Figure 2.1: A schematic outline of the Edwards High Vacuum ESM100 sputter deposition system. Characteristic distances are indicated. Below a sample strip is shown.

2.3 Immersion studies

2.3.1 SBF protocol

The protocol for the preparation of simulated body fluid (SBF or SBF₁) was adopted from Kokubo [100, 101]. Ion concentrations for SBF are listed in table 2.1. Also

Species	Solutions						
	HBP	SBF ₁	SBF _x	Ca-stock	P-stock	SBF ₁ -s	α -MEM
Na	142.	142.	142.	684.	735.	1420.	143.6
K	5.0	5.0	$3.0 + 2 \cdot x$	-	70.	30.	5.4
Ca	2.5	2.5	$2.5 \cdot x$	50.	-	-	1.8
Mg	1.5	1.5	1.5	15.	-	15.	0.81
Cl	103.	148.	$143. + 2 \cdot x$	814.	714.	1428.	125.
CO ₃	27.	4.2	4.2	-	42.	42.	26.
PO ₄	1.0	1.0	$1.0 \cdot x$	-	20.	-	1.0
SO ₄	0.5	0.5	0.5	-	5.0	5.0	0.81

Table 2.1: Concentrations of ionic species in Human Blood Plasma (HBP) and Simulated Body Fluid (SBF) of different Ca and PO₄ concentrations. Concentrations are in mM.

more strongly concentrated SBFs were derived from SBF₁ by increasing Ca and PO₄ concentrations congruently (SBF_x). Here, concentrations of the background electrolyte (NaCl) were kept constant. Concentrations of other ions not directly related to the free energy difference remain the same (refer to section 3.3). From the oversaturated SBFs, especially SBF with twice the Ca and PO₄ concentrations (SBF₂) are used throughout this thesis.

To facilitate fast production of SBFs, for most experiments concentrated stock solutions were used. Ion concentrations for the stock solutions are also listed in table 2.1. A cation stock was prepared (Ca-stock), an anion-stock (P-stock), and a SBF₁ supplement stock (SBF₁-s). All stock solutions were filtered (pore size 0.45 μ m) and stored at $\approx 5^\circ\text{C}$. New stock solutions were made regularly.

For all solutions reagent grade chemicals were used, i.e., NaCl, KCl, CaCl₂·2H₂O, MgCl₂·6H₂O, NaHCO₃, K₂HPO₄, and Na₂SO₄·10H₂O. A buffer solution of 50 mM tris (tris(hydroxymethyl)-aminomethane, H₂NC(CH₂OH)₃) in ultra pure water (Millipore) was made, all chemicals were dissolved under continuous stirring. pH values were set to 7.4. For the stock solutions, pH values were set to result in a pH 7.4 solution after mixing and diluting.

For most experiments, SBFs were mixed from concentrated stock solutions.

2.3.2 Immersion protocol

Most of the SBFs used in this thesis were prepared from stock solutions as described in section 2.3.1 immediately prior to use. Unless stated otherwise, first the PO_4 -stock was diluted with water and stirred, followed by the dropwise addition of the Ca-stock, also under continuous stirring. pH values were checked and adjusted to 7.4 when necessary. Solutions were filtered through a $0.45\ \mu\text{m}$ pore size syringe filter. When prepared and stored dust free, solutions up to SBF_2 proved to be stable for days. If dust particles are present in the solution, SBF_2 shows homogeneous precipitates visible to the eye after about 1 day at room temperature.

SBF_1 was obtained by mixing one part of the Ca-, P-, and SBF_1 -s stocks and 17 parts of water (so: 50 ml of Ca-stock + 50 ml of P-stock + 50 ml of SBF_1 -s stock can be diluted to 1 liter SBF_1). SBF_2 can be made from equal amounts of Ca- and P-stock at 5 fold dilution (so: 50 ml of Ca-stock + 50 ml of P-stock can be diluted to 500 ml SBF_2). SBF solutions were filtered and stored for a maximum of two days at $\approx 5^\circ\text{C}$. No solutions were used that showed the presence of homogeneous precipitates.

Immersion was done in 6-well polystyrene plates using 10 ml solution. This solution volume is enough to guarantee constant bulk solution composition during the experiments. After immersion samples were rinsed with water, and dried to air. No homogeneous precipitates were found after the immersion period, nor precipitation on the plates. In none of the experiments pH values changed significantly.

2.4 Analysis

2.4.1 IBA

Ion beam analysis (IBA) techniques can be used as depth-resolved, mass dispersive tools to determine elemental coverages of thin layers (up to a few micron) with an excellent sensitivity. These techniques rely on the elastic scattering of MeV projectile ions with atoms in the sample layer. In-depth treatment of these techniques can be found in [123–125].

Two complementary techniques were applied in this thesis, Rutherford backscattering spectrometry (RBS), and elastic recoil detection (ERD). In RBS the energies of the projectiles after collision with a target particle are analyzed. In ERD the energies of the recoiled particles from the target sample are analyzed.

Kinematics

In figure 2.2 the scattering geometry of a collision is depicted together with the naming conventions for the different angles. When a MeV projectile collides with a target atom, energy is elastically transferred from the projectile to the target. The ratio of transferred energy is called the kinematic factor K , $K_{\text{RBS}} = E_1/E_0$ for RBS, and

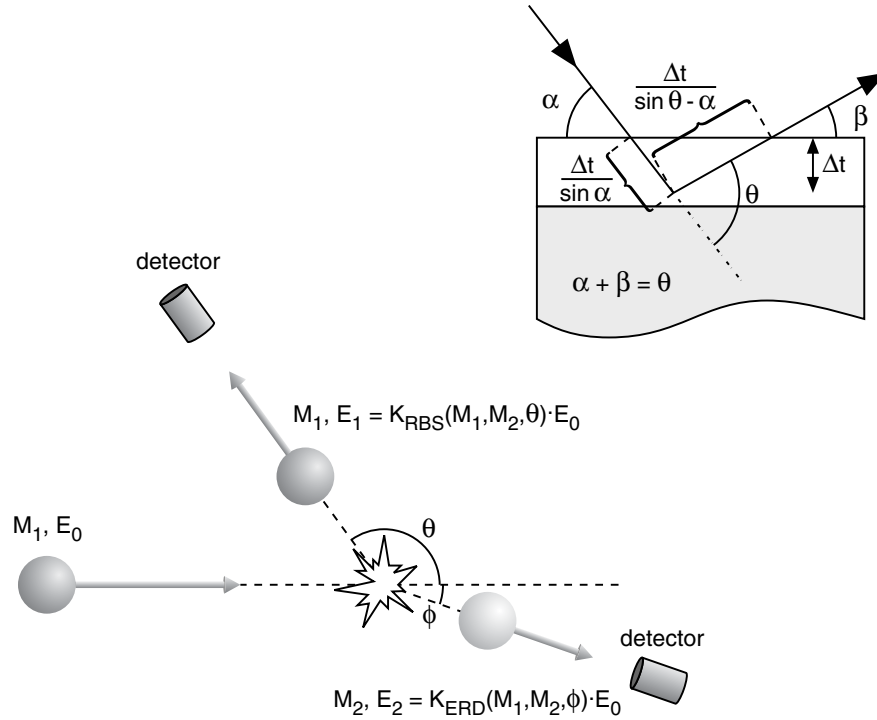


Figure 2.2: Definitions in ion beam analysis for angles (α , β , θ), masses (M_1, M_2), and energies (E_1, E_2). In the top right figure it is indicated how the length of the in- and outward path depends on α and θ .

$K_{\text{ERD}} = E_2/E_0$. From basic energy and momentum conservation laws we have:

$$K_{\text{RBS}} = \frac{E_1}{E_0} = \left[\frac{(M_2^2 - M_1^2 \sin^2 \theta)^{1/2} + M_1 \cos \theta}{M_2 + M_1} \right]^2, \quad (2.1)$$

$$K_{\text{ERD}} = \frac{E_2}{E_0} = \frac{4M_1M_2}{M_1 + M_2} \cos^2 \phi. \quad (2.2)$$

We see that the kinematic factors depend on M_2 and therefore result in mass dispersion. For the following discussion we will focus on the principles of RBS; the treatment of the principles of ERD is similar and is therefore omitted.

Energy loss

Depth information can be obtained as a result of energy loss of the particles when traveling through the layer. The particles will lose energy mainly by excitation of and inelastic collisions with electrons, i.e., electronic stopping.

Assuming a constant stopping power over both the inward and the outward path

(surface energy approximation), we may write for the energy loss in the case of RBS:

$$\Delta E_{AB} = N_B \Delta t \left[K_A \frac{\epsilon_{B,\text{in}}}{\sin \alpha} + \frac{\epsilon_{B,\text{out}}}{|\sin(\theta - \alpha)|} \right]_A = N_B \Delta t [S]_A^B,$$

$$\text{with : } \epsilon_{B,\text{in}} = \left. \frac{1}{N_B} \frac{dE}{dx} \right|_{B,E_0}$$

$$\epsilon_{B,\text{out}} = \left. \frac{1}{N_B} \frac{dE}{dx} \right|_{B,KE_0}. \quad (2.3)$$

Here ΔE_{AB} is the energy loss of a projectile after collision with an atom A in a matrix B at a depth Δt and exiting the layer again as indicated in figure 2.2. N_B is the atomic density of the matrix B . ϵ_B is called the stopping cross-section and $[S]$ is the backscattering energy loss factor (about 75 eV/(10¹⁵ at./cm²) for 2.4 MeV He⁺ projectiles in CaP). It can be seen that the energy loss of the projectiles, and thus the depth sensitivity, can be increased by decrease of the entrance angle α or the exit angle β ($= \theta - \alpha$).

Quantification

In the surface energy approximation, the yield of scattered projectiles from an element A may be expressed as:

$$Y_A = \frac{\sigma_A \Omega Q (N \Delta t)_A}{\sin \alpha}. \quad (2.4)$$

Here σ_A is the cross-section for the scattering process, Ω the solid angle of the detector, Q the number of incident particles and $(N \Delta t)$ the areal coverage of element A .

In figure 2.3 we see an example of a RBS spectrum of a ≈ 200 nm CaP coating. The Ca, P, and O signals are indicated. Clearly, the Ca and P signals can be separated from the Si substrate signal. Absolute coverages for Ca, P, and O can now be calculated by comparing the elemental yield with the height of the Si signal. Note that the height of the silicon signal can be expressed as $Y_{Si}/\text{channel}$. By combining 2.3 with 2.4 and inserting δE as the equivalent energy for 1 channel, we have:

$$(N_A \Delta t) = \frac{Y_A \sigma_{Si} \delta E}{H_{Si} \sigma_A [S]_A^{Si}}. \quad (2.5)$$

One way to calculate the coverages is by determining the height of the Si signal (H_{Si}), the contents of the Ca, P, and O signals, and application of expression 2.5. Another strategy that was frequently employed is by simulation of the experimental data. Simulation was done with the computer code RUMP [126] and stopping power tables from Ziegler [127, 128]. In figure 2.3 also the simulated spectrum is plotted together with the experimental data. The indicated thickness and composition were extracted from the simulation.

Quantification of ERD elemental yields was done using a computer code based on the yield equations above (I2P, based on reference [125]), and comparison with appropriate reference samples.

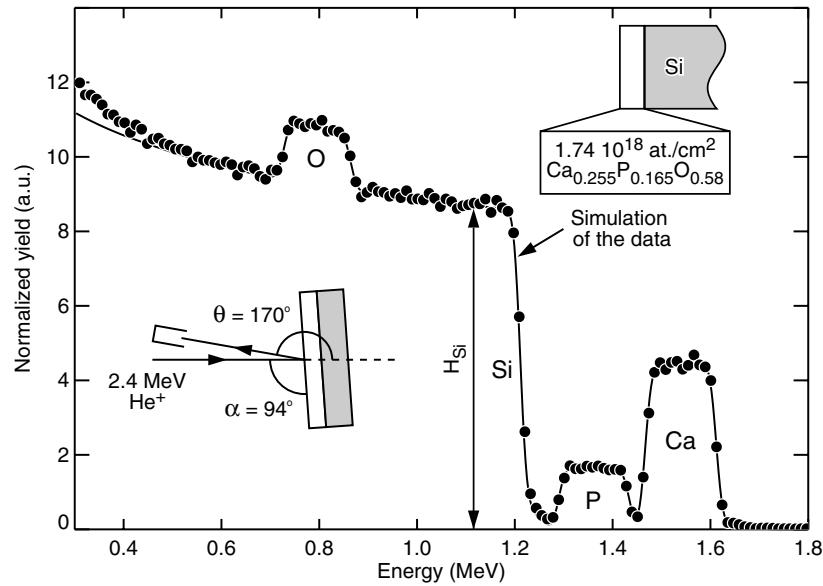


Figure 2.3: Typical RBS spectrum for a heat-treated CaP coating deposited at 2×400 W from granulated HAP targets. Contributions from the various elements to the signal are indicated. The solid line is a simulation based on the coatings thickness and composition as indicated in the figure. RBS: 2.4 MeV He^+ , $\theta=170^\circ$, $\alpha=94^\circ$.

Experimental

RBS experiments were performed in one of the ion-scatter setups connected to the 3 MV single-ended Van de Graaff accelerator at Utrecht University. For most experiments, a 2.0 or 2.4 MeV He^+ beam was used. The scattered He^+ projectiles were detected with a silicon surface barrier detector.

For most of the ERD experiments, a ^{63}Cu ion beam was used with energies in the range of 50-66 MeV. Recoils were detected with a gas filled ionization detector [129]. The incoming recoils ionize gas molecules and lose energy in the detector. If the detected particle is stopped within the detector, both the energy loss (over the first part of the detector) and total energy can be determined. The energy loss of the particles increases with the atomic number Z . This allows the separation of the signals for the various elements as shown in figure 2.4. In general, RBS was used for the analysis of elements heavier than Si and ERD for elements lighter than Si.

2.4.2 Light scattering

In section 5.3.2 we conduct an experiment to study the activation of CaP nucleation. For this purpose, a static light scattering experiment is executed, to determine the kinetics of crystal formation. The theory for static light scattering (SLS) is among others

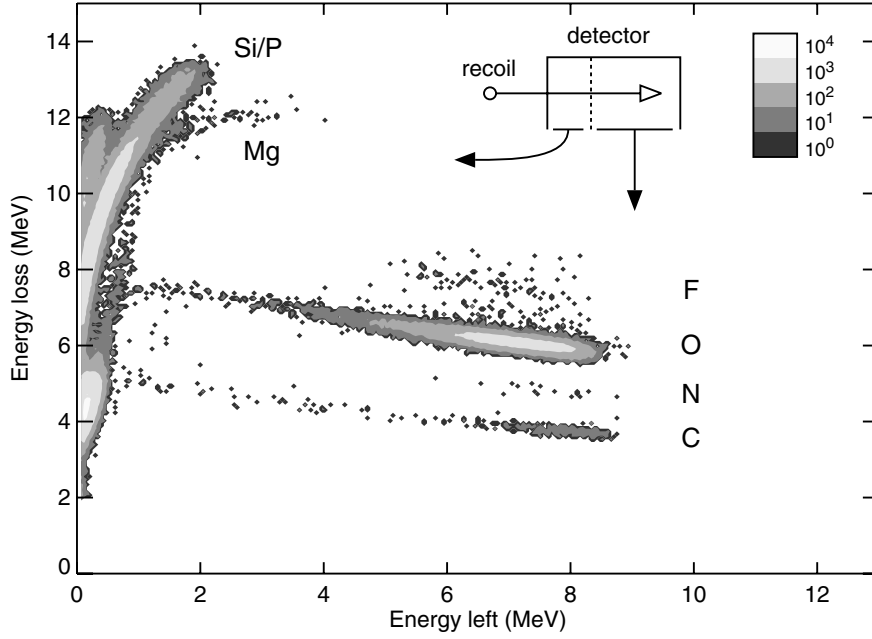


Figure 2.4: ERD dE-E spectrum of a 70 nm heat-treated CaP coating on Si. Due to differences in energy loss the signal of the various recoils can be separated. ERD: 50 MeV ⁶³Cu, p=42 mbar, $\phi=30$, $\alpha=20$.

treated in depth by van de Hulst [130]. If the wavelength of the scattered light is larger than the particle size, Raleigh Scattering can be used. Wavelengths should be larger outside as well as inside the particles. If we neglect absorption of light by the scattering particles and assume natural unpolarized light and a scattering angle θ of 90° we can write for the scattered light intensity:

$$I = \frac{8\pi^4 |\alpha|^2}{r^2 \lambda^4} N I_0, \quad (2.6)$$

with λ the wavelength and I_0 the intensity of the incident light, r the distance of the detector to the scattering particles, N the number of particles, and α the polarizability of the particles. α depends on the refractive index of the particles (which is real if we neglect absorption) compared to the medium, and on the geometry of the particles. Since the refractive indices of most CaP phases are between 1.5 and 1.6 [131], the ratio between refractive indices of CaP and water is ~ 1.2 and thus fairly close to 1. The polarizability may now be approximated by an expression which is isotropic and independent of the particle geometry:

$$\alpha = \frac{(n^2 - 1)V}{4\pi}, \quad (2.7)$$

with n the refractive index and V the particle volume. If we substitute expression (2.7) in equation (2.6) we have:

$$I = \frac{\pi^2 (n^2 - 1)^2}{2r^2} I_0 \frac{V^2}{\lambda^4} = K \frac{c^2}{\lambda^4}, \quad (2.8)$$

with $c = NV\rho$ the net atomic coverage (ρ is the atomic density in at.cm^{-3}). We see that the scattering intensity is proportional to $\frac{V^2}{\lambda^4}$. When we consider a constant number of particles positioned on a surface, the intensity is also proportional to $\frac{c^2}{\lambda^4}$. This result is quite robust for deviations in particle shape.

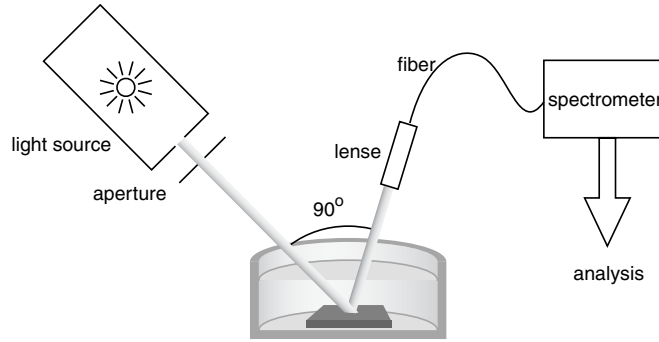


Figure 2.5: Static light scattering (SLS) setup.

If the scattering particles grow in time, we designate the point of a first detectable increase in scattering yield as the *inflection point*, and associate with this point the inflection time t_{infl} and the intensity I_{infl} . As a reference, let us assume that for a certain large wavelength λ_r we know the coverage $c_r (=NV_r\rho)$ at the inflection point, t_{infl} . We may write:

$$I_{\text{infl}} = K \frac{c_r^2}{\lambda_r^4}. \quad (2.9)$$

If the increase in atomic coverage proceeds in an approximately linear fashion after an inert onset time τ (the *induction time*), we may write:

$$c(t) = R(t - \tau), \quad (2.10)$$

with R the growth rate. If we now combine equations (2.8) with (2.9) and substitute expression (2.10), we find for the inflection time t_{infl} :

$$t_{\text{infl}} = \frac{c_r}{\lambda_r^2 R} \lambda^2 + \tau. \quad (2.11)$$

Thus we see that if we plot the inflection time versus λ^2 , the slope will be inversely proportional to the growth rate, and the offset will be the induction time.

The setup for the light scattering experiment is outlined in figure 2.5.

2.4.3 XRD

X-ray diffraction (XRD) measurements were performed with a Philips PW3710 thin film diffractometer with a Cu-K α source ($\lambda=0.154$ nm) with a fixed divergence slit, a monochromator, and a solid state detector. Recorded XRD spectra were compared with Elliot [17] for phase identification. A fixed angle of incidence of 2.5° was used.

Description of the CaP Coatings and Solutions

3.1 Introduction

In this chapter the composition, thickness, crystallinity, porosity morphology, and stability of the RF-sputtered CaP coatings are characterized. In the second part we will address the thermodynamical properties of the simulated body fluids that will be used in the following chapters. Both the coating and solution descriptions impose important boundary conditions on the dissolution and precipitation processes.

3.2 Part I: RF-sputter deposited CaP thin films

Typical deposition parameters were listed in section 2.2. To obtain coatings with Ca/P ratios that closely resemble HAP, 2 plasma sprayed HAP targets or 2 targets of granulated HAP powder were used at 400 W, or one target of granulated HAP was used at 600 W. Both parameter settings result in a Ca/P ratio of 1.6 ± 0.1 .

At equal discharge powers, deposition rates were considerably higher for the plasma sprayed targets compared to the granulated HAP powder targets. For the granulated targets, the average deposition rate for one target at 600 W was ~ 2.5 nm/s, for two targets at 400 W it was ~ 3.5 nm/s. In figure 2.3 we already showed an RBS spectrum of a CaP coating sputtered from 2×400 W granulated HAP targets. In figure 3.3 an RBS spectrum of a CaP coating from 1×600 W granulated HAP powder target is shown. For most of the experiments in the following chapters the 600 W deposition was used,

which allowed the other target to be used for the deposition of a TiO₂ interlayer as discussed below.

In table 3.1 atomic concentrations obtained from RBS and ERD measurements are summarized for as-deposited CaP coatings. Indeed the Ca/P ratio is ~ 1.6 . The P/O ratio is $\sim 1/4$ suggesting that P and O are mainly incorporated as (ortho)phosphate. Small amounts of hydrogen and carbon could be detected, probably present as OH and CO₃. Also, small amounts of contaminant N, F, and Mg could be detected. In

Element	as-deposited	heat-treated
H	2.0	1.1
C	0.7	0.5
N	0.4	0.4
O	58.	58.
F	0.14	0.11
Na	0.08	0.08
Mg	0.36	0.12
P	15.	15.
Ca	24.	25.

Table 3.1: Atomic concentrations (in at.%) for various elements from ERD and RBS. The second column gives as-deposited coating concentrations, the third contains the heat-treated coating concentrations. Errors were estimated at 5-10% of the given values.

figure 3.1 the coating thickness and composition are plotted versus the distance from the center of the deposition chamber. It can be seen that the coating thickness at the outside of the sample holder decreases by a factor of almost 2 compared to the center. On the other hand, the Ca/P ratio does not depend on the position of the sample on the sample holder.

From the results of van Dijk et al. [95] it is clear that sputtered CaP coatings can be (partly) crystallized at temperatures higher than $\sim 550^\circ\text{C}$. Above 800°C also CaO is expected, and above 1200°C also high temperature phases like β -TCP can be found. In this work all heat treatments were done at 650°C after Wolke et al. [96]. In figure 3.2 the diffractogram before and after a heat treatment is shown. Reflecting plane indices for HAP are indicated. The as-deposited coatings are mainly amorphous as can be seen from the bump between 25° and 35° . Also, a small fraction of a (001) oriented apatite structure can be identified. After the heat treatment the amorphous phase is largely converted to a more randomly oriented apatite structure.

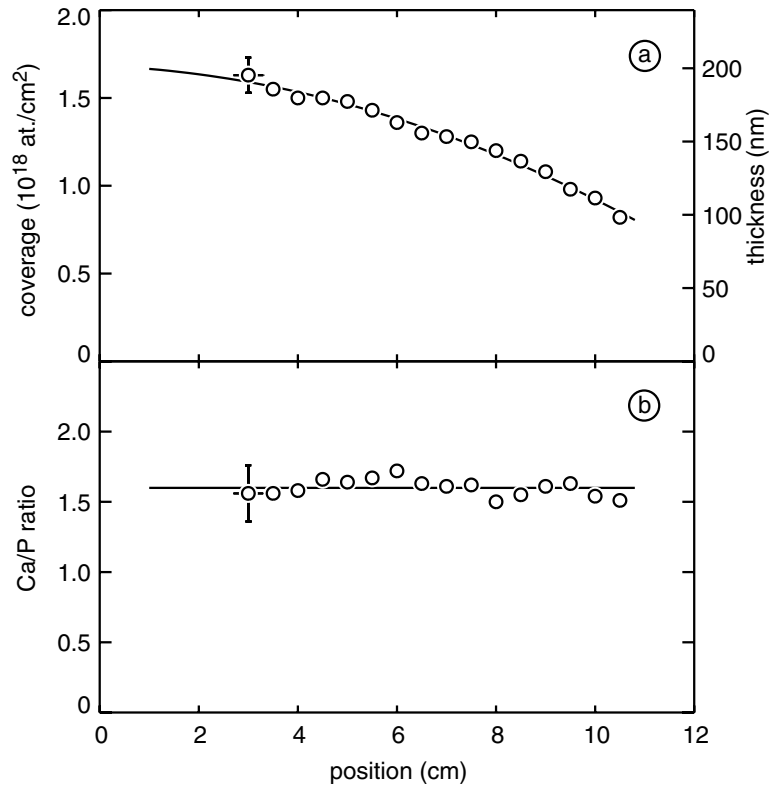


Figure 3.1: Thickness and composition of 2×400 W CaP coatings as a function of their distance from the center of the deposition chamber.

3.2.1 Graded Ca/P ratios

To produce CaP coatings with different coating composition, two strategies were employed. First targets with different Ca/P ratios were pressed from mixtures of DCPA, HAP, and TTCP. Sputtering from these targets resulted in coatings with different Ca/P ratios, but target failure was too high to produce coatings with custom Ca/P ratios routinely. The second method was to vary the power between two targets of different composition. For this purpose, a target of granulated pyrophosphate ($\text{Ca}_2\text{P}_2\text{O}_7$) and a target of CaO powder were used. The RBS spectra for the produced CaP coatings are presented in figure 3.3. The corresponding Ca/P ratios are shown in table 3.2. It is clear that by this method the coating can be accurately tailored. In figure 3.4 diffractograms are shown for the coatings with a varying Ca/P ratio after a heat treatment of 30 minutes at 650°C . As expected [17, 69], the only crystalline phase that can be identified is the apatite phase (reflecting plane indices are indicated). Surprisingly, if the Ca/P ratio is below a critical value, no apatite crystallization is possible. However, there seems to be no upper limit, below a ratio of ~ 5 , for apatite formation. For the sample with a Ca/P ratio of 4.7 peak-broadening can be observed as compared to the lower Ca/P ratios, indicating the presence of smaller CaP crystallites.

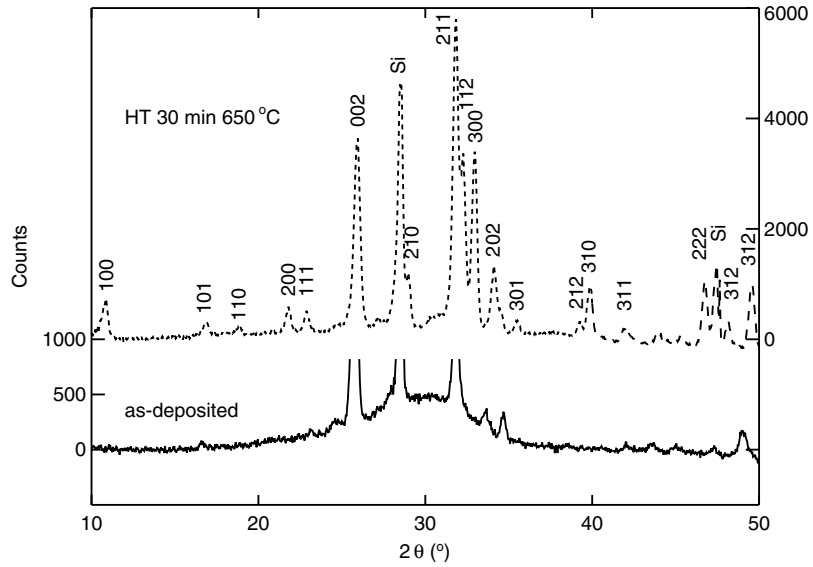


Figure 3.2: Diffractograms of a 600 W CaP coating before and after a heat treatment (HT) of 30 minutes at 650°C. A strongly oriented apatite fraction can already be identified in the as-deposited coating.

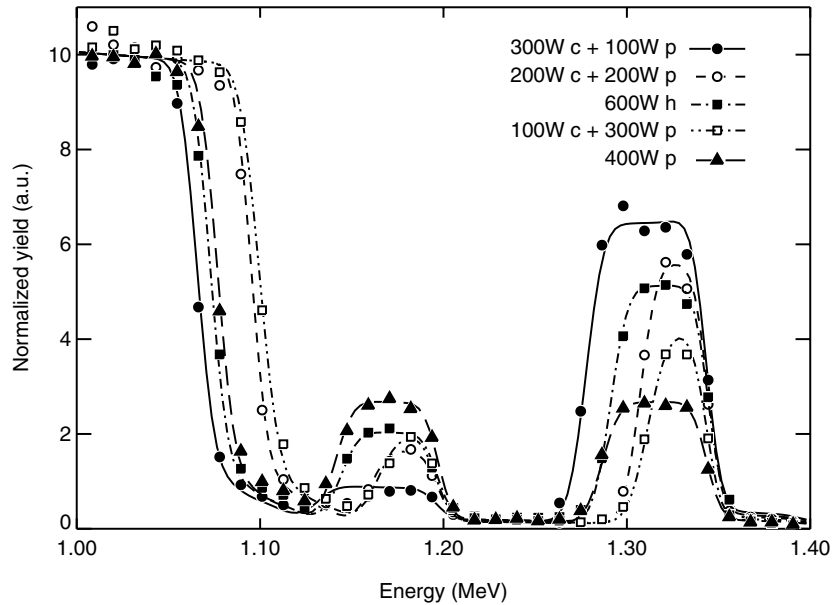


Figure 3.3: RBS spectra for CaP coatings after 30 minutes of deposition using different sputter targets operated at different powers. Ca/P ratios are listed in table 3.2. RBS: 2.0 MeV He⁺, $\theta=170^\circ$, $\alpha=94^\circ$.

Power			Ca/P ratio
CaO	pyro	HAP	
300	100	600	4.7
200	200		2.3
100	300		1.6
			1.3
			0.6

Table 3.2: Ca/P ratios as a function of target power.

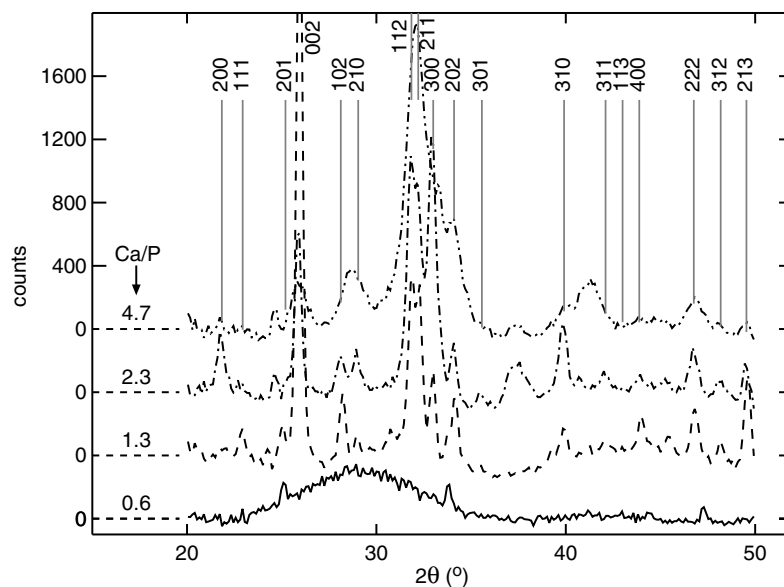


Figure 3.4: Diffractograms of CaP coating with different Ca/P ratios before and after a heat treatment of 30 minutes at 650°C.

3.2.2 Coating integrity

One of the problems that arise in preparing CaP thin films on Si substrates is the delamination of the coating. Coatings may peel off during the deposition, during a heat treatment, or upon immersion of the coatings in water. The first two processes are related to the stress in the coating due to differences in thermal expansion compared to the substrate. The silicon substrate has a low (linear) coefficient of thermal expansion (CTE) of $2.6 \cdot 10^{-6} \text{ K}^{-1}$ compared to the CTE of HAP of $\sim 12 \cdot 10^{-6} \text{ K}^{-1}$ (calculated from the data of Brunet et al. [132]). Cooling the samples after deposition thus results in tensile stress and a heat treatment results in compressive stress in the coatings.

It was found that at higher discharge power coatings delaminated after deposition. On the other hand, at lower discharge power many coatings detached after a heat treatment. In figure 3.5 a micrograph of a ~ 300 nm CaP coating deposited at 2×400 W is shown after a 30 minute anneal at 650°C . Clearly, blistering of the coating has

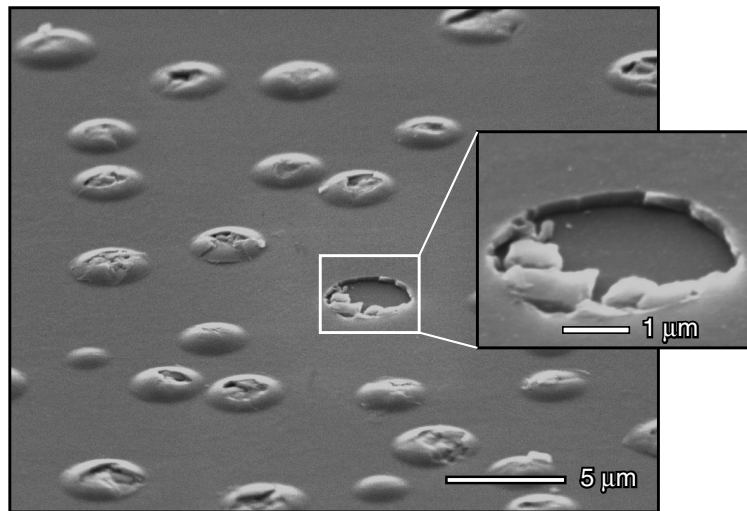


Figure 3.5: Electron micrograph of CaP coating deposited at 2×400 W and post-annealed for 30 minutes at 650°C . The blistering of the coating is due to stress relaxation.

occurred. At higher temperatures the coating completely peels off. A study at different discharge powers and heat treatments at 650 and 800°C showed that there is only a limited range of deposition conditions and annealing temperatures that results in blister-free crystallized coatings on polished Si substrates. In figure 3.6 the effect of discharge power, annealing temperature, and coating thickness is summarized schematically. Stable coatings are produced in the zone enclosed by the shaded planes. Thick coatings fail at lower annealing temperatures than thin coatings. Further, a high discharge power produces coatings that can survive higher annealing temperatures.

The third reason for observed coating loss is the delamination of the CaP coatings upon immersion in water or water based solutions. This process was found to be water mediated. Already after a few minutes of immersion coatings could be wiped off with a tissue. After prolonged immersion, the complete coating peeled off. This can be prevented by the deposition of a TiO_2 interlayer between the Si substrate and the CaP coating. Even an interlayer of 10 nm completely prevents the coating from delaminating during immersion.

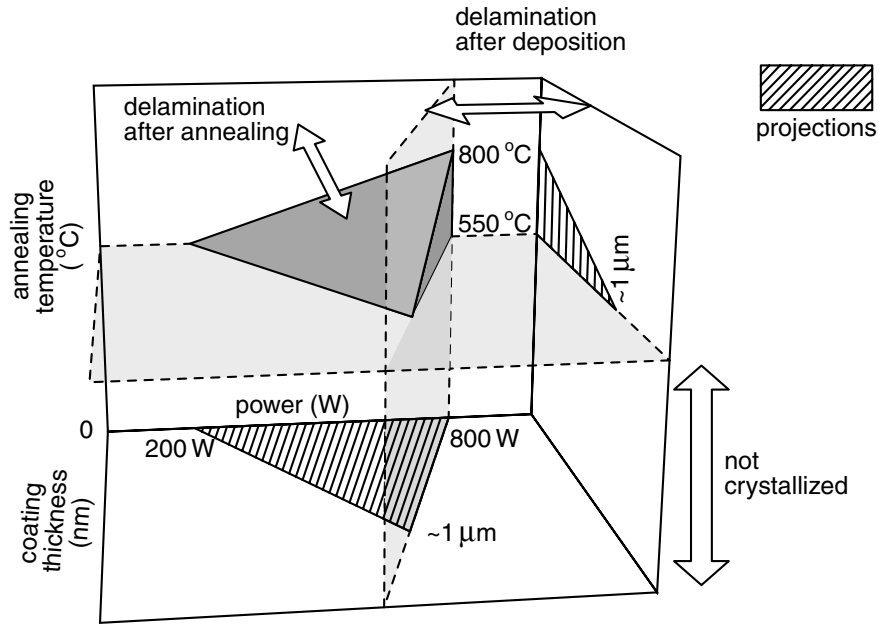


Figure 3.6: Stability diagram for crystallized CaP coatings on Si as a function of discharge power, annealing temperature, and coating thickness. Also projections of the stability region are plotted.

3.3 Part II: Thermodynamics of simulated body fluids

In this section we investigate the thermodynamic properties of the simulated body fluids (SBFs) as described in section 1.6 and section 2.3.1. Not many thermodynamical studies of SBFs can be found in literature. To get some insight in the possible potential of the SBFs to dissolve CaP coatings or to form precipitates of CaP, we will focus on their thermodynamic properties.

The theoretical background for the free energy calculations is outlined in appendix A. As in other research [133], for the following calculations we will apply the simplified free energy expression for the precipitation reaction (refer to equation A.11):

$$\Delta_{\text{prec}}G = -RT \log \frac{\text{IAP}}{K_{\text{sp}}} \equiv -RT \cdot \text{SI}. \quad (3.1)$$

ΔG (we will drop the subscript for convenience) is the molar free energy change of unit cell reactions with respect to the formation of a certain phase. The ratio of IAP/K_{sp} is called the *solubility S*, and *SI* is the so called saturation index. K_{sp} is the solubility product and the ion activity product (IAP) is defined as:

$$\text{IAP} = \prod_j a_j^{v_j}, \quad (3.2)$$

with ν_j the stoichiometric coefficient and a_j the activity of lattice species j . Since the activity of the solid *reactant* is 1, the product in equation 3.2 extends only over the *products* of the dissolution reaction. For the reaction *products* the ν_j 's are positive. For example the IAP of a solution with respect to HAP will be:

$$\text{IAP}_{\text{HAP}} = a_{\text{Ca}}^{10} \cdot a_{\text{PO}_4}^6 \cdot a_{\text{OH}}^2 .$$

Taking the logarithm of equation 3.2 gives:

$$\log \text{IAP} = \sum_j \nu_j \log a_j . \quad (3.3)$$

From 3.1 we see that for an oversaturated solution, the SI is positive, for an undersaturated solution the SI is negative, and for a solution in thermodynamical equilibrium the SI is zero.

Note that in this definition of ΔG with respect to a certain phase, its value depends on the definition of the unit cell of this phase. Since the unit cells of the different CaP phases differ, it is not possible to compare the free energy values of different CaP phases directly. We can solve this problem by introducing the volume free energy defined as:

$$\Delta G_v \equiv \frac{m \Delta G}{v} , \quad (3.4)$$

with m the total number of species in a (unit) cell, and v the (unit) cell molar volume. We can now compare the free energy releases for the formation of equally sized crystals of different phases. This volume free energy is of special importance for the nucleation theory of crystals as described in section 5.1.1. In table 3.3 we present the cell volumes for some of the CaP phases, calculated from its unit cell parameters [17].

phase	formula per cell	cell vol. (nm ³)	m
HAP	Ca ₁₀ (PO ₄) ₆ (OH) ₂	0.531	18
OCP	Ca ₈ (HPO ₄) ₂ (PO ₄) ₄ ·5H ₂ O	0.607	19
β -TCP	β -Ca ₃ (PO ₄) ₂	0.168	5
DCPD	CaHPO ₄ ·2H ₂ O	0.123	4

Table 3.3: Volumes per structure formula and the number of species per cell (m) for some of the CaP phases. Cells are not necessarily unit cells.

In order to obtain the required activities of the different species in the solution, we have to calculate the solution speciation. For this purpose, PHREEQCI was used, a computer code for speciation, batch-reaction, one-dimensional transport, and inverse geochemical calculations [134, 135]. PHREEQCI simultaneously solves a set of mass-action equations to obtain a solution that is in thermodynamical equilibrium. It uses

the Truesdell-Jones extended Debye Hückel equation [136] to evaluate the activity coefficients. Thermodynamic data were obtained from Hartley et al. [137], K_{sp} 's of CaP phases were adopted from Koutsoukos et al. [46].

Volume free energies of SBF_x with varying x can now be evaluated with respect to the different CaP phases. In figure 3.7 the calculated ΔG_v 's are plotted versus x for HAP, OCP, TCP, and DCPD. Numbers for SBF_1 and SBF_2 are also given in table 3.4.

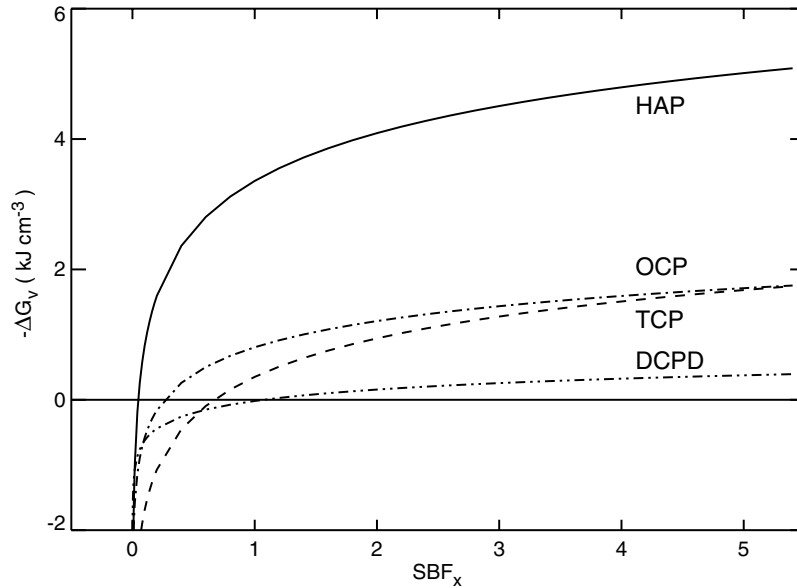


Figure 3.7: Volume free energy differences ΔG_v for SBF_x with respect to HAP, OCP, TCP, and DCPD.

As expected, the formation of HAP results in the largest free energy release and is therefore the most stable phase.

Since for most precipitating CaP solutions, HAP is the stable end product, ΔG values are often given with respect to HAP. In table 3.4, also the free energy values per mole are given for SBF_1 and SBF_2 with respect to some of the CaP phases. Also, the x is given at which the phase is at equilibrium with SBF_x . Again, be aware that the numbers for ΔG can not be compared directly between different CaP phases.

From figure 3.7 and table 3.4 we observe that both SBF_1 and SBF_2 are oversaturated with respect to the major CaP phases. However, the free energy difference of SBF_1 with respect to DCPD is approximately zero.

Analysis of the (macro)thermodynamics of the system tells us what the stable end products of the precipitation reaction will be. However, the kinetics (or microthermodynamics) of the process determine which phases will be formed in which order and on what timescale. According to Ostwald's empirical rule of stages [138, 139], it is expected from figure 3.7 that the precipitation of HAP proceeds via the metastable phases

phase	ΔG (kJ mol ⁻¹)		ΔG_v (kJ cm ⁻³)		SBF _x at eq.
	SBF ₁	SBF ₂	SBF ₁	SBF ₂	
HAP	-59.7	-72.7	-3.36	-4.09	0.047
OCP	-6.76	-18.1	-0.35	-0.94	0.67
β -TCP	-16.3	-24.4	-0.81	-1.21	0.26
DCPD	+0.34	-2.91	+0.018	-0.16	1.07

Table 3.4: Molar and volume free energy differences for SBF₁ and SBF₂ with respect to the precipitation of some of the CaP phases. Calculations were done at 25°C, pH 7.4, and a CO₂ mole fraction of 10^{-3.5}.

that are closest in free energy to the present state. This implies that according to figure 3.7, DCPD, TCP, and OCP act as precursors for the precipitation of HAP from SBFs. Due to its instability, no accurate thermodynamic data are available for amorphous calcium phosphate (ACP). At physiological conditions and moderate supersaturation, ACP, DCPD, and OCP have been reported as precursor phases for HAP [133], in the order as expected from Ostwald's rule of stages: so from the metastable phases with the lowest negative free energy difference compared to the solution, towards the most stable phase with the highest energy difference.

Dissolution of As-deposited CaP Coatings

4.1 Introduction

In this chapter we report a study of the behavior of as-deposited RF-sputtered CaP coatings under physiological conditions, without any organic additives. As was mentioned in section 1.6 Kokubo proposed simulated body fluid (SBF or SBF₁) [100–102], to test materials for their ability to form a directly bonded CaP layer as an indication of possible bioactivity. A close relation has been recognized between the formation of such a layer and the bioactive potential of a material [103].

As mentioned in section 1.6, extensive research has been done with respect to CaP formation and dissolution in solutions mimicking physiological conditions.

In this and the next chapter we focus on the dissolution and precipitation properties of CaP coatings in simulated body fluids (SBFs). More particularly, in this chapter the dissolution behavior of amorphous coatings is discussed, in SBF as well as in concentrated SBF with twice the Ca and PO₄ concentrations (SBF₂). In section 1.4 previous research was summarized on the dissolution behavior of CaPs. Firstly, we explore what happens when CaP coatings are immersed in unstirred SBF and in SBF₂.

Further, we determine whether a surface process or diffusion is rate-limiting in dissolving the CaP coating. For CaP, extensive research has been done on discriminating between surface controlled and diffusion controlled processes [20, 21, 28, 30, 31, 140, 141]. Most of this research was done on powders, mostly HAP or enamel. For both powders and solid surfaces it was found that dissolution is diffusion-limited at a wide

range of solution conditions, stirring rates, and reaction extents. For growth of CaP crystals on CaP coatings, much less is known about the influence of diffusion. We employ a strategy based on the so-called *rotating-disk* experiments to elucidate the role of diffusion in both dissolution and growth processes. Firstly, in section 4.1.1 some background on the theory involved in these experiments is given.

The main goal of the experiments in this chapter and next one is to reveal the importance of the observed processes under simulated physiological circumstances, and relate them to processes also observed in early osteogenesis.

4.1.1 Diffusion

Near a growing or dissolving surface, differences in chemical potential (μ) are the driving force for the migration of species from or to the surface. We can treat this as a non-equilibrium, and in the end, a steady-state process. In general we can state that for the flux of species S , J_S :

$$J_S = -M_S c_S \frac{\partial \mu_S}{\partial x}, \quad (4.1)$$

with c_S the concentration and M_S the mobility of species S . Inserting $M_S = D_S/kT$, with D_S the diffusion coefficient, we get:

$$J_S = -\frac{D_S}{kT} c_S \frac{\partial \mu_S}{\partial x}, \text{ or :} \quad (4.2)$$

$$J_S = -D_S \left[\frac{1}{kT} c_S \frac{\partial \mu_S}{\partial c_S} \right] \frac{\partial c_S}{\partial x}. \quad (4.3)$$

The term in between brackets is denoted the *thermodynamical factor* F . From expression 4.3 we now obtain Fick's first law with an effective diffusion coefficient of $D_S F$:

$$J_S = -D_S F \frac{\partial c_S}{\partial x}. \quad (4.4)$$

In chapter 6 we elaborate in detail on the structure of the adsorption and diffusion layer. For now, we define the *Nernst layer* as the layer in the solution near the surface where the chemical potential falls off to the bulk value. It can be found by linearization of expression 4.4:

$$J_S = -D_S F \frac{c_{S,0} - c_{S,b}}{\delta}, \quad (4.5)$$

with $c_{S,0}$ the surface concentration, and $c_{S,b}$ the bulk concentration of species S , and δ the thickness of the Nernst layer.

A well known approach to study the relative importance of the diffusion in a crystal growth or dissolution process is the use of a rotating disk. For enamel and HAP surfaces this strategy was employed before [19, 38, 142]. In figure 4.1 a schematic view of the setup is depicted. In short, the rotation of the disk induces a laminar flow along

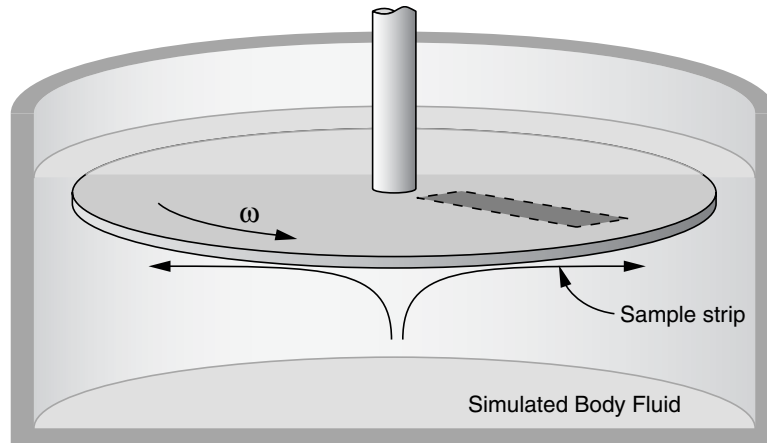


Figure 4.1: Setup for the diffusion experiments. An uncut CaP sample strip is mounted on a disk and rotated in SBF for some time to allow significant growth or dissolution.

the surface of the disk affecting the thickness of the Nernst layer and according to equation 4.5 the flux of species to or from the bulk solution. For a rotating disk in a solution, fluid mechanics have to be considered. So far, we did not take drift effects into account, nor the effect of convection or viscous drag. According to Levich [143], the thickness of the Nernst layer can be expressed as:

$$\delta \sim D_s^{1/3} \nu^{1/6} \omega^{-1/2}, \quad (4.6)$$

where ν is the kinematic viscosity of the solution, and ω is the angular speed of the disk. It can be seen from equations 4.5 and 4.6 that the rate of growth or dissolution increases when the angular speed is increased. Levich assumed a radial flow of the solution from the center to the edge of the disk. In this simple model the thickness of the Nernst layer in the center of the disk is equal to the thickness on the outer part. However, due to drag forces of the container, we expect that the solution is not able to keep up with the rotating surface, resulting in an extra shear force on the Nernst layer. This effect is larger for the fast moving outer part of the disk. We thus expect that the dissolution and growth rates on the outer part of the disk are somewhat higher than on the inside.

4.2 Experimental considerations

4.2.1 Immersion studies

The immersion experiments described in this chapter were carried out in simulated body fluids with different Ca and PO₄ concentrations (SBF_x). Most of the SBFs used in this chapter were prepared from stock solutions immediately prior to use as described in section 2.3.1. The immersion protocol was described in section 2.3.2. In short, SBFs

were prepared from stock solutions and pH was adjusted to 7.4. After immersion in 10 ml of solution, samples were rinsed with water and dried to air.

To investigate the diffusion properties of our system, we employed a method based on the so-called rotating disk experiments as described elsewhere [19, 38, 142]. No effort was done to create well described hydrodynamical conditions, since our interest is purely qualitative. A schematic setup is shown in figure 4.1. A coated strip of ~ 6 cm was attached to a disk, immersed in 500 ml SBF, and rotated with a frequency of about 40 revolutions per minute. Immersion periods were chosen such that significant dissolution or precipitation occurred. Coverages of CaP of immersed coatings and their references were determined with RBS.

4.2.2 Coating application

Coatings were deposited on silicon (100) substrates with RF magnetron sputtering in $5.0 \cdot 10^{-3}$ mbar Ar using one target and a rotating substrate holder. CaP coatings were sputtered for 30 minutes at 600 W (unless stated otherwise) from a target of granulated CaP. An intermediate TiO_2 layer (30 s at 200 W) of ~ 10 nm was applied as a bonding layer to prevent delamination during immersion. CaP layers were found to be between 60 and 80 nm thick from RBS. Coated strips were cut into pieces of 1 cm^2 . For each sample used in the experiments, the sample that was right next to it in the sputter chamber was saved as a reference. This allowed an accurate and sensitive determination of changes in coating thickness.

4.3 Static dissolution of as-deposited coatings

In this first part we report on the immersion of as-deposited RF-sputtered CaP coatings in simulated body fluids with different total amounts of Ca and PO_4 concentrations. More specific, besides SBF_1 , also immersion in SBF_2 , is studied. In figure 4.2 **a** RBS depth profiles are given for Ca, P, and O, before and after immersion for 14 hours in SBF_2 . Clearly the loss of material can be seen. The thickness of the untreated sample equals 215 nm, whereas the immersed sample thickness is reduced to 155 nm. No change in the coating composition is observed. Thus, elemental dissolution is homogeneous, the elemental constituents are dissolved equally. The steepness of the back edges indicates little surface roughness after dissolution. From ERD measurements no significant change could be observed of H, N, F, Na, or Mg content, as can be seen from table 4.1. A slight increase in the C concentration can be observed after dissolution.

In figure 4.2 **b** the total dissolved content versus time is plotted for dissolving as-deposited coatings in SBF_1 and SBF_2 . The rate of dissolution in SBF_1 and SBF_2 is determined to be $4.3 \cdot 10^{15}$ and $0.70 \cdot 10^{15} \text{ at./cm}^2 \text{ min}^{-1}$ respectively (or $5.2 \cdot 10^{-1}$ and $8.5 \cdot 10^{-2} \text{ nm min}^{-1}$). For these coatings, dissolution rates tend to be constant on the studied timescale. A dissolution experiment with coatings of different Ca/P ratios (refer to section 3.2.1) showed dissolution of all coatings at roughly the same rate.

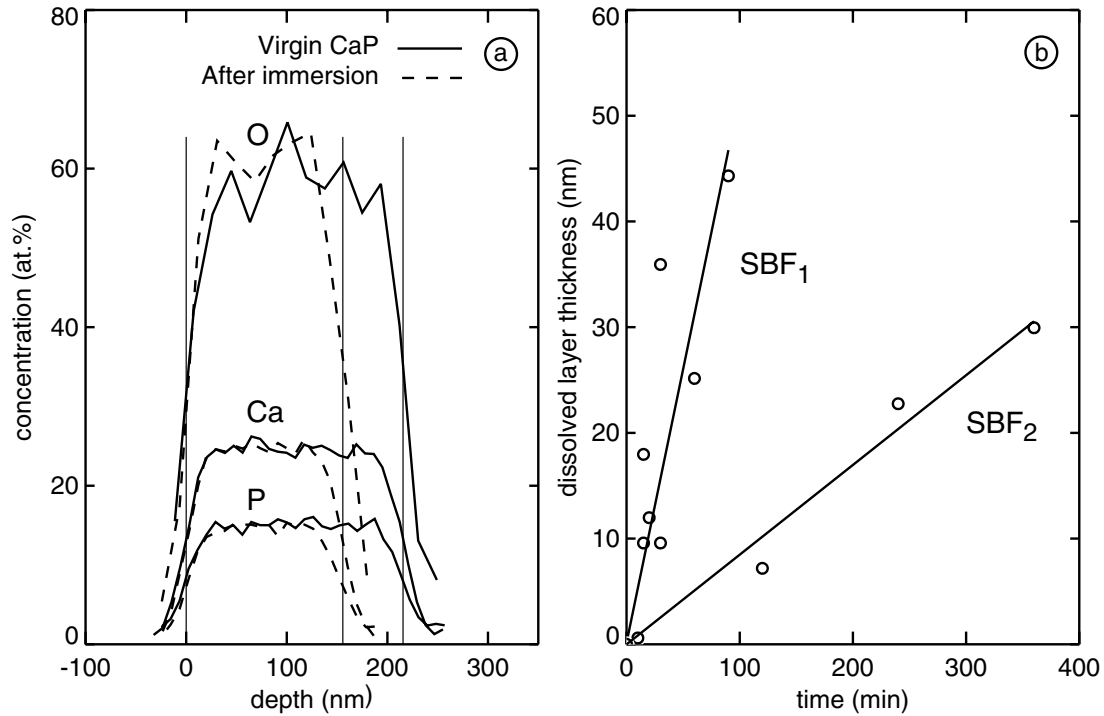


Figure 4.2: **a)** RBS elemental depth profiles for Ca, P, and O. Solid lines correspond to an 400 W as-deposited reference, and broken lines to a sample that was immersed in SBF₂ for 14 hrs at 20°C. RBS: 2.4 MeV He⁺, $\theta=170^\circ$, $\alpha=85^\circ$. **b)** Coating thickness versus time for 600 W as deposited coatings immersed in SBF₁ and SBF₂ at 20°C.

4.4 Diffusion

To investigate the role of diffusion in the dissolution and growth processes of CaP, we use the experimental setup as described in section 4.1.1 and 4.2.1. In figure 4.3 the effect of rotation of the coated strip in SBF₁ (full circles and solid line) and SBF₂ (open circles and broken line) is shown on the dissolution rate of non-annealed CaP coatings. Also the dissolution rates in SBF₁ and SBF₂ without rotation are indicated. Clearly, the average dissolution rates on the coated strips are much higher for the rotating samples as compared to the non-rotating references. It also appears that the dissolution rate depends on the distance to the center of the disk, as we expect for diffusion-limited dissolution (refer to section 4.1.1).

4.5 Discussion

We have investigated in this chapter how as-deposited RF-sputtered CaP coatings interact with solutions that mimic the physiological composition of body fluid.

Element	as-deposited	14 hrs SBF ₂
H	2.0	2.0
C	0.7	1.2
N	0.4	0.4
O	58.	57.
F	0.14	0.12
Na	0.08	0.08
Mg	0.36	0.23
P	15.	14.
Ca	24.	24.

Table 4.1: Atomic concentrations (in at.%) for various elements from ERD and RBS. The first column gives as-deposited coating concentrations, the second contains precipitated concentrations in the remaining coating after dissolution for 14 hrs in SBF₂. Errors were estimated at 5-10% of the given values.

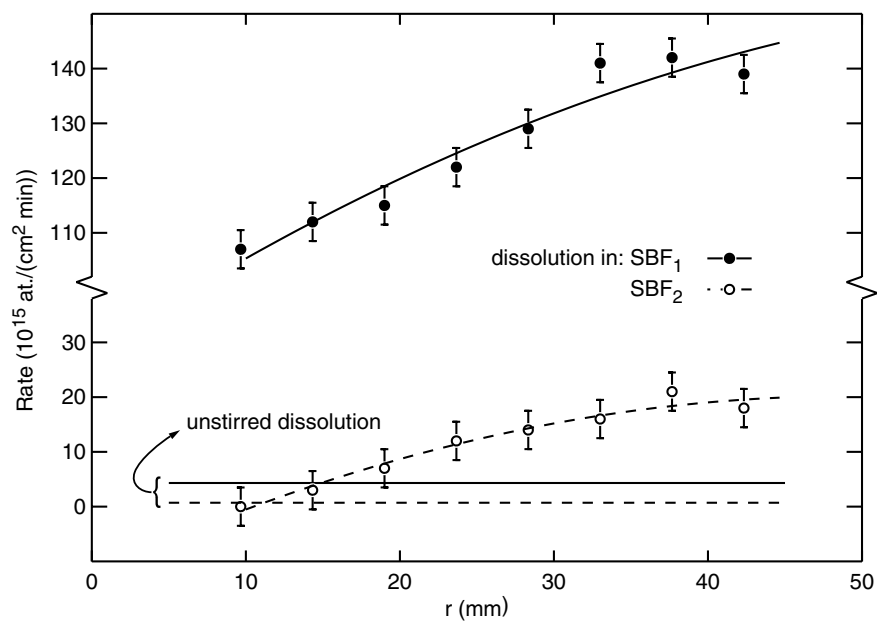


Figure 4.3: Dissolution rate versus sample position for amorphous CaP coatings in SBF₁ and SBF₂ for rotating and non-rotating samples.

As-deposited coatings were found to dissolve in simulated body fluids, even with twice the Ca and PO₄ concentrations (SBF₂). For all stable SBF_x solutions, i.e., all SBF_x that did not show immediate homogeneous precipitation upon mixing of the stock solutions, as-deposited CaP coatings were found to dissolve.

Firstly, we have seen that the dissolution of our CaP coatings is linear and congruent. This is in agreement with findings in literature for diffusion-limited dissolution of amorphous CaPs. Further, it was found that the dissolution of RF-sputtered CaP coatings is diffusion-limited by employing a method based on rotating disk experiments. The most important indication of this was the large increase in the dissolution rate when rotating the sample (figure 4.3). This result is not too surprising since it was found that for many CaP systems, coatings and powders, and under a wide range of solution conditions, dissolution is limited by diffusion when the solution is not stirred. Therefore, we do not see dissolution deceleration, in contrast to what is described in literature for surface controlled CaP systems (HAP powders at high stirring rates) [29, 144].

4.6 Conclusions

We have given an short overview of the dissolution behavior of RF-sputtered CaP coatings in simulated body fluids.

The amorphous as-deposited CaP coatings were found to dissolve in all stable SBFs. Composition of the CaP coatings does not greatly affect the dissolution process. Dissolution of amorphous CaP coatings was found to be diffusion-limited.

Precipitation on Heat-treated CaP Coatings

5.1 Introduction

In the previous chapter we have seen that as-deposited coatings dissolve when exposed to simulated body fluids (SBFs), even when twice the Ca and PO₄ concentrations were used. In this chapter we study the behavior of heat-treated CaP coatings in SBFs with different Ca and PO₄ concentrations. Extensive work has been done on the crystallization of CaP on CaP surfaces and is summarized in section 1.4.

We explore the conditions under which the sputtered CaP coatings allow the formation and growth of CaP crystals on their surface. For this, it is important to distinguish between different mechanisms of precipitation. There is primary nucleation, which is driven by the solution itself. This can be homogeneous, within the solution, or heterogeneous, catalyzed by a surface. Homogeneous precipitates can be found on a surface by sedimentation, the attachment of particles from the solution to the surface. Further, also secondary nucleation can occur on a surface: nucleation of a phase on seeds of crystals of the same phase. As we will see, in practice it can be very difficult to distinguish between the various forms of nucleation. We start this chapter with a short overview of some of the most important concepts from classical heterogeneous nucleation theory. This gives us insight into the physical parameters that govern these processes.

To investigate the role of the coating composition on the nucleation of CaP we evaluate the behavior of coatings of other oxides (like Al₂O₃, TiO₂, and SiO₂) on CaP

nucleation. For the CaP coatings we determine the influence of the Ca/P ratio on the nucleation potential.

Under the appropriate conditions, it turns out that the growth of a precipitate is preceded by a period of approximately an hour, in which almost no material is deposited from the solution. Therefore, the study on the formation of a precipitate is divided in two parts. In the first part, processes during the initial stage are studied, in the second part we focus on the subsequent growth of the precipitate.

Besides the formation of CaP crystals we also study the subsequent growth of a precipitated CaP layer after nucleation, again in SBF₁ and SBF₂. Nucleation and growth of CaP crystals on the coatings are followed in time.

Finally, we briefly examine the diffusion properties of the growth process.

5.1.1 Classical nucleation theory

To obtain some insight into the parameters that control the heterogeneous nucleation of CaP crystals on a coating surface, we present in short some of the most important results of the classical nucleation theory [48, 145, 146]. Let us treat the simple but illustrative case of a cap-shaped nucleus with a radius r . For the free energy change due to the formation of a nucleus we can write:

$$\Delta G = \frac{2}{3}\pi r^3 \Delta G_v + \pi r^2 (2\sigma_{cl} + \sigma_{cs} - \sigma_{sl}) , \quad (5.1)$$

with σ_{ij} is the surface free energy between substance i and j , where the subscripts c, s, and l denote the crystal (the nucleus), the surface (the coating), and the liquid (solution). ΔG_v is the change in volume free energy, as derived in section 3.3:

$$\Delta G_v = -\frac{mRT}{v} \log S . \quad (5.2)$$

Note that ΔG_v is negative, since the solution will have to be supersaturated ($S > 1$, i.e., $IAP > K_{sp}$) to allow nucleation. We have neglected free energy changes due to lattice distortions, formation of cluster-edges, and rearrangement of charges in the electrical double layer.

We clearly see two competing processes: the volume phase change of the nucleus is exothermic, whereas the formation of a new (larger) surface tends to be endothermic. The latter dominates for nuclei smaller than some critical size, that will be unstable and dissolve. Nuclei larger than the critical nucleus size, will be stable and able to grow. We can now calculate the free energy change ΔG^* required to form a critical nucleus or the *activation energy* A :

$$A = \Delta G^* = \frac{\pi \Delta \sigma^3}{3 \Delta G_v^2} = \frac{\pi (2\sigma_{cl} + \sigma_{cs} - \sigma_{sl})^3}{3 (mRT/v)^2 (\log S)^2} . \quad (5.3)$$

In almost every case the influence of the substrate is to reduce the energy barrier for nucleation as compared with homogeneous nucleation, and hence catalyzes the

nucleation process. From the law of mass action we know that ideally the nucleation rate will be proportional to $\exp[-\Delta G^*/(RT)]$. Following Walton and Nielsen [145, 146], we introduce the *induction time* τ as the (arbitrary) time at which a detectable amount of precipitated material can be distinguished.

$$\tau = C \exp \left[\frac{\Delta G^*}{RT} \right]. \quad (5.4)$$

Thus, if an induction time is measurable, we have a very sensitive probe for the activation energy of nucleus formation. Combining equations 5.4 and 5.3 yields:

$$\log \tau/C = \frac{\pi}{3} \frac{(2\sigma_{cl} + \sigma_{cs} - \sigma_{sl})^3}{(RT)^3(m/v)^2(\log S)^2}. \quad (5.5)$$

The induction time will thus be very sensitive to the surface free energy properties of the coating, to the temperature, and to the solubility S . Materials that show a very long induction time ($\gg 2$ hours) for CaP nucleation will be addressed as *inert*. Since the induction time is so sharply dependent on the surface free energy, we expect a clear distinction between *active* and *inert* materials.

5.2 Experimental considerations

The immersion experiments were carried out as we described previously in section 2.3.2. In short, SBFs were prepared from stock solutions as described in section 2.3.1. pH was adjusted to 7.4. After immersion in 10 ml of solution, samples were rinsed with water and dried to air.

In some experiments, strontium labels were used as a marker for Ca adsorption and precipitation. The use of labels for Ca and PO_4 is a powerful tool that will be used frequently in this thesis. Obviously, it is difficult to quantify small amounts (a few times 10^{15} or less) of deposited Ca or PO_4 ions on top of a CaP coating. In this chapter Sr is used as a marker for Ca ions. It is known that the ion exchange ratio for Sr to Ca is 1:1 in the adsorption layer [147]. The same strategy will also be employed in chapter 6. When Sr labels were used, rinsing was done with methanol.

The setup for the diffusion experiment and a theoretical background was outlined in section 4.2.1 and 4.1.1.

Coating depositions was done according to section 4.2.2. That is, coatings were sputtered on Si (100) from granulated HAP for 30 minutes at 600 W. An intermediate TiO_2 layer was applied as a bonding layer. A graded Ca/P ratio series was obtained as described in section 3.2.1. CaP layers were found to be between 60 and 80 nm thick from RBS. Samples were post-annealed for 30 minutes at 650°C to crystallize the coatings. Coated strips were cut into pieces of 1 cm^2 , and one of two adjacent samples was saved as a reference.

5.2.1 Scanning electron microscopy

Samples were sputter coated with carbon or Pt/Pd and examined with a Jeol 6310 or a Philips XL30SFEG scanning electron microscope. Images were acquired by detecting the emission of secondary electrons. An acceleration voltage of 15 kV was applied, unless stated otherwise.

5.3 Heat-treated coatings in SBFs

5.3.1 Formation and growth of a precipitate

After annealing for 30 minutes at 650°C, samples were immersed in SBF₁ and SBF₂. Heat-treated coatings immersed in SBF₁ did not show any change even after immersion for more than 3 days. RBS did not show an increase or decrease in coating thickness or a change in composition. For immersion of heat-treated CaP samples in SBF₂ it was found that a precipitate was formed. Figure 5.1 shows RBS spectra of the heat-treated coatings after immersion in SBF₂ for 90 min. We see that a CaP layer with a total coverage of $200 \cdot 10^{15}$ at./cm² was deposited on top of the coating. The slope of the

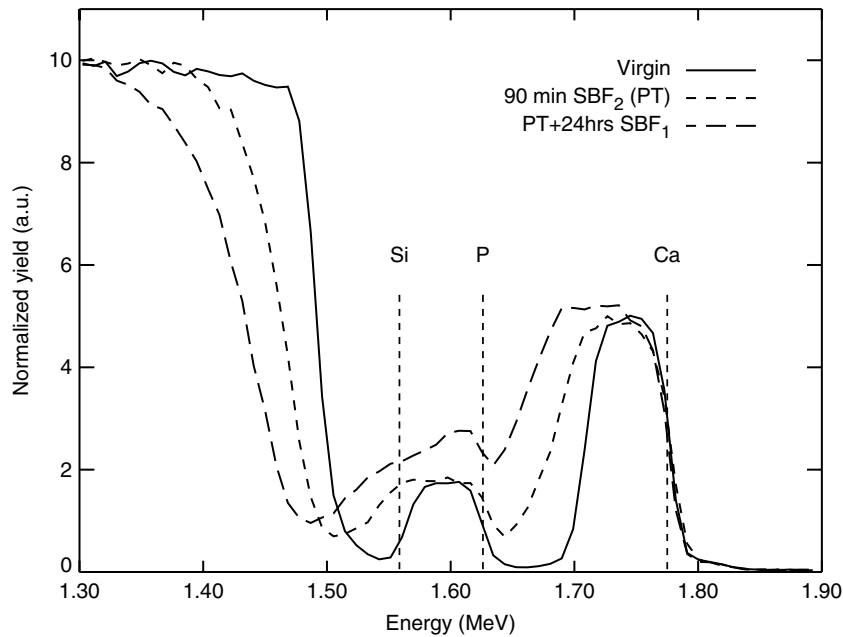


Figure 5.1: RBS spectra of a CaP-coating before (solid line) and after (broken line) 90 min of immersion in SBF₂ at room temperature. The long dashed line gives the spectrum after 24 hrs of subsequent growth in SBF₁. Surface energies are indicated for Ca, P, and Si. RBS: 2.4 MeV He⁺, $\theta=120^\circ$, $\alpha=94^\circ$.

back edges of the Ca and P signals and the front edge of the Si signal has become less steep, indicating considerable surface roughness.

The second column in table 5.1 shows the composition of the precipitated layer. We

Element	coating	precipitate
H	1.1	2.5
C	0.5	1.6
N	0.4	0.07
O	58.	58.
F	0.11	0.12
Na	0.08	0.04
Mg	0.12	0.14
P	15.	17.
Ca	25.	20.

Table 5.1: Atomic concentrations (in at.%) for various elements from ERD and RBS. The first column gives the concentrations of the annealed coating, the second gives precipitated layer concentrations. Errors were estimated at 5-10% of the given values.

see that the Ca/P ratio of the precipitated layer is ~ 1.2 , markedly lower than the Ca/P ratio of ~ 1.6 of the coating. We also see that hydrogen and carbon are incorporated into the crystals, probably as CO_3 and OH. Further, only very low amounts of Mg could be detected in the precipitate. From RBS, also no considerable amounts of Cl were found.

Figure 5.2 **b** shows a SEM micrograph of a heat-treated CaP coating after 90 minutes of immersion in SBF_2 . Note that the complete surface is covered with ~ 500 nm sized, honeycomb-shaped clusters of crystals that were not present on the virgin coatings (5.2 **a**). Little change could be observed in the XRD patterns (not shown) before and after immersion in SBF_2 . This could be due to the fact that the deposits are mainly amorphous or have an apatite structure that is lost in the coating signal. However, from about 70 minutes of immersion, a clear peak can be distinguished at 26.3° and 30.8° . It is not known yet which phase causes this extra reflection to appear.

Immersion at different Ca and PO_4 concentrations showed that at least $\text{SBF}_{1.4}$ is needed for the formation of a precipitate on these CaP coatings.

In the following, we will address the heat-treated coatings that were immersed for 120 minutes (or if indicated, for 90 minutes) in SBF_2 as *pretreated* (PT). To these pretreated coatings a 24 hour follow-up in SBF_1 was applied. In figure 5.1 the effect of the follow-up is plotted. It is clear that the CaP crystals keep growing in SBF_1 . In contrast, we observed that without this pretreatment no formation of CaP crystals is possible. We can calculate a rate of about $0.16 \cdot 10^{15}$ at./ cm^2 min^{-1} . No significant change in composition could be determined from RBS as compared with the pretreated

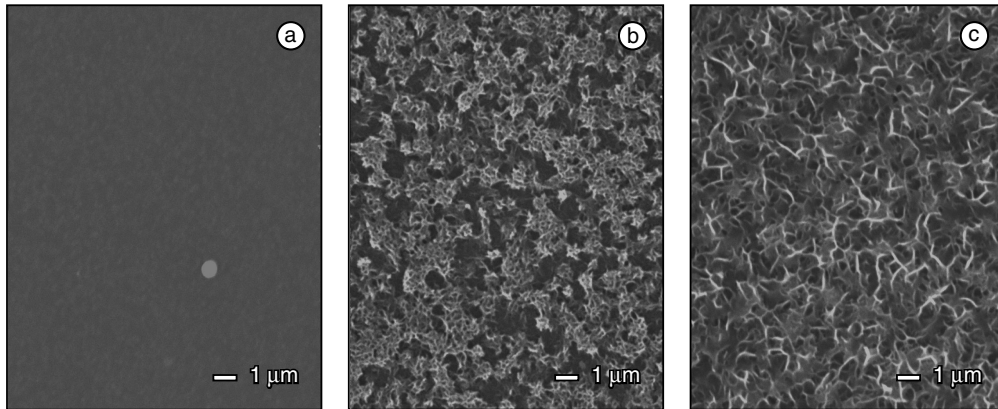


Figure 5.2: SEM micrographs of 400 W CaP samples after different treatments. **a)** After heat treatment. **b)** After 90 min of pretreatment in SBF_2 . **c)** After pretreatment and a follow-up of 24 hours in SBF_1 .

coatings. We see from SEM (figure 5.2 **c**) that after prolonged immersion the clustered crystals evolve into micron-sized platelet-shaped crystals. XRD did not show clear changes in crystallinity after the follow-up in SBF_1 .

Summarizing, in this section we gave a crude impression of the behavior of CaP coatings with a Ca/P ratio of ~ 1.6 in SBF_x at room temperature. We saw that the formation of CaP crystals is possible in SBF_x with $x > 1.4$. Subsequent growth is possible at concentration as low as SBF_1 . In the next section we report on the influence of the coating composition on the ability to form CaP crystals on its surface.

Influence of bulk composition

Immersion studies were also performed on coatings of different composition. CaP coatings with Ca/P ratios other than the ~ 1.6 used in the previous section were prepared as described in section 3.2.1. Samples were immersed in SBF_2 for two hours. In figure 5.3 the RBS results are plotted before and after immersion. Only the coating with a Ca/P ratio of 2.3 showed the formation of a precipitate within 2 hours. The other coatings remained inert for this period. Figure 5.4 shows an overview of some of the different Ca/P ratios that were used over time. It is also indicated whether these coatings allowed the formation of a precipitate within two hours under the conditions as mentioned above. In the schematic figure, the reciprocal time is plotted that is needed to form a precipitate. The relevance of this time will become clear in the following.

We see that only coatings with a Ca/P ratio of about 1.4 to 3 show a precipitated CaP layer within two hours.

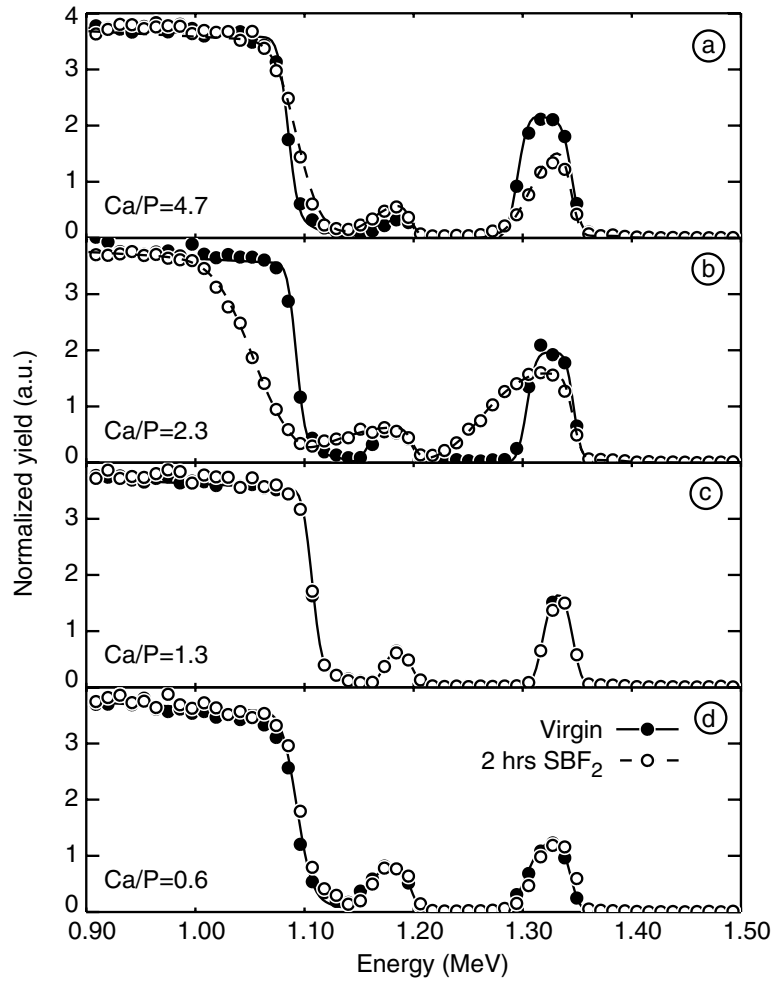


Figure 5.3: RBS spectra of CaP coatings with different Ca/P ratios immersed in SBF₂ for 2 hours. RBS: 2.0 MeV He⁺, $\theta=167^\circ$, $\alpha=94^\circ$.

In this study, also other metal oxides and ceramics were included. Uncoated silicon, Si/Si₃N₄, Si/SiO₂, Si/TiO₂, Ti, Si/Al₂O₃, Al₂O₃, and bulk HAP pellets were investigated. None of these materials showed any formation of CaP crystals on its surface within two hours of immersion in SBF₂.

Precipitation kinetics

In the following, we will concentrate on CaP coatings with a Ca/P ratio of ~ 1.6 , to guarantee the formation of a precipitate in SBF₂ within two hours. Figure 5.5 shows the equivalent layer thickness of the precipitated layer versus time for immersion in SBF₂ at room temperature. After an induction period of 40-60 minutes, where no significant apposition of material is observed, a sharp increase in the growth rate occurs, followed by steady and continuous growth.

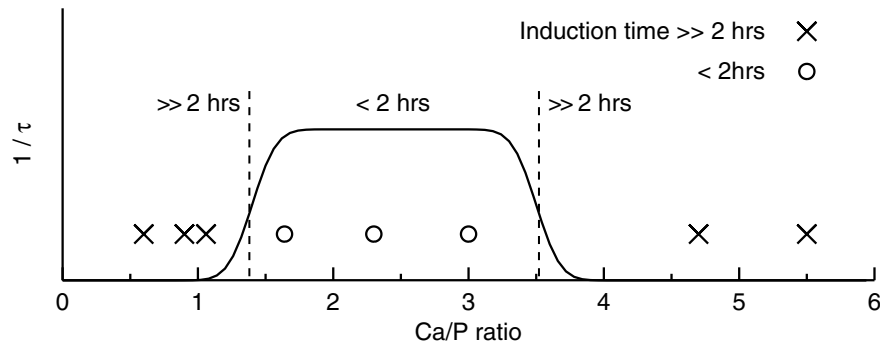


Figure 5.4: Schematic overview of the ability to nucleate CaP crystals on the coating surface as a function of Ca/P ratio. τ is the time required to precipitate a measurable amount of CaP.

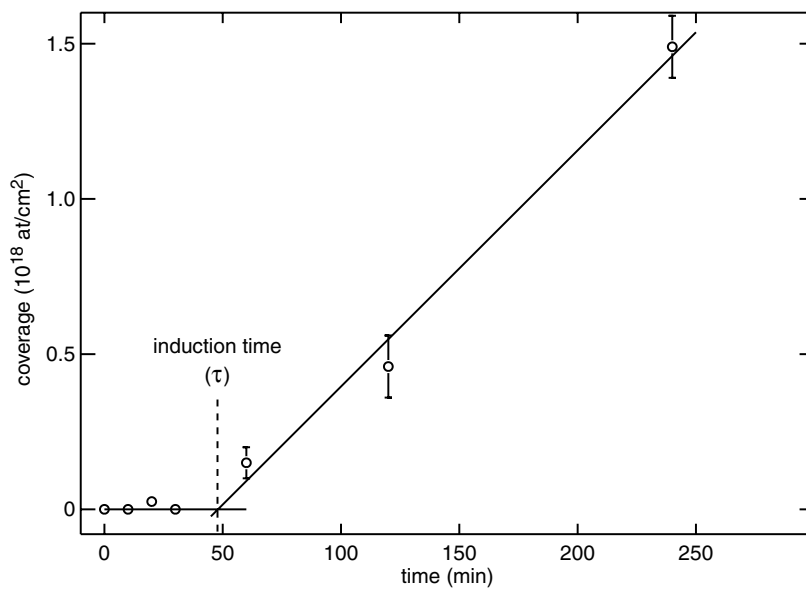
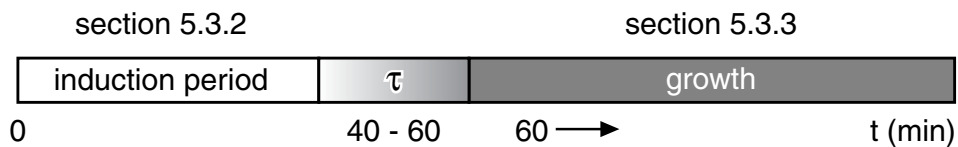


Figure 5.5: Precipitated layer coverage versus time for annealed CaP coatings after immersion in SBF₂ at room temperature.

In the following sections, we will discuss separately the events that take place during the induction period and the evolution of the CaP precipitate after the induction period.



In part I (section 5.3.2) the *induction period* (i.e., the first 40-60 minutes) will be investigated, in part II (section 5.3.3) we investigate the *growth period* (from ~60 minutes onwards).

5.3.2 Part I: the induction period

Deposits in the induction period

In figure 5.6 we see the electron micrographs of CaP coated samples after immersion in SBF₂ for 20, 40, 50, and 90 minutes (**a**, **b**, **c**, and **d** respectively). In figure 5.7 we see micrographs at a larger magnification for immersion periods of 20, 40, 60, and 90 minutes. We see that already after 20 minutes of immersion, i.e., in the induction period, deposits are found on the coating surface. Typical rod-shaped crystals of about 100 nm length and 10 nm diameter are identified, locally clustered in agglomerates. Little change in the amount of deposits is observed before the end of the induction period (figures **b**). We do see a slight change in morphology of the deposits towards more sheetlike shapes. After the induction time (figure **c**), three dimensional structures start to grow, resulting in a quite open honeycomb structure of thin sheetlike material. Finally, after 2 hours of immersion, plate-like structures like in figure 5.2 **c** are found. These experiments were repeated in different solution concentrations. It was found that after immersion periods ranging from 20 to 90 minutes, no deposits were found for immersion in SBF₁, nor in SBF₂ without either Ca or PO₄.

Composition of the deposits

To investigate the composition of the deposits we performed the following experiment. We immersed a CaP coated sample partly in SBF₂ for 30 minutes as depicted in figure 5.8. Glancing angle RBS measurements were done at different locations along the sample surface. Total CaP coverages were calculated from Ca back edge positions and are plotted as a function of sample position in figure 5.9. We can see a small step of $26 \cdot 10^{15}$ at./cm² in the total CaP coverage. The same step could be observed in the P back edge and Si front edge, but not in the Ca or P front edge. This clearly indicates that the deposited material consists of CaP. Assuming the deposits are CaP

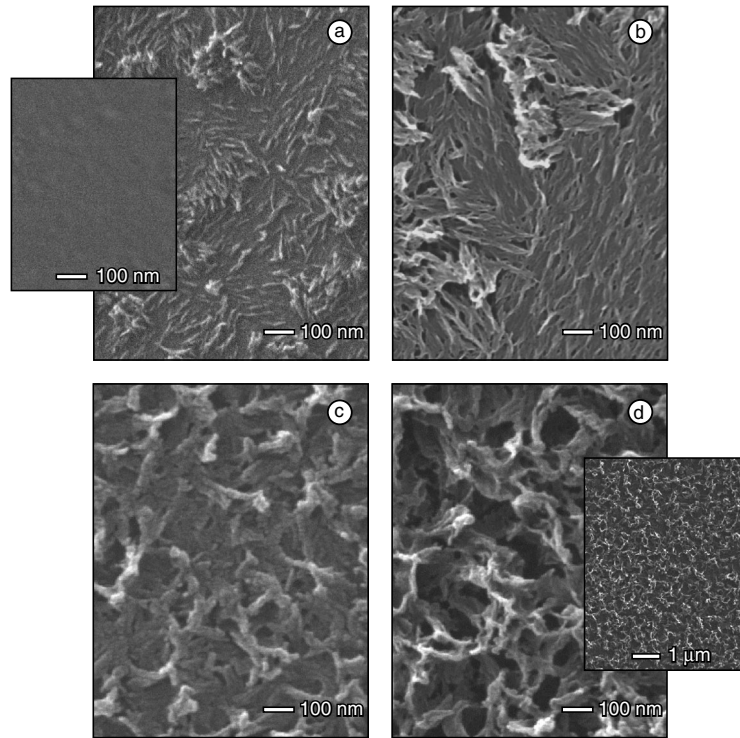


Figure 5.6: SEM micrographs of CaP samples after immersion in SBF_2 for different periods of time (magnification 160k). **a)** 20, **b)** 40, **c)** 50, and **d)** 90 minutes. The top left inset shows a non-immersed reference. The bottom right inset shows a sample after 90 minutes of immersion at a lower magnification.

crystals, we can also estimate the total coverage from figure 5.6 **a**. If we assume the rods to have an average length of 100 nm, a diameter of 10 nm and a coverage of $\sim 7 \cdot 10^{10}$ rods cm^{-2} (approximately 30 times 40 rods in 5.6 **a**), we roughly estimate a CaP coverage of $\sim 50 \cdot 10^{15}$ at./ cm^2 , in agreement with the result of figure 5.9. ERD showed no increase in C or N concentrations on the surface. We can thus conclude that the features observed on the CaP surface are most probably small CaP crystals.

Nucleation or sedimentation

It now remains to be investigated whether the rod-shaped deposits found shortly after immersion are involved in inducing the growth of CaP crystals after the induction time. Let us first try to reveal the origin of the deposits.

One possibility is that the rod-shaped crystals were formed on the coating surface. A lowering of the nucleation barrier by the presence of the CaP coating surface could

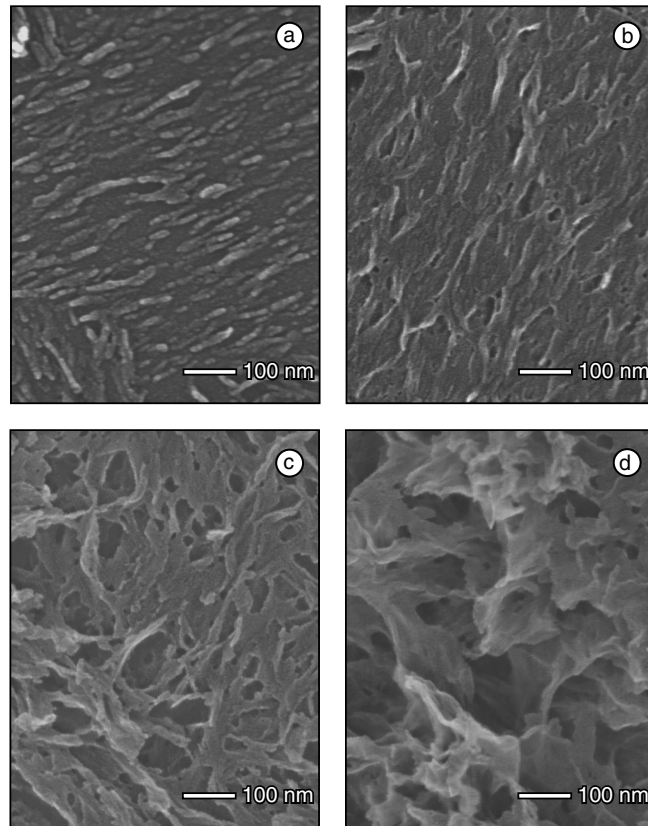


Figure 5.7: SEM micrographs of CaP samples after immersion in SBF_2 for different periods of time (magnification 320k). **a)** 20, **b)** 40, **c)** 60, and **d)** 90 minutes.



Figure 5.8: Setup of the glancing angle RBS experiment. A CaP sample is half-immersed in SBF_2 for 30 minutes. Glancing angle RBS measurements were done at positions on the immersed part of the coating and on the non-immersed part.

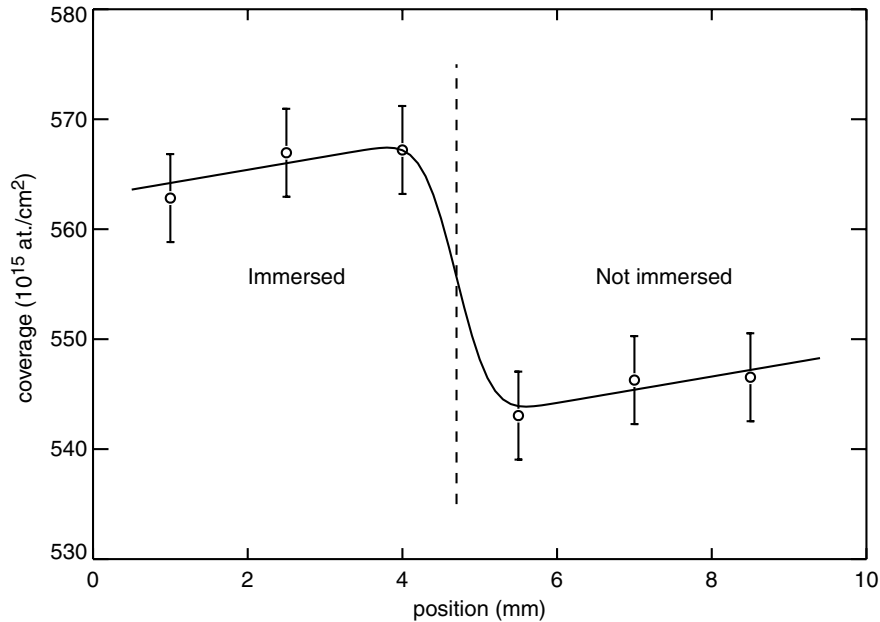


Figure 5.9: Total CaP coverage as a function of sample position for a CaP sample half-immersed in SBF_2 for 30 minutes. Coverages were calculated from Ca back edge positions in RBS profiles. The broken line indicates which part of the sample was immersed.

catalyze the formation of CaP nuclei on its surface. Another possibility is that the deposits are sediments from the solution. To discriminate between these hypotheses, we conducted the following experiments.

Firstly, Sr was added to the SBF_2 solution as a marker for the Ca ions. If the rods are formed at the coating surface, the amount of codeposited Sr ions reflects the total amount of deposited Ca. However, if the rods are already present in the solution, only adsorbed Sr contributes. Sr was added with a Sr/Ca ratio of 0.2, and samples were immersed in the labeled SBF_2 for 30 minutes. The experiment was repeated in SBF_1 with the same amount of Sr labels. The results of the RBS measurements after immersion and rinsing with methanol are plotted in figure 5.10. Sr coverages correspond to about $1 \cdot 10^{15}$ at./ cm^2 Ca ions, a typical coverage for a condensed adsorption layer, well below the $26 \cdot 10^{15}$ at./ cm^2 CaP as determined in figure 5.9. In chapter 6 we will find more evidence to support this number by the use of radionuclides, and confirm that the ion exchange ratio Sr:Ca is 1:1.

Further, we also observe that the average Sr coverage after immersion in SBF_2 is about 1.3 times higher than for immersion in SBF_1 , where no deposits can be found on the sample surface. The dash-dotted line corresponds to a CaP coated sample that was allowed to precipitate for several hours in a Sr labeled SBF_2 . It shows that it is possible for Sr ions to be coprecipitated in the CaP crystals, since Sr is found at depth

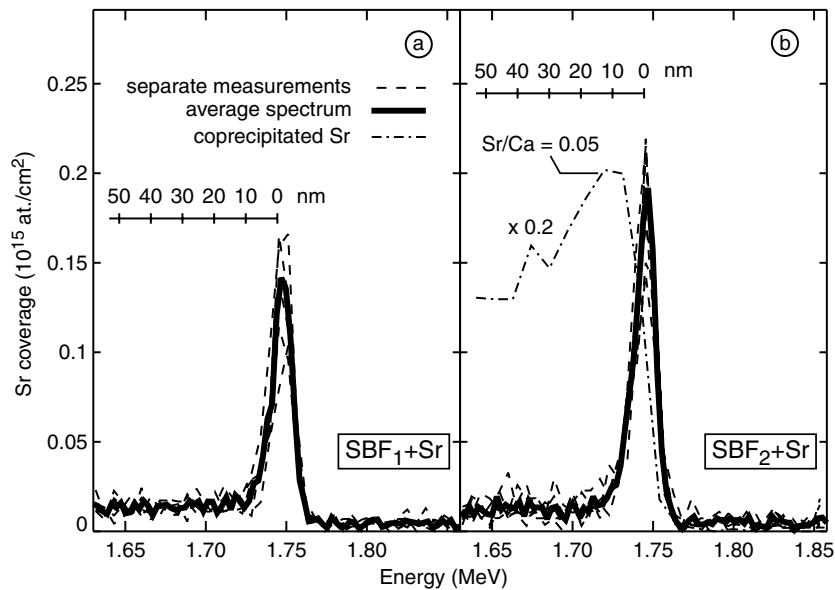


Figure 5.10: RBS spectra of the Sr label. Total Sr coverages are indicated on the y-axis. Depth scales are given for Sr contained in the coating. **a)** Sr coverage after 30 minutes of immersion in Sr-labeled SBF₁ and **b)** SBF₂. The average Sr coverage after immersion in SBF₂ is about 30% higher than for immersion in SBF₁. The dash-dotted line corresponds to the spectrum of a Sr codeposited CaP precipitate. RBS: 2.0 MeV He⁺, $\theta=120^\circ$, $\alpha=105^\circ$.

and there is no significant surface contribution to the Sr signal. Sr incorporation in the CaP crystals is four times lower than the Sr/Ca ratio in the solution.

Therefore, we conclude that it is possible to coprecipitate Sr in CaP crystals, but no Sr is coprecipitated in the deposits. Further, the adsorption of Sr labels is mainly governed by the CaP coating and not by the deposits. This leads us to the conclusion that the deposits are sediments from the solution, and are not formed on the coating surface.

Sediments and gravity

To investigate whether the accumulation of sediments on the surface is driven by gravity or otherwise (e.g. by surface charge), we designed the experiment as outlined in figure 5.11. Samples were immersed for 30 minutes in SBF₂ under different orientations. One sample was immersed with its sample normal upright, one to the side, and one upside down. Samples were rinsed, dried to air, and inspected using SEM (not shown). No differences in the shape, size, or coverage of the sediments could be observed. This indicates that the sample orientations is unimportant for the attraction of sediments to the CaP surface.

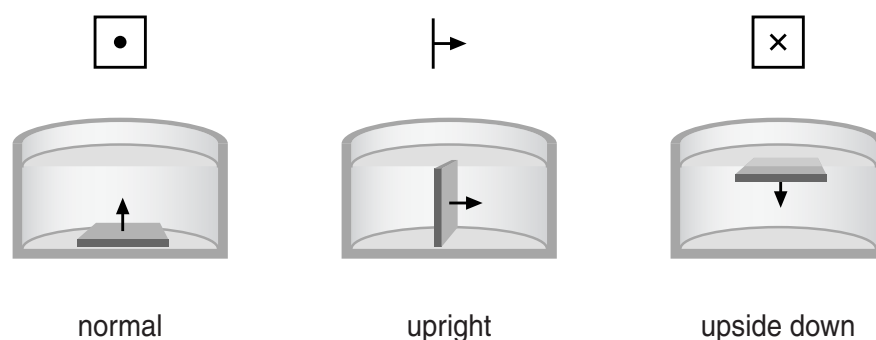


Figure 5.11: Setup of the oriented growth experiment.

Origin of the sediments

We have seen that the CaP crystals are most likely sediments from the solution and are not related to the immersion of the CaP coated sample. The sediments proved to be too small or their concentration too low to detect them in the solution using dynamical light scattering. They may have formed when the two stock solutions were mixed, or may have already been present in stock solutions themselves, and cluster together after mixing. To check this, we designed an experiment as outlined in figure 5.12. If the sediments are formed when the Ca and PO_4 stock solutions are mixed, we expect the order of addition of the Sr label and the Ca stock to influence the amount of Sr to be sorbed on the CaP surfaces after immersion. Therefore, one solution of Sr labeled SBF_2 was prepared by first mixing the Ca stock and the PO_4 stock, followed by the addition of the Sr label (**a**). Another labeled SBF_2 was prepared by adding the Sr label to the PO_4 stock and completed by the addition of the Ca stock (**b**). Both solutions were used for immersion of CaP samples for 30 minutes.

After immersion, no difference in deposited Sr could be observed between the two mixing orders (not shown). This suggests that the sediments did not form when the stocks were mixed, but were already present in the stock solutions. We hypothesize that undissolved fragments of the Ca and PO_4 salts cluster together upon mixing the stock solutions.

As mentioned above, when CaP coated samples are immersed in SBF_1 , no signs of sediments could be observed. An obvious experiment that comes to mind is to mix SBF_2 from the stock solutions, dilute it to SBF_1 concentrations, and immerse CaP coatings herein. Again, no sediments could be observed. It would be expected that the coverage of sediments would be halved, or even be unaffected by the change in concentrations, but instead, no sediments could be observed at all. Apparently, the sediments are very dynamic in nature and dissolve quickly when the solution is diluted. Yet it is unknown what the effect of coating composition is on the deposition of sediments.

Another indication of the dynamical nature of these sediments was obtained by

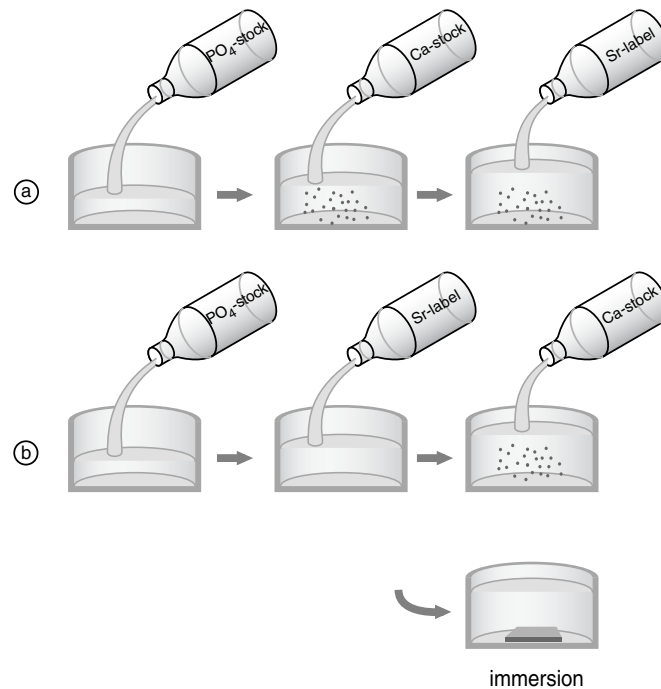


Figure 5.12: Setup of the mixing order experiment. Two different mixing orders were employed. **a)** First the PO_4 -stock is diluted with water, then the Ca-stock is added, and finally the Sr-label. **b)** Again, first the PO_4 -stock is diluted with water, then the Sr-label is added, and finally the Ca-stock.

filtering the SBF_2 solution with a pore size of 20 nm (Whatman, Anotop 25). No differences were found in sediment coverage of immersed coatings after 20 minutes of immersion in 20 nm filtered SBF_2 or 0.45 μm filtered SBF_2 . Also formation of CaP crystals was similar.

Summarizing, the deposits found on the CaP surface during the induction period preceding crystal growth are sediments from the solution. We also revealed that the sediments contribute up to a maximum of 30 percent to the early adsorption (refer to figure 5.10), which is governed by adsorption on the coating. The influence will probably be even less due to the lower bulk solution concentrations in the SBF_1 controls.

It remains unclear whether the sediments are involved in the nucleation of the CaP crystals that control the growth after the induction period. Obviously, when dispersed in the solution, the sediments are not able to show the rapid growth and clustering that is observed on the CaP coatings.

Activation and the induction period

In figure 5.13 precipitated layer coverages are plotted versus time for different temperatures. Again in **c** an induction period of 40-60 minutes can be observed. After the

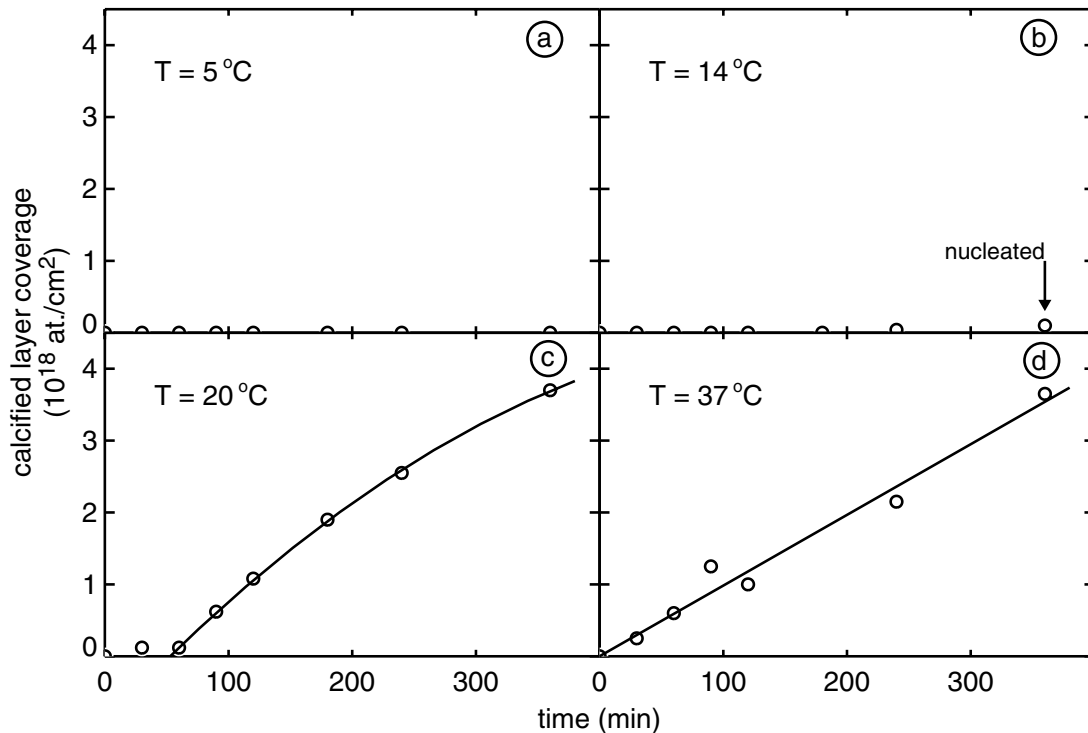


Figure 5.13: Precipitated layer coverages after immersion in SBF₂ versus time for annealed CaP coatings. Immersion at a) 5°C, b) 14°C, c) 20°C, and d) 37°C.

induction period, crystals start to grow at a rate of $\sim 1.5 \text{ nm min}^{-1}$ (or $12 \cdot 10^{15} \text{ at./cm}^2 \text{ min}^{-1}$). Also growth curves are shown for immersion at 5, 14, and 37°C. It is clear that the induction time before nucleation is very temperature sensitive. Furthermore, after the induction period, the growth rates at 20°C and 37°C are similar.

Another way to investigate the formation of crystals on the coating surface is to measure the scattered light intensity from the coating surface as described in section 2.4.2. It is to be expected that the sediments and the growing CaP crystals will give rise to Rayleigh scattering of the incident light. Since the scattering of the light is more efficient if the size of the scattering particle comes in the range of the wavelength, we expect first an increase of the scattered intensity in the short wavelength regime, followed by the larger wavelengths. If the size of the particles reaches the size of the wavelength of the light, the scattering efficiency becomes more or less independent of the crystal size.

In figure 5.14 a we see the fraction of light scattered into a detector placed under an angle of 90° with respect to the scattering plane, plotted versus time. Initially we see some scattering for all wavelengths. The smaller the wavelength the larger the scattered fraction, in agreement with equation 2.8. It is plausible that this initial scattering is caused by the attached sediments. After about 50 minutes, light at the

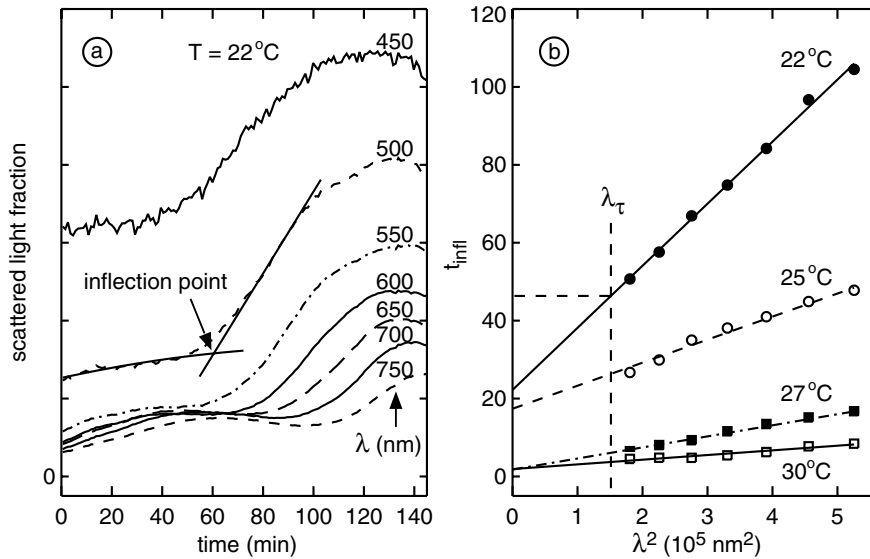


Figure 5.14: **a)** Scattered light intensity versus immersion time in SBF_2 for different wavelengths. **b)** Inflection times versus λ^2 for immersion at different temperatures.

smallest wavelengths starts to scatter more strongly, followed later by the larger ones. This sudden increase in scattered intensity is caused by the growth of CaP crystals after the induction period. By extrapolating portions of the curves in figure 5.14 **a** before and after the sudden increase in scattered intensity, we can define a point of inflection, and the associated inflection time. In figure 5.14 **b** we plotted for various temperatures the inflection points as a function of λ^2 , according to expression 2.11 for the scattered intensity. Combining expression 2.11 with 5.4 and assuming an Arrhenius type of temperature dependence allows us to derive an apparent activation energy from the data presented in figure 5.14 **b**. Induction times are determined at $\lambda = 400 \text{ nm}$, the wavelength corresponding to the induction time at 20°C from figure 5.13 **c**. A value of $\sim 250 \text{ kJ mol}^{-1}$ was calculated, much larger than expected for a precipitation or dissolution process. For example, for heterogeneous nucleation of OCP on TiO_2 powders we calculated a value of $\sim 21 \text{ kJ mol}^{-1}$ based on kinetic data by Wu and Nancollas [148]. Apparently, from our data, the temperature activated process(es) that control(s) the length of the induction period can not be described by a simple Arrhenius relation. Further, it is not clear yet which are the processes that are responsible for the induction period. However, light scattering experiments provide us with a valuable tool to study the kinetics of early CaP crystal formation *in situ*. With other techniques, like the use of ion-selective electrodes, this is hardly possible due to the low specific area of our CaP surfaces.

5.3.3 Part II: the growth period

Growth before and after completion of the induction period

We have seen that after a pretreatment for 120 minutes in SBF_2 , it is possible to continue the growth of CaP in solutions with lower Ca and PO_4 concentrations, e.g., SBF_1 (refer to figure 5.1). We have also established that without a pretreatment no growth is possible in SBF_1 . This suggests that the induction point at 40-60 minutes is discriminating between inertness and the possibility for further growth. In figure 5.15 the results of immersion in SBF_1 are shown after 25 and 90 minutes of pretreatment in SBF_2 . A pretreatment of 25 minutes is enough for the sediments to adhere, which

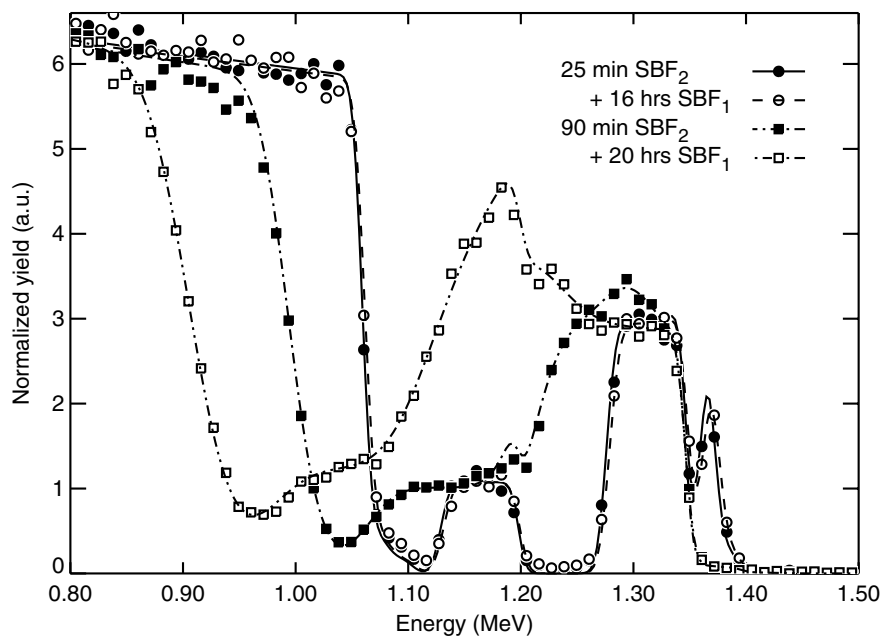


Figure 5.15: Growth in SBF_1 after 25 and 90 minutes pretreatment in SBF_2 . RBS: 2.0 MeV He^+ , $\theta=167^\circ$, $\alpha=94^\circ$.

is well below the induction period. We see that these surfaces are not able to allow further growth of CaP in SBF_1 . However, growth is observed with the 90 minutes pretreated samples, well past the induction period. This indeed confirms the hypothesis that completion of the induction period is decisive for further growth.

Sample orientation

To investigate possible gravitation effects on the growth of a CaP layer, the experiment outlined in figure 5.11 was repeated with CaP coatings that were first subjected to a pretreatment of 90 minutes in SBF_2 , all in the default upright position. After this, samples were again immersed in SBF_2 for several hours in the different positions as

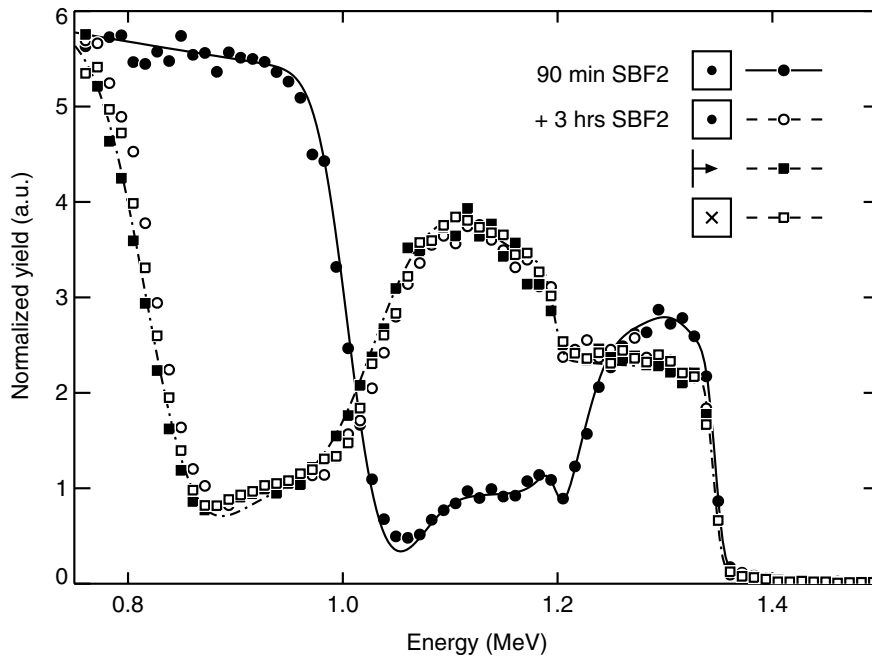


Figure 5.16: RBS spectra of CaP coatings immersed in different positions for 3 hours in SBF₂ after a pretreatment. RBS: 2.0 MeV He⁺, $\theta=167^\circ$, $\alpha=94^\circ$.

shown in figure 5.11. Results of the RBS measurements are shown in figure 5.16. We see that the amount of deposited CaP after growth under different orientations is exactly the same. Thus, we can conclude that orientation of the samples in the solution and gravitation do not influence the growth of a CaP layer.

Diffusion

To investigate the role of diffusion in the dissolution and growth processes of CaP, we used the experimental setup described in section 4.1.1 and 4.2.1.

The results of the rotating disk experiments for heat-treated coatings are shown in figure 5.17. In **a** the growth rate in SBF₂ is plotted as a function of the distance from the center of the disk, without (full circles and solid line) and with (open circles and broken line) rotating the disk. In **b** we see the corresponding results for growth in SBF₁. Since the strips were mounted in the same way during depositions, the radial distance corresponds to a thickness gradient as well. The growth rate in SBF₂ does not depend on coating thickness. For both growth in SBF₂ and SBF₁ we see that growth rates are lower for rotated samples than for non-rotated samples. We also observe that growth rates do not depend on the radial distance. This leads us to propose that growth kinetics are not diffusion-limited but most probably surface controlled. The reason why the growth rates drop significantly upon rotation is not clear, but it can be hypothesized that a part of the formed crystals is removed by frictional forces from the fluid.

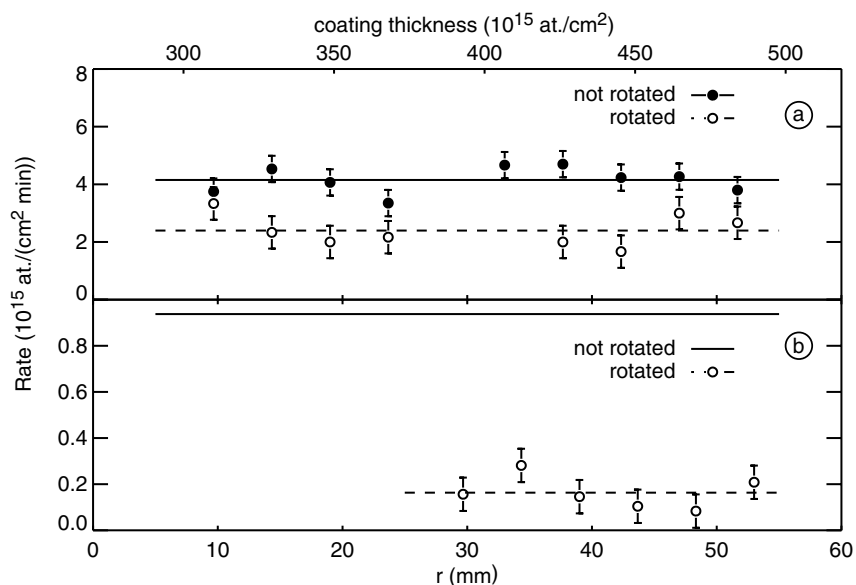


Figure 5.17: Growth rate versus sample position for CaP in **a)** SBF₂ and **b)** SBF₁ with (open circles and broken lines) and without (full circles and solid lines) rotation. Coating thickness is also indicated for the growth experiment in SBF₂.

5.4 Discussion

In this chapter we investigated how the RF-sputtered CaP coatings interact with solutions that mimic a physiological environment.

After a heat treatment of 30 minutes at 650°C, coatings with a Ca/P ratio of ~ 1.6 allowed the formation of a precipitate in SBF_{*x*} with $x > 1.4$. In SBF₁ these coatings remained inert. After initial formation of CaP crystals in SBF₂, further growth is possible in SBF₁.

Further, the effect of coating composition on the ability to form CaP crystals was investigated. Only within a certain range of Ca over P ratios crystals are formed. No other oxides or ceramics were found that showed induction times of less than two hours.

For immersion in SBF₂ at room temperature the formation of CaP crystals can be divided in two stages. First there is an induction period of 40-60 minutes, in which only little material is deposited from the solution, followed by a period where continuous growth of a CaP precipitate is observed.

During the induction time, sediments from the solutions are found on the coating surface. Their influence on the early adsorption process is limited, and their role as nucleation centers in the formation of the growing crystals during the induction time is still unknown.

In the last part of this chapter we found that the growth of CaP in SBF₁ and SBF₂ is

most likely limited by a surface related process.

Let us now treat the different aspects found in this chapter in somewhat more detail.

We found the heat-treated CaP coatings to be inert for days when immersed in SBF_1 . So, the most important factor that controls whether the coating dissolves or not, is the crystallinity, or to be more precise, the fraction of the CaP coating that has crystallized into an apatite phase.

Care should be taken with the term inert. As proposed in section 5.1.1, coatings that show induction times much longer than two hours are addressed as inert. This classification will be quite discriminative due to its high sensitivity for the surface free energies of the coatings as stated in equation 5.5. For immersion in SBF_x with x below 1.4, all CaP coatings were found to be inert. In literature no nucleation of CaP crystals has been reported in ordinary SBF_1 . Only for strongly leaching bioglasses precipitation of CaP can occur in SBF_1 . However, the question could be raised whether this should be addressed as SBF_1 . Because of the leaching, solution concentrations surrounding the bioglass exceed the concentrations of SBF_1 .

When immersed in SBF_2 at room temperature, the CaP coatings clearly show an induction period preceding the formation of CaP crystals. As we saw in section 5.1.1 this is a fingerprint for an activated, rate-limiting process. Indeed we see a strong dependence on temperature, saturation index, and coating composition. From the RBS data in figure 5.13 and the SLS data in figure 5.14 we clearly see that the induction time is decreased when the temperature is increased. We also observed that the growth rate after nucleation is not so much dependent on the temperature. This is a first indication that the growth in SBF_2 is not diffusion-limited. Note that the viscosity of water at 37°C drops to about 65% compared to water at 20°C . If the growth is diffusion-limited, it is expected that the growth rate would increase by about 60%.

The SEM observations in figure 5.6 and 5.7 interfere with a simple description of the nucleation process as described in section 5.1.1. Already after an immersion period of 20 minutes in SBF_2 , rod-shaped deposits can be found on the coating surface. From the glancing angle RBS measurements in figure 5.9 and the Sr-sorption data in figure 5.10 we concluded that the deposits found with SEM are CaP crystals originating from the solution and are not formed on the coating surface.

The SEM images suggest that agglomerates of the sediments form the growth centers for the crystals that are observed after the induction time. We saw that sediments on our CaP coatings are absent when immersed in SBF_1 . If the sediments are essential for crystal formation, this would explain why no materials have been found yet that show nucleation in SBF_1 . It should be stressed that if there is a relation between the sediments and crystal formation, it would be a collective effect. We showed that when no CaP coating surface is present, SBF_2 is stable for days. The ability of a material to form CaP crystals on its surface is then related to the efficiency to extract sediments from the solution and to cluster these in growth centers. The clustering then defines the induction period. On the other hand, it is also possible that the sedimentation and nucleation processes are completely independent. The growth centers for the observed CaP crystals after the induction period would be formed at the coating surface itself.

Therefore, the issue of heterogeneous versus homogeneous nucleation is difficult to solve. Clearly, the presence of a (CaP) surface is essential for the growth of a precipitate (heterogeneous), but so may be the presence of sediments in the solution (homogeneous). It may be the accumulation of the small sediments on the surface and their collective behavior that are the essential ingredients for CaP growth. However, it is clear that before and after the induction period of 40-60 minutes two different processes determine the crystal growth.

Filtering the solutions with a pore size of 20 nm showed no differences in sediment coverage on the coating surface, suggesting a very dynamical formation of the sediments. This is in agreement with the observation that no deposits could be found when samples were immediately immersed after dilution of SBF₂ to SBF₁ concentrations. However, no measurements have been done yet to verify the effectiveness of the filters.

From SEM observations, we conclude that the accumulation of sediments on the coating is not caused by gravitation. It is plausible that the surface charge of the coating and the sediments causes the accumulation.

Further, from the Sr sorption experiments in figure 5.10 we concluded that the effect of the sediments on the early adsorption behavior is only limited. Total Sr coverages after sorption in SBF₁ and SBF₂ are quite comparable. Most of the observed difference can be attributed to the differences in bulk concentrations.

After the induction period in which CaP crystals are formed, continuous growth is observed even when reimmersed in solutions with lower concentrations than SBF₂. It is important to note that the attachment of the sediments in itself is not enough to allow continuous growth of the CaP crystals. In figure 5.15 we showed that when the immersion of the CaP coatings in SBF₂ is interrupted before the end of the induction period, and the coatings are subsequently reimmersed in SBF₁, no growth is possible.

The formed crystals have a Ca/P ratio of about 1.2 as seen from RBS (see table 4.1). XRD did not show a large fraction of CaP phases other than the amorphous and apatite phase already present in the coating. The precipitate probably consists of (Ca-deficient) apatite or an amorphous phase obscured by the coating signal in XRD. Difficulties arise in the characterization of the precipitated phase for several reasons. Firstly, it is virtually impossible to apply diffraction techniques in situ, so the layers have to be dried before measuring. Also, the initially formed phase may have been transformed before it could be measured. Surprisingly, only very little Mg could be detected in the precipitated layer. Unlike Sr, which can easily be codeposited according to figure 5.10, Mg was almost not incorporated. Note that the Mg/Ca ratio in SBF₂ is 0.3, but in the precipitate only $7 \cdot 10^{-3}$.

In figure 5.3 we showed the importance of the CaP coating composition on the possibility to form CaP crystals from SBF₂. Only within a certain window of Ca/P ratios the induction time is shorter than 2 hours. It was shown that other oxides like SiO₂, TiO₂, and Al₂O₃ do not induce CaP crystal formation. This observation indicates that it is not very likely that the accumulation of sediments from the solution by surface charge is exclusively responsible for precipitation. In fact, from RBS also a small

amount of CaP ($\sim 5 \cdot 10^{15}$ at./cm²) deposits was found on Si/Al₂O₃ coatings.

For the diffusion experiments, we did not find an increase in growth rate of CaP crystals in SBF₁ or SBF₂ when samples were rotated. Together with the observation that the growth rate does not depend so much on the temperature, we conclude that the growth rate of CaP crystals is limited by a surface process rather than by diffusion. The reason for the decrease in growth rates observed in figure 5.17 is not completely clear. However, frictional forces can remove material from the growing surface or remodel it. Since this effect would be independent of the solution concentrations, it is indeed to be expected that the effect would be more pronounced for a slowly growing surface (in SBF₁), than it would be for a rapidly growing surface (in SBF₂).

5.5 Conclusions

We have given an overview of the influence of the various physical parameters that control the dissolution and precipitation processes of RF-sputtered CaP coatings in simulated body fluids.

Clearly, before the formation of CaP crystals on the coating surface in a physiological environment can be achieved, nucleation has to be activated, e.g., by increasing the lattice ion concentration of Ca and PO₄ in the SBF. After crystal formation is activated, growth can proceed at physiological conditions.

The precise mechanism that determines the first formation of CaP crystals remains unclear. Possible candidates are: heterogeneous nucleation of the coating or the formation of agglomerates of solution sediments.

Adsorption

6.1 Introduction

In section 3.3 we studied the thermodynamics of dissolution and the precipitation of CaP phases in simulated body fluids (SBFs). It should be emphasized that this approach does not account for surface effects. Since the processes that we study, like dissolution and nucleation, are fundamentally related to the surface, we investigate in this chapter what the implications of the CaP coating surface are on the adjacent solution layer.

The CaP oxide surface is negatively charged in SBF and provides (specific) adsorption sites for potential-determining ions in the solution. At immersion of the coating in SBF, surface complexes and an electrical double layer are formed, and the surface charge is screened in the solution. This influences the composition and structure of the solution near the surface, and thus the boundary conditions for nucleation and growth of CaP crystals, and related to this, its biocompatibility.

Lack of a successful quantitative model for ionic adsorption on CaP surfaces from SBFs, and the limited availability of complexation data for Ca and PO_4 on CaP surfaces, have led us to adopt an empirical approach.

In a first set of experiments, we focus on how the composition of the coating surface is related to the nucleation of CaP phases from SBFs. Firstly, we introduce the techniques that are necessary to obtain the required sensitivity and discrimination to probe the adsorption layer.

After this, we concentrate on the composition of the adsorbate itself, again related to the coating surface composition, and we also address the reversibility of the adsorption.

Finally, we investigate the desorption properties during the induction period, i.e., the period preceding the formation of CaP crystals (refer to section 5.3.1).

6.2 Adsorption and the electrical double layer

In general at the interface of a charged solid and a solution, positive and negative charges are aligned on both sides of the interface. The resulting charge distribution extending in the solution is called the electrical double layer (EDL). In figure 6.1 the general structure of this EDL according to the Gouy-Chapman-Stern-Graham (GCSG) model is depicted together with the associated terminology.

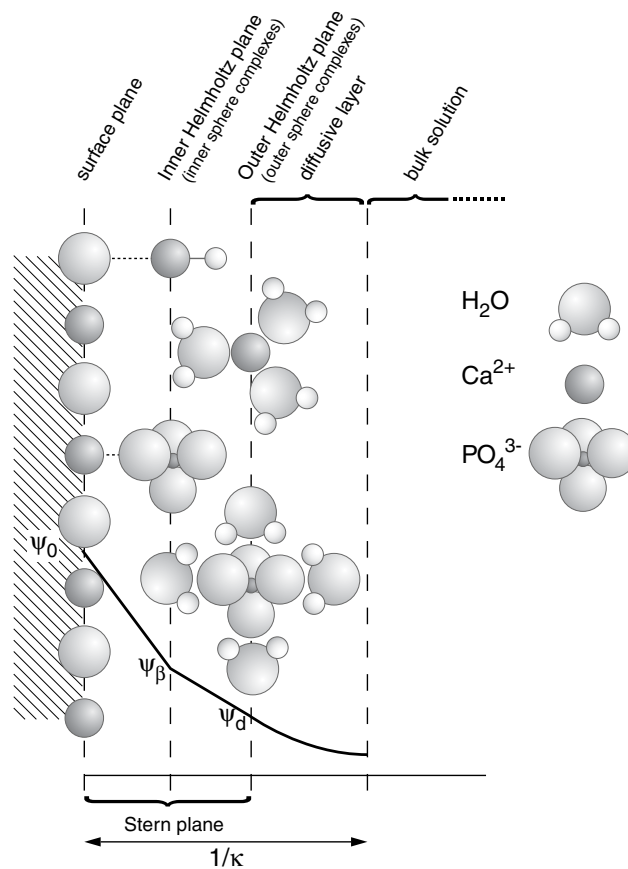


Figure 6.1: Structure of the electrical double layer according to the Gouy-Chapman-Stern-Graham (GCSG) model. The different layers are indicated together with their corresponding potentials ψ_x . The surface potential falls off to ψ_0/e over a distance of $1/\kappa$, the Debye length.

It consists of the *surface layer*, a layer of potential-determining ions in the solid that interact with the solution. Directly next to it are the specifically sorbed, tightly bound

ions without a hydration shell in the so-called *Inner Helmholtz Plane* (IHP). The first plane of ions that carry a hydration shell and are still tightly bound to the surface is designated as the *Outer Helmholtz Plane* (OHP). The region in the solution where the surface potential falls off to ψ_0/e ($\sim 0.37 \psi_0$) is called the *diffusive layer*. This distance is called the Debye length $1/\kappa$; κ is the Debye reciprocal length parameter given by:

$$\frac{1}{\kappa} = \sqrt{\frac{\epsilon_0 \epsilon_r kT}{2ne^2 v^2}} \approx \frac{3.04 \cdot 10^{-8}}{v \sqrt{c}} \text{ cm @ } 298^\circ\text{K}, \quad (6.1)$$

with n the number of electrolyte ions per volume, v the valence of the electrolyte ions, $\epsilon_0 \epsilon_r$ the dielectric constant of the medium, and c the concentration of the electrolyte in M. In SBFs the ionic strength is governed by the NaCl electrolyte, resulting in a Debye length of about one nanometer.

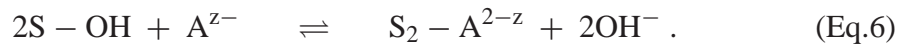
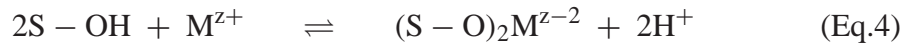
The charge separation between the different planes gives rise to three capacitances: between the surface layer and the IHP (C_1), between IHP and the OHP (C_2), and between the OHP and the bulk solution (C_d). The total capacitance of the adsorption layer is:

$$1/C_T = 1/C_1 + 1/C_2 + 1/C_d. \quad (6.2)$$

If the capacitance between the IHP and the OHP is neglected (the Stern model), and high ionic strengths and surface potentials are assumed, the model simplifies to the constant capacitance model in which $C_T = C_1$.

In the diffusive layer ion concentrations are governed by the Poisson-Boltzmann equation; counterions are attracted to the surface and coions are repelled. The distribution of ions is strongly dependent on the (multi)valency of the ions. This separation of charges in the diffusive layer does not result in differences in the ion activity product (IAP), since in equilibrium the chemical potential is constant over the adsorption layer.

Sorption of ions as inner- or outersphere species can be modeled by a site-binding model. If S is a surface group, the following equilibria can occur:



For the sorption of ions from simulated body fluids on a CaP surface, S can be Ca or PO_4 , M is one of the cations present in SBF (Ca^{2+} , Mg^{2+} , Na^+ , K^+), and A one of the anions (PO_4^{3-} , CO_3^{2-} , SO_4^{2-} , Cl^-). Equilibria 4 and 6 are bidentate surface complexes in which only multi-valent ions are involved. All the reactions above have their own stability constant β_i .

A CaP surface is a multi-site amphoteric hydrolyzed oxide surface. Both the Ca and PO_4 surface sites can act as Lewis acid or base, and provide binding sites for both

cations and anions. The oxide surface is charged due to the acidity of the different surface groups. In view of this, we know for example from the observation that the isoelectric point for HAP is below the physiological pH of 7.4 [108, 149, 150], that in SBFs the net surface charge for HAP is negative.

James and Healy found that metal ions, like Ca^{2+} , retain their primary hydration sheath when adsorbed on oxide surfaces [151]. Thus, Ca is most likely sorbed non-specifically as an outersphere complex on CaP. PO_4 on the other hand can bind by a ligand exchange with the surface hydroxyl groups, and can be sorbed as an innersphere complex.

Somasundaran [152] showed convincingly that for a HAP surface in a Ca and PO_4 containing solution Ca, PO_4 , and OH are all potential determining, and should all be included when constructing an adsorption model for CaP. Models only including the surface acidity constants, like developed by Wu et al. [153, 154] and Bell et al. [149], can not describe the structure of the adsorption layer correctly for all pHs, and all Ca and PO_4 concentrations.

For the adsorption experiments in this chapter an immersion time of 10 minutes was used based on previous findings [155, 156]. Longer immersion times are impossible in SBF₂ due to the formation of nuclei. This immersion period is sufficient to allow simple adsorption (typical less than a minute), but does not allow equilibrium to be reached in ion exchange processes with coating species [157]. The acid strength of methanol is supposed to be too low to disturb the adsorption equilibrium on the CaP surface [156].

The pH controls precipitation in three ways. Firstly, it is a lattice constituent and is a member of the IAP (thermodynamics). Secondly, it influences the phosphate balance (thermodynamics), and thirdly, it determines the adsorption equilibrium by controlling the number of available surface sites.

6.2.1 Reprecipitation

A persistent theory on the mechanism of CaP formation on CaP coatings is the reprecipitation hypothesis [158, 159]. A schematic representation is depicted in figure 6.2. Briefly, upon immersion, coating species are released from the surface and enter the diffusive layer. If the release rate exceeds the diffusion rate, the IAP is increased, and the solution is locally supersaturated with respect to other, more stable, CaP phases. This oversaturation results in reprecipitation of these species in newly formed CaP crystals.

A similar mechanism was shown to be valid for the precipitation of CaP on CaCO_3 . Griffin and Jurinak [160] found that addition of phosphate to a calcite suspension resulted in fast adsorption and, after an induction period, CaP crystals were formed.

We can roughly estimate the desorption rate that is necessary for an oversaturation in the diffusive layer to be effective. Therefore, the concentration of desorbed ions should at least be of the order of magnitude of a few percent of the bulk concentrations.

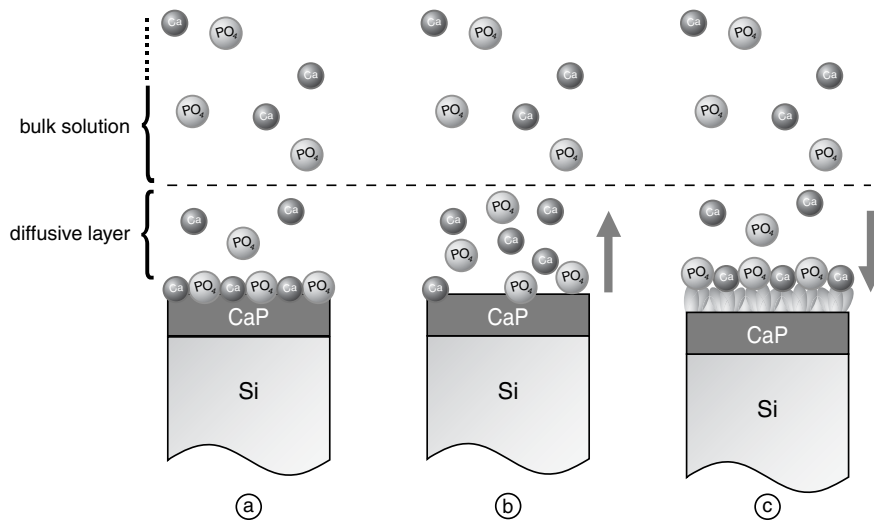


Figure 6.2: A suggested mechanism of CaP precipitation on CaP coatings. **a)** Coating is introduced in a Ca and PO₄ containing medium, **b)** coating species are dissolved, increasing the IAP in the diffusive layer. **c)** Stable CaP phases are reprecipitated on the surface.

If we take a diffusion coefficient of $\sim 10^{-6}$ cm²/s, an (overestimated) diffusive layer thickness of 10 nm, and bulk concentrations of a few mM, we deduce a minimum release rate of $\sim 10^{16}$ ions/(cm² s). Because no electrostatic interaction with the surface is included, the minimum release rate is probably even somewhat lower.

6.3 Experimental considerations

6.3.1 Setup of the experiments

To investigate the adsorption of Ca and PO₄ ions on CaP coatings we designed the following experiments. To determine the composition of the adsorption layer, CaP coatings were immersed in SBFs, rinsed, dried and examined. The followed procedure and the consequences for the structure of the adsorption layer is presented in figure 6.3. CaP coated samples were immersed in SBF₂ for 10 minutes. SBF₂ was used to allow the formation of CaP crystals on the surface of CaP coatings (refer to section 5.3.1). Then, samples were rinsed thoroughly with methanol and dried to air. Two strategies for analysis of the adsorption layer were employed. Firstly, adsorption layers were studied with low energy ion scattering (LEIS), an elastic, mass-dispersive keV ion scattering technique, most sensitive for the outermost atomic layer. Another approach that we applied was the use of radioactive isotopes to label the solution species and thus the adsorption layer species.

Therefore, CaP coatings were immersed in SBF₂ labeled with β -emitting isotopes

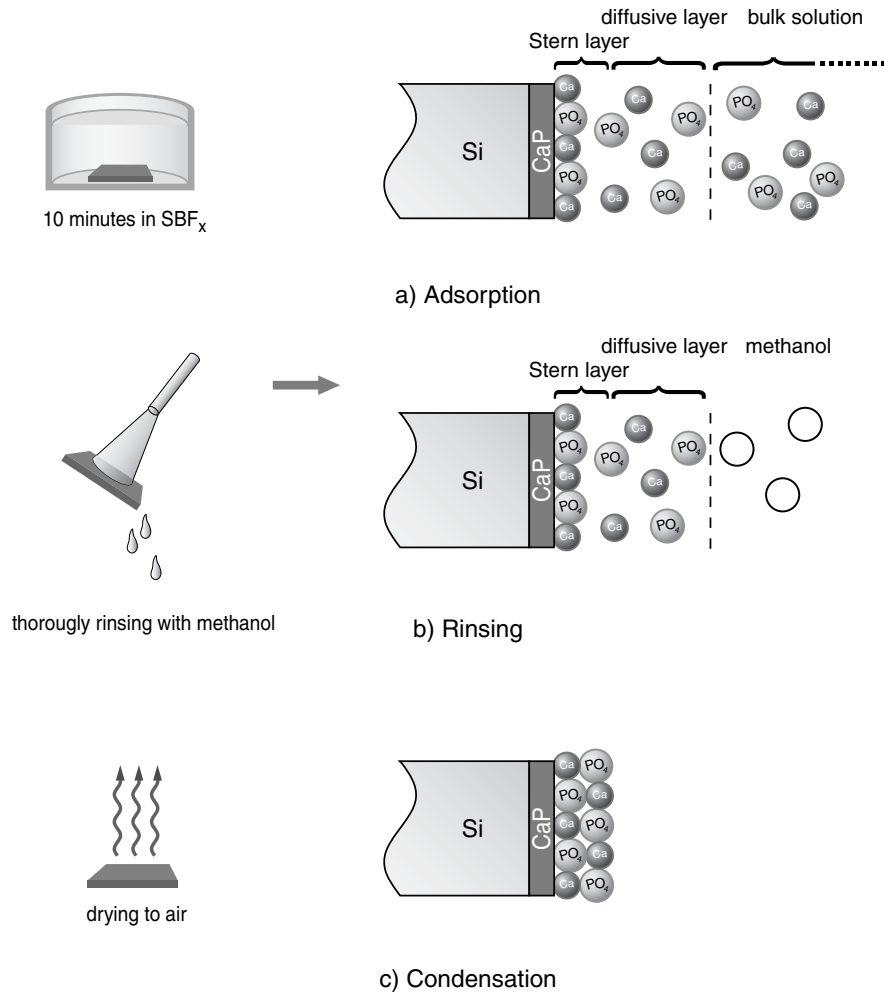


Figure 6.3: The adsorption procedure (left), and implications for the adsorption layer (right). **a)** 10 minutes adsorption in SBF_2 , equilibrating the structure of the adsorption layer. **b)** Rinsing with methanol, removal of the bulk solution. **c)** Drying of the coatings, condensation of the adsorbate.

for Ca and PO_4 . After completion of the adsorption process, coatings were rinsed and dried. By dissolving the coating in acid, the condensed adsorption layer with the adsorbed radiolabels is also be dissolved, and can be quantified with liquid scintillation counting (LSC). Since the efficiency of counting β decays is almost unity, the sensitivity of this technique is excellent. By labeling the solution species we were able to distinguish between Ca and PO_4 originating from the coating and Ca and PO_4 deposited from the solution.

6.3.2 LEIS

The advantage of LEIS is, besides its known surface sensitivity, that both the coating surface and adsorption layer can be probed with the same technique.

A 3 keV He⁺ was used with a spot diameter of 0.3 mm. Measurements were done at a beam current of 3.7 nA; sputter cleaning was done with the same beam at a beam current of 14 nA scanning over an area of 1 mm².

Due to the extreme surface sensitivity of the technique, hydrogen termination and adsorbed water had to be removed. A 15 minutes oxygen anneal at 300°C followed by 10 minutes sputter cleaning proved to be effective and reproducible. The effectiveness was concluded from a considerable increase in LEIS yield after the cleaning procedure. However, it is not possible to exclude partial removal of the surface CaP layer itself. Further, a temperature of 300°C is not sufficient to crystallize the coatings or any CaP deposit.

Differences in neutralization probabilities and unknown coordination of surface groups do not allow the establishment of absolute surface coverages from the LEIS results. However, relative differences or changes are well observable.

6.3.3 Radionuclides

⁴⁵Ca and ³²P are β -emitting isotopes of Ca and P and were used to label SBF₂ (Amersham Biosciences). In table 6.1 the decay properties of these isotopes are listed. In

Isotope	Mineral	Decay type	Half life (days)	Decay energy (MeV)
⁴⁵ Ca	CaCl ₂ ·2H ₂ O	β^-	165	1.72
³² P	KH ₂ PO ₄	β^-	14.3	0.256

Table 6.1: Decay properties of the Ca and P isotopes used to label the SBFs.

total, 1 ml of 90.8 $\mu\text{g Ca ml}^{-1}$ labeled CaCl₂·2H₂O in solution with an activity concentration of 2.5 mCi ml⁻¹, and 2 ml of 200 mCi mmol⁻¹ labeled KH₂PO₄ with an activity concentration of 1.0 mCi ml⁻¹ were added to complete two solutions of 20 ml of labeled SBF₂. Specific activities were supplied by the manufacturer and corrected to the proper activities at the time of use. Both solutions were diluted with SBF₂ to optimize count rates with liquid scintillation counting (LSC). These solutions are designated the Ca-stock and PO₄-stock. In the Ca-stock solution a fraction of $3.3 \cdot 10^{-5}$ of the Ca ions were labeled, for the PO₄-stock a fraction of $1.1 \cdot 10^{-6}$. Equal parts of the stock solutions were mixed to obtain a doubly labeled SBF₂, which is referred to as SBF₂^{*}.

Adsorption experiments were performed in 2 ml of labeled SBF according to figure 6.3. The rinsed and dried coatings were dissolved in 1 ml HCl and neutralized

with 1 ml NaOH/tris buffer to a pH of $\sim 6-7$ to give clear solutions. Two ml of this solution was transferred to a plastic vial and 15 ml of scintillation fluid was added (Ultima Gold, Packard). For measurement of the activities of the adsorbed species, liquid scintillation counting was used (LSC, Packard Tricarb).

In β -LSC, energetic electrons interact with the solvent of the scintillation fluid, exciting solvent molecules to emit UV photons, which in turn excite fluorescent solute molecules that generate blue light. The intensity is proportional to the energy of the electron and about 10 photons per keV are generated, which can be detected as flashes by a photomultiplier tube.

Scintillation intensities were measured in two energy windows: the Ca-window from 50-256 keV and the P-window from 300-1750 keV. Electron energies range from the decay energy (table 6.1) down to zero because of the simultaneous generation of an energetic antineutrino. This results in a significant background of the ^{32}P signal in the Ca-window.

All experiments were done in fivefold.

Calibration and quenching

Before the measurements were done, a series of test measurements was conducted to test the quenching behavior of the scintillation signal, to check linearity of the signal versus label concentrations and to calibrate the LSC yield to obtain absolute label concentrations.

In figure 6.4 the effects of dilution of the scintillation fluid (**a**), excess acid (**b**), and SBF_2 concentration in the sample solution (**c**), on the scintillation signal in the Ca and P-window are shown. All added solutions were labeled with 200 μl PO_4 -stock. Intensities are scaled at zero dilution, added acid, and SBF_2 concentration respectively. Figure **a** reveals that it is important that the sample volume that is added to the scintillation fluid is maintained constant for all experiments. In the adsorption experiment all added volumes were 2000 μl . In **b** and **c** the effect of excess acid and CaP concentration is plotted. Clearly, acid- and chemical quenching can be neglected. In the adsorption experiments, the Spectral Index of External Standard (SIE), an index related to the spectral distribution, was used to monitor differences in quenching behavior. No significant differences in SIE were found between the different experiments.

In figure 6.5 the scintillation intensity in the Ca- and P-windows is plotted for different label concentrations. Points were obtained by measuring serial dilutions of the Ca-stock and the P-stock with water. The x-axis gives the total number of Ca or PO_4 ions in solution, not just the labels. The slopes of the curves were used to convert scintillation intensities to absolute Ca and PO_4 contents. The inset in the figure shows a schematic view of the spectral energy distribution for ^{45}Ca , ^{32}P , and for a mixed label sample. When the contribution of the ^{32}P signal in the Ca-window is established, ion concentrations can be calculated for mixed label solutions as well. Backgrounds were well below 1% for all measurements.

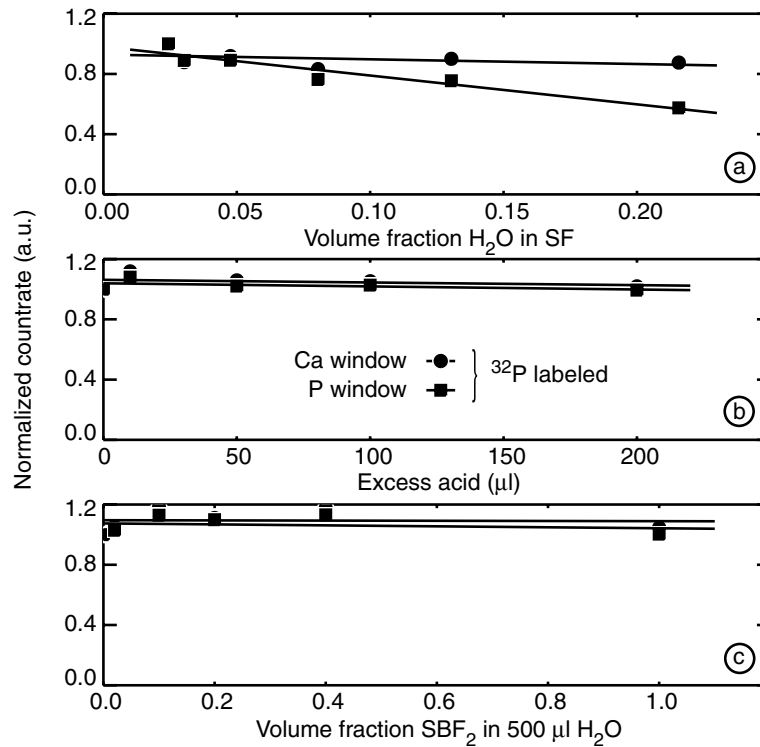


Figure 6.4: Effect of **a)** dilution of the scintillation fluid, **b)** excess acid (0.1 N HCl), and **c)** CaP concentrations on the count rate in the Ca and P window. Only a ³²P label was used in these experiments.

6.3.4 Coating application

Coating depositions was done according to section 4.2.2. That is, coatings were sputtered on Si (100) from granulated CaP for 30 minutes at 600 W. CaP layers were found to be between 60 and 80 nm thick from RBS. Samples were post-annealed for 30 minutes at 650°C to crystallize the coatings. Coated strips were cut in pieces of 1 cm².

One set of coatings, named CaP_{high}, was sputtered from HAP as a target material, and its Ca/P ratio was found to be ~1.6 from RBS. Another set of coatings, CaP_{low}, was prepared by sputtering from two granulated pyrophosphate targets (refer to section 3.2.1), and showed a Ca/P ratio of ~0.8.

Immersion studies with the CaP_{high} and CaP_{low} coatings revealed that CaP_{high} coatings nucleated within 2 hours in SBF₂ and showed the formation of CaP crystals on the coating surface as we saw earlier in section 5.3.1. CaP_{low} coatings do not result in nucleation and growth of crystals within this time span.

When measuring the amounts of adsorbed ions as described in section 6.3.3, any contribution of ions adsorbed on the rough backside of the Si substrates has to be avoided. Therefore, doubly polished silicon (100) substrates, coated on both sites, were used for the radiolabel experiments. To ensure identical adsorption on front- and backside, coatings were placed in an upright position in the wells (like in figure 5.11 **b**).

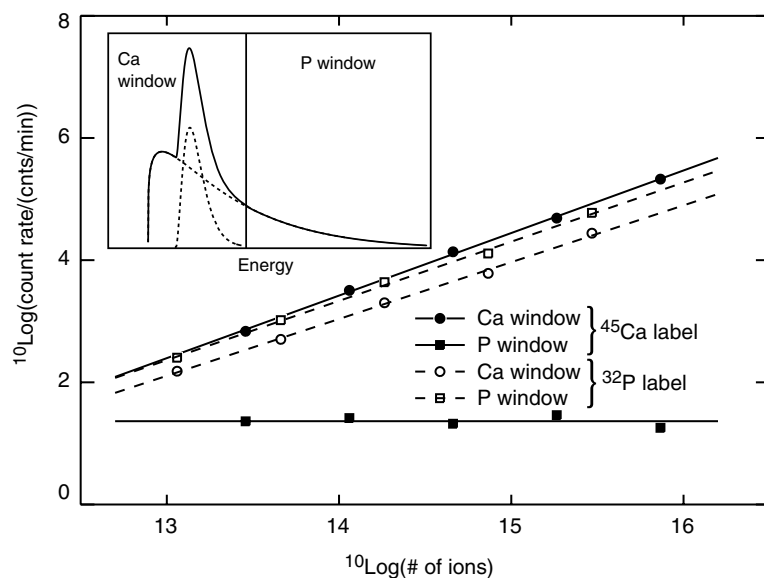


Figure 6.5: Scintillation intensities versus total Ca concentration (for the Ca label) or versus total PO_4 concentration (for the ^{32}P label), for the Ca and the P windows. Inset: Spectral distribution for ^{45}Ca , ^{32}P , and a mixed label solution.

6.4 Adsorption

In figure 6.6 the LEIS spectra for a CaP_{high} and CaP_{low} sample are given before and after immersion for 10 minutes in 10 ml SBF_2 . Peak positions for Ca, P, Mg, Na, and O are indicated. The peak at 1490 eV in the CaP_{low} spectra is due to a few at.% bulk sodium contamination as confirmed by ERD. Due to the low P signal we assume in the following that the majority of the oxygen yield is from phosphate groups, and thus we use the larger oxygen signal as a measure for the number of phosphate groups. The non-immersed reference spectra show that at the outermost atomic layer the Ca/ PO_4 ratio is indeed higher for the CaP_{high} samples than for the CaP_{low} samples. When we compare the Ca over O peak area ratio for the CaP_{high} and CaP_{low} samples, we find similar values as with RBS. Thus, we see that the termination of the CaP lattice is related to the bulk composition. Evidently, this is an essential condition if we want to investigate the effect of bulk parameters on surface properties.

We also compared the LEIS spectra for non-immersed CaP_{high} samples before and after the heat treatment of 30 minutes at 650°C (not shown). These were almost identical, indicating that such an anneal did not induce changes in the surface composition.

Further, figure 6.6 demonstrates that the Ca over PO_4 peak area ratio for CaP_{high} has decreased after 10 minutes of immersion in SBF_2 . On the other hand, for the CaP_{low} samples an increase in the Ca over PO_4 peak area ratio is seen. Because the contribution of the underlying coating to the elemental yields is not clear, this effect might even be partly masked. It might even suggest that the Ca over PO_4 ratios in the

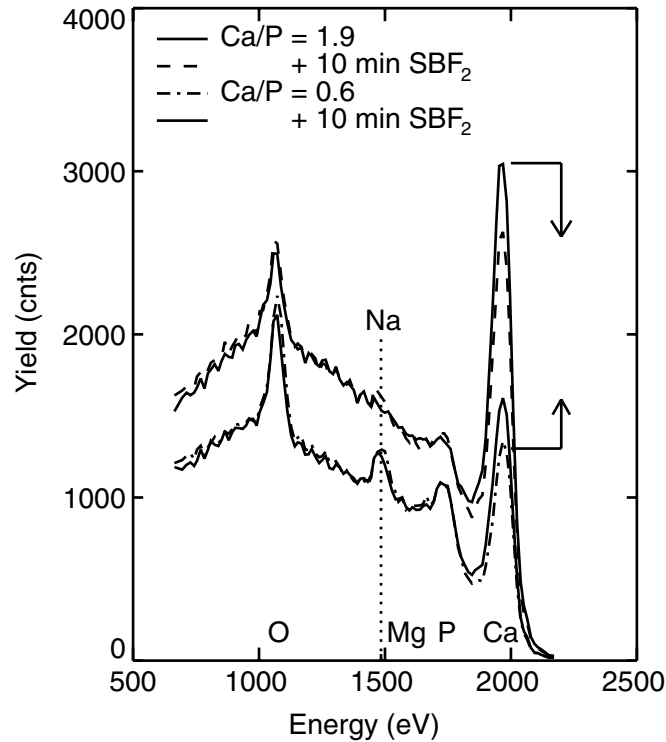


Figure 6.6: LEIS spectra for CaP_{high} and CaP_{low} samples before and after immersion for 10 minutes in SBF_2 .

adsorption layer are the same for both sample groups.

We have noticed that for both the CaP_{high} and CaP_{low} samples no significant amount of Mg could be detected on the surface after 10 minutes immersion. The Mg over Ca ratio in SBF_2 is 0.3, so we can conclude that Ca is preferentially adsorbed over Mg. These findings are also supported by the ERD results for the precipitate compositions in section 5.3.1. It is known that in the HAP crystal lattice only a limited amount of Mg can be incorporated.

The results of immersion of CaP_{high} and CaP_{low} samples in SBF_2^* are listed in table 6.2. All differences between the CaP_{high} and CaP_{low} adsorption numbers are significant. The Ca and PO_4 coverages are in the right order of magnitude for monolayer adsorption, which suggests that no significant precipitation has occurred. Nevertheless, the variance in the adsorption numbers is considerably larger than the variance in the Ca/P ratios. This might be explained by small differences in coating surface area, rinsing procedure, or the amount of residual adsorption species after dissolving the coating. These effects influence the absolute adsorption numbers, but cancel out if we calculate the Ca/P ratios and therefore do not contribute to the variance. The Ca and PO_4 adsorption coverages for CaP_{low} samples show that the adsorption for Ca is about halved and the PO_4 coverage is about 1/4 of the coverages found for the CaP_{high} coatings. The Ca/P ratio of 2.17 for the CaP_{low} coatings is considerably closer to the bulk

Sample	bulk Ca/P	Adsorbate					
		Ca 10 ¹⁵ ions/cm ²	Average Ca 10 ¹⁵ ions/cm ²	P 10 ¹⁵ ions/cm ²	Average P 10 ¹⁵ ions/cm ²	Ca/P	Average Ca/P
CaP _{high}	~1.6	1.01		0.83		1.21	
		1.40		1.14		1.23	
		1.03		0.82		1.25	
		1.15		0.90		1.27	
		1.17	1.15±0.16	0.96	0.93±0.13	1.22	1.24±0.02
CaP _{low}	~0.8	0.56		0.26		2.13	
		0.77		0.33		2.35	
		0.46		0.22		2.12	
		0.43		0.20		2.15	
		0.47	0.54±0.14	0.22	0.25±0.05	2.13	2.17±0.10

Table 6.2: Ca and PO₄ coverages in the adsorption layer on CaP_{high} and CaP_{low} coatings after 10 minutes immersion in SBF₂* calculated from label activities.

ratio of 2.5 for SBF than the 1.24 for CaP_{high}. The latter corresponds closer to the ratios for possible CaP precursor phases, like DCPD (Ca/P=1.00) and OCP (Ca/P=1.33), or a Ca deficient apatite. Surprisingly, this would imply that PO₄ species are more abundant in the adsorption layer than Ca, although it is known that (apatitic) CaP layers possess a negative surface charge at this pH. This implies that PO₄ species are specifically adsorbed.

Ca and PO₄ coverages are plotted versus time in figure 6.7 for both the CaP_{high} and CaP_{low} sample groups. Each data point is the average of two samples. Evidently, for both sample groups the majority of the ions are adsorbed within the first two minutes after immersion. Thereafter, on the CaP_{low} samples only a small increase in the adsorbed coverage could be observed, probably due to ion exchange processes. The CaP_{high} data scatter considerably compared to the CaP_{low} data. Currently, we do not know whether this is due to experimental errors or to factors related to the adsorption process or structure of the adsorbate.

After 40 minutes a steep increase in the Ca and PO₄ coverages is observed for the CaP_{high} samples, indicating the formation of CaP crystals. This confirms the existence of a clear induction time before a significant growth rate of CaP is obtained. The coverages at 40 minutes are of special interest because they allow the accurate calculation of the Ca/P ratio during early crystal formation (at ~ 25·10¹⁵ at./cm² or ~4 nm). We calculated a value of 1.30 ± 0.02, in agreement with the RBS data in section 5.3.1. This value corresponds within the error with the Ca/P ratio of 1.33 of OCP, a known precursor phase. Ca/P ratios in this range have also been reported for Ca deficient apatites [16]. Further, the measured Ca/P ratio for the precipitate is significantly higher

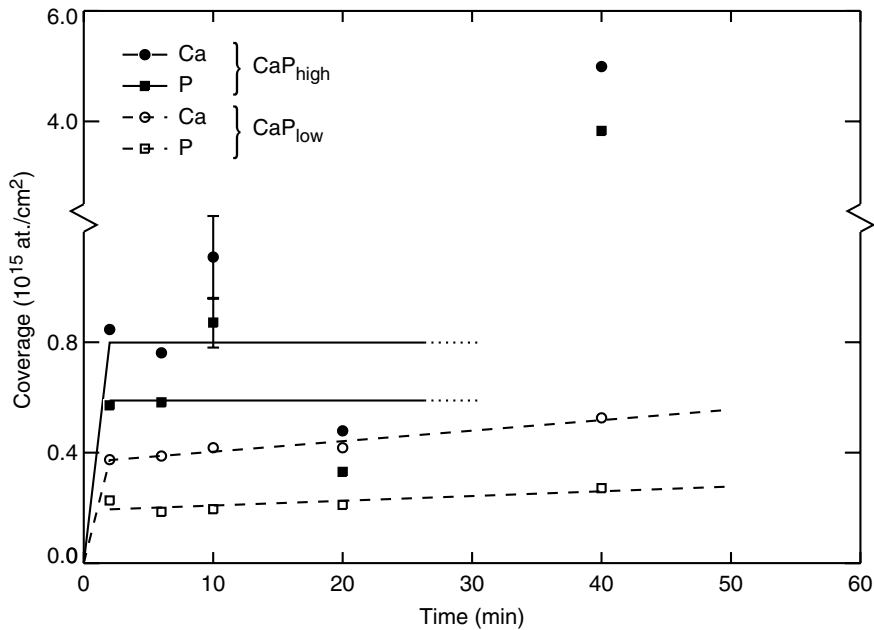


Figure 6.7: Ca and PO₄ coverages in the adsorption layer on CaP_{high} and CaP_{low} coatings versus time for immersion in SBF₂* calculated from label activities. After 40 minutes immersion, the CaP_{high} samples show a sharp increase in sorbed species indicating growth of crystals.

than the Ca/P ratio found for the adsorbate.

For the correct interpretation of the adsorption results as obtained using the radiolabeling, we have to distinguish between adsorption and early nucleation. To investigate this, we did an additional adsorption experiment. However, instead of radioactive labels, Sr and SeO₃ were used as markers for Ca and PO₄ respectively. It is known that Sr exchanges reversibly with Ca and SeO₃ with PO₄ in a 1/1 ratio [147, 161].

Our hypothesis is that when (supercritical) nuclei are formed, the markers are codeposited in the CaP crystal. After subsequent re-immersion of the same samples in non-labeled SBF₂, only a limited fraction of the codeposited markers is able to exchange with solution species. Therefore, the sorption of these markers would be highly irreversible. On the other hand, if only simple adsorption occurs, a considerable fraction of the adsorbed species is expected to desorb upon re-immersion.

Consequently, CaP_{high} coatings were immersed for 10 minutes in SBF₂, with Sr/Ca and SeO₃/PO₄ ratios of 0.2. After rinsing and drying, samples were divided in half. One part was kept as a reference, the other part was re-immersed for 10 minutes in non-labeled SBF₂. The experiment was done in threefold.

In figure 6.8 the RBS spectra are plotted for a coating after immersion in labeled SBF₂ (full circles), and for an identical sample that was post-immersed in SBF₂ without labels (open circles). Both Sr and Se surface signals are present after immersion in

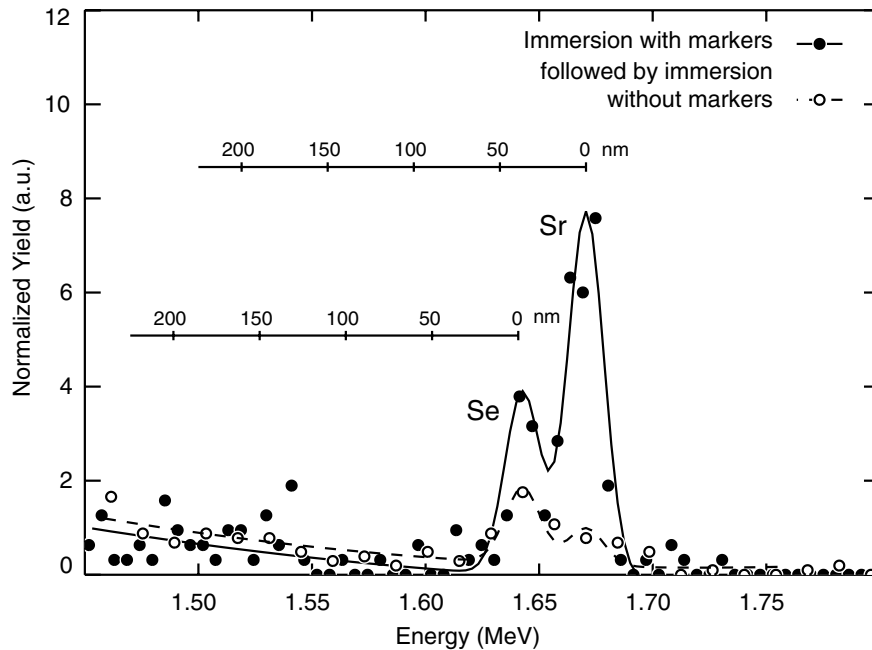


Figure 6.8: RBS spectra for CaP_{high} samples after immersion in Sr and Se labeled SBF_2 (full circles and solid line), and after subsequent immersion in non-labeled SBF_2 (open circles and broken line). For both markers depth scales in the coating are given. The background is due to signal pile-up. RBS: 2.0 MeV He^+ , $\theta=167^\circ$, $\alpha=90^\circ$.

labeled SBF_2 . For both Sr and Se, depth-scales are plotted for labels contained in the coating. We determined a Sr coverage of $2.0 \cdot 10^{14} \text{at./cm}^2$, and a Se coverage of $1.4 \cdot 10^{14} \text{at./cm}^2$. When we assume congruent sorption of the labels compared to Ca and PO_4 , total adsorption is in excellent agreement with the coverages found in table 6.2. No change in the CaP layer thickness (results not shown) and no diffusion of labels into the coating could be observed.

After re-immersion of the coatings in non-labeled SBF_2 a marked decrease in surface label concentrations was observed: the Sr coverage decreased by a factor of 7 and the Se coverage by a factor of 2. Again the coating thickness did not change. We suppose that the reduced release of the SeO_3 ions compared to the Sr ions, indicates that the SeO_3 and thus the PO_4 groups are stronger sorbed than the Sr or Ca species. Apparently, the majority of the sorption of the labels is reversible within 10 minutes. This indicates that the majority of the species found in the adsorption layer after 10 minutes immersion in SBF_2 is not contained in nuclei.

6.5 Desorption and reprecipitation

To investigate the amount of possible desorption of coating species during the induction time and the likelihood of the suggested reprecipitation mechanism, we designed the following experiments. If the only mechanism of CaP precipitation is related to the dissolution of coating species, there is a critical coating thickness necessary to allow CaP to precipitate. To investigate this hypothesis, we deposited a coating with a thickness of only 2 nm. This coating was then immersed in SBF₂ for 2 hours. In figure 6.9 the RBS spectra of the coating before (full circles) and after immersion (open circles) are plotted. Lines are simulations of the data. Clearly, CaP is precipitated on a

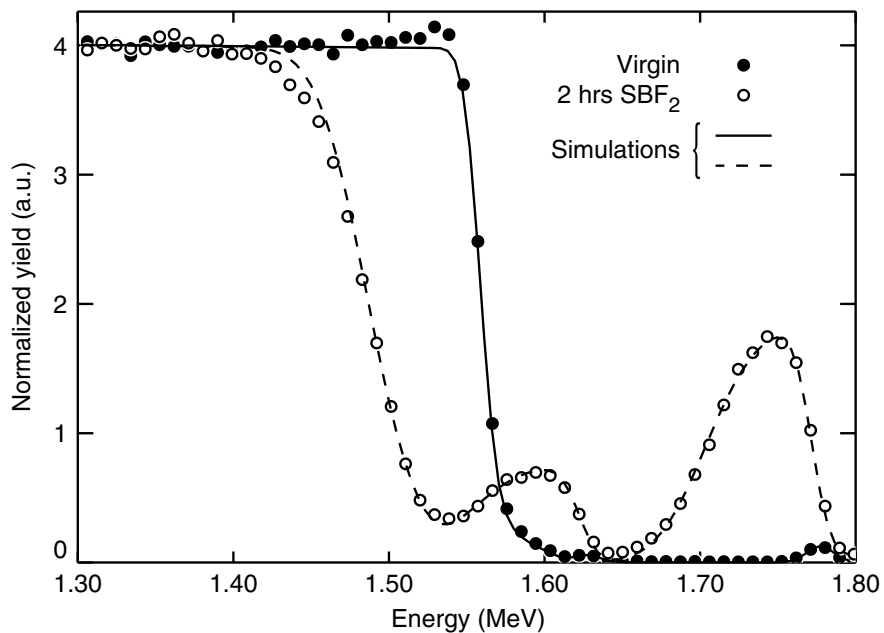


Figure 6.9: RBS spectra for a 2 nm coating before (full circles) and after (open circles) immersion for 2 hours in SBF₂. Lines are simulations of the data used to quantify the elemental coverages. RBS: 2.4 MeV He⁺, $\theta=120^\circ$, $\alpha=90^\circ$.

2 nm thick coating after immersion in SBF₂ for 2 hours. The critical coating thickness is therefore less than 2 nm, which corresponds to an upper limit of $\sim 10^{16}$ at./cm² of total desorbed Ca and PO₄ species involved in a supersaturation of the diffusive layer. Also, the RBS data of the precipitated sample allow the calculation of an accurate Ca/P ratio. The simulations provide a ratio of 1.36 with an estimated error of ± 0.05 . This is in agreement with the ratio of 1.30 ± 0.02 as found in the radiolabel experiments in section 6.4.

To refine the lower limit for desorbing species preceding the growth of CaP crystals, we can also make use of radiolabels. The aim is to introduce the labels on the coating surface and to crystallize the surface layer by a heat treatment. If any signif-

icant desorption of coating species takes place, radiolabels are released. The design of this experiment is similar to that described in section 6.3.1 and is depicted in detail in figure 6.10. Adsorption was done with CaP_{high} samples in radiolabeled SBF_2^* as

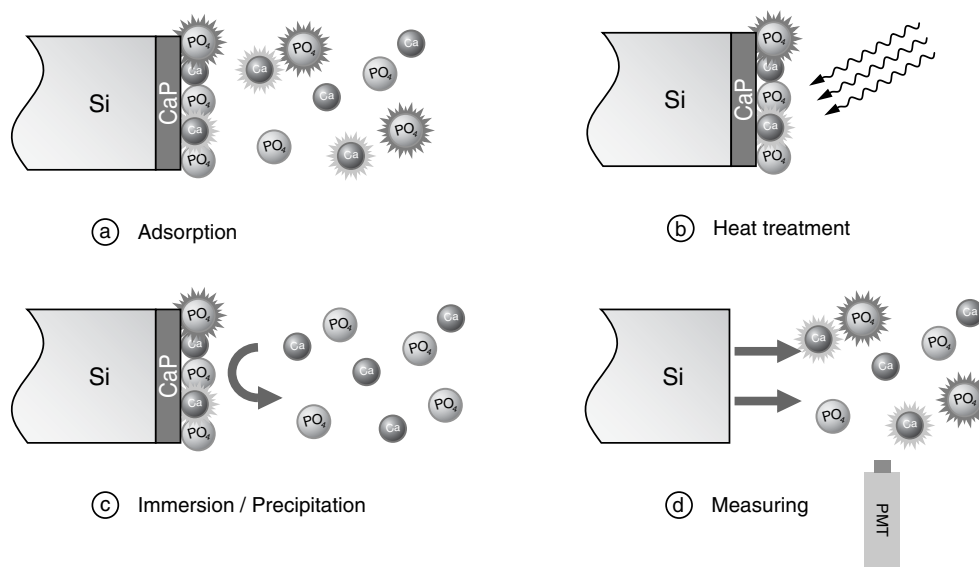


Figure 6.10: Experimental setup to test for possible desorption of coating species during the induction time preceding nucleation and growth of CaP crystals. **a)** 10 minutes adsorption of CaP_{high} samples in radiolabeled SBF_2^* . **b)** Crystallization of the surface layer by a heat treatment of 30 minutes at 650°C . **c)** Immersion for two hours in non-labeled SBF_2 . **d)** Measuring of the label activities by LSC.

described in section 6.3.3. After rinsing and drying, samples were heat-treated for 30 minutes at 650°C , to crystallize the adsorbed Ca and PO_4 on the coating CaP lattice. Then, samples were divided in halves. One part was kept as a reference, the other was reimmersed in SBF_2 without labels for two hours, allowing precipitation of CaP to occur. Then the protocol described in section 6.3.3 was followed again, i.e., coatings were dissolved and solutions were examined with LSC. Also aliquots of the residual SBF_2 used in the last step (c) were checked for the presence of radiolabels.

Before presenting the results of this experiment, a critical assumption in this design has to be verified: are the radiolabels still on top of the coating after the heat treatment (b). If the labels diffuse into the coating during the heat treatment, dissolution would not necessarily result in a considerable release of labels. Since it is not possible to measure a depth-resolved profile of the radionuclides in the coating, we added Sr or SeO_3 ions to label the SBF_2 in a separate experiment. After adsorption and heat treatment, the coatings were analyzed with RBS and X-ray photoelectron spectroscopy (XPS). In figure 6.11 the results are presented for the coatings labeled with Sr or Se before and after the heat treatment. In **a** we see RBS spectra of the Sr labeled coatings, in **b** the RBS spectra for the Se labeled coatings, and in **c** the XPS spectra for the Sr 3p peaks

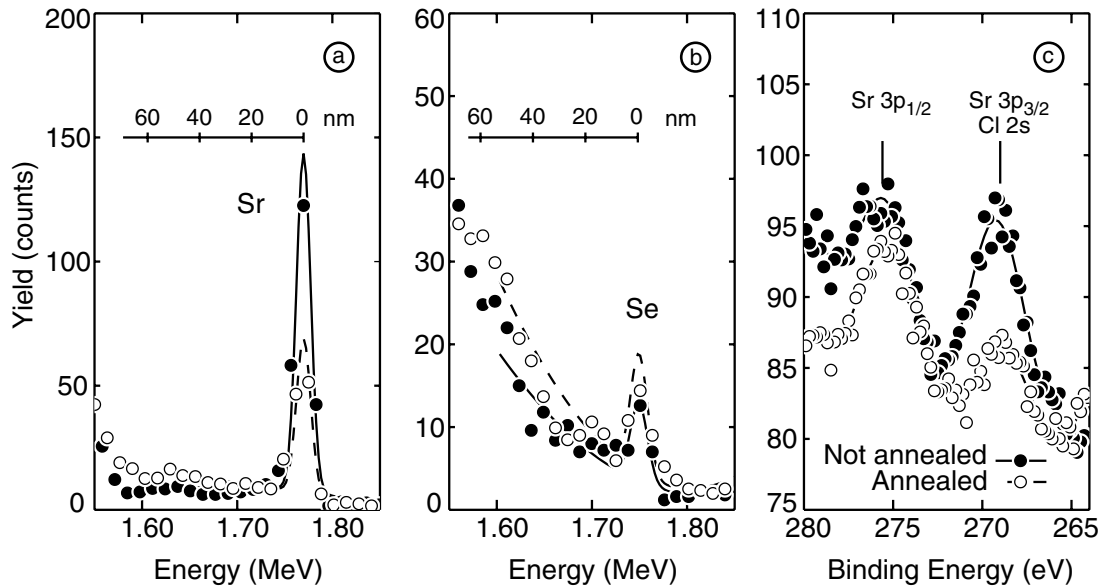


Figure 6.11: RBS and XPS spectra of CaP_{high} coatings with preadsorbed Sr or SeO_3 surface markers, before (full circles and solid lines) and after (open circles and broken lines) a heat treatment of 30 minutes at 650°C . **a)** RBS spectra of the Sr labeled coatings, **b)** RBS spectra of the Se labeled coatings, **c)** XPS spectra of the Sr labeled coatings. In the RBS graphs depth scales for the labels in the coating are given. Backgrounds in the RBS spectra are due to signal pile-up. RBS: 2.0 MeV He^+ , $\theta=110^\circ$, $\alpha=80^\circ$.

are shown. No XPS results for the Se labeled coatings are given due to overlapping signals of other elements present on the surface. The RBS profiles for both labels show that before and after annealing labels are present at the surface (or at least in a thin surface region). No significant diffusion of labels into the coating can be seen from these spectra. The XPS spectra reveal that the yields in the Sr $3p_{1/2}$ peaks before and after annealing are comparable. We have to notice that the Sr $3p_{3/2}$ peak is shadowed by the Cl $2s$ peak. Since the depth resolution of XPS is a few nanometer, we can conclude that the adsorbed labels are still present on the coating surface after a heat treatment.

Now this assumption is verified, the results of the radiolabel desorption experiment as outlined in figure 6.10 are presented in table 6.3. The differences in surface Ca and PO_4 coverages before and after immersion appear to be not significant. The Ca and PO_4 coverages are in agreement with the numbers presented in table 6.2. Some differences in Ca/P ratios were seen, but the origin is not completely clear. It is possible that some of the labels are lost during the heat treatment due to evaporation. The loss of surface labels is also in agreement with the RBS profiles in figure 6.11 **a**. However, also phosphorus could leave the surface for example as phosphine (PH_3). Preferential escape of phosphorus would also explain an increase in Ca/P ratio after the heat treat-

	Ca 10 ¹⁵ ions/cm ²	Average Ca	P 10 ¹⁵ ions/cm ²	Average P	Ca/P	Average Ca/P
before immersion	1.04		0.76		1.37	
	1.22		0.93		1.32	
	0.85		0.62		1.37	
	1.02		0.74		1.38	
	0.82	0.99±0.16	0.59	0.73±0.13	1.40	1.37±0.03
after immersion	1.14		0.84		1.37	
	1.40		1.08		1.29	
	1.06		0.80		1.32	
	0.79		0.56		1.41	
	0.99	1.08±0.22	0.70	0.80±0.19	1.42	1.36±0.05
residue	0.02		0.002			
	0.05		0.007			
	0.02		0.003			
	0.07		0.013			
	0.02	0.03±0.02	0.004	0.006±0.004		

Table 6.3: Coverages of Ca and PO₄ ions in the coating surface layer and equivalent coverages for released ions in the bulk solution (the residue), before and after immersion of CaP_{high} samples in SBF₂ for two hours. Coverages were calculated from label activities.

ment. The difference in Ca/P ratio between the adsorbate and the coating is reduced by a heat treatment.

Further, only a very small amount of radiolabels was released in the solution before precipitation takes place. We calculated a fractional release of 0.02 of the surface species. If we assume that the dissolved coating species all originate from the preadsorbed layer, we can calculate an upper limit of $\sim 4 \cdot 10^{13}$ ions desorbed over a period of about 60 minutes. Consequently, we conclude that desorption of coating species is negligible, and that reprecipitation of coating species is highly unlikely to play a role in the mechanism of CaP nucleation on these coatings.

6.6 Discussion

In this chapter we have investigated adsorption and desorption processes in close relation to the ability of CaP surfaces to nucleate CaP crystals. We have addressed the following issues. Firstly, we investigated the boundary conditions of the adsorption process. Will a difference in bulk coating composition translate into a difference in

surface composition? We also studied qualitatively which species could be identified in the adsorption layer, and compared the yields to the coating composition.

We then quantified the coverages after adsorption. An extremely powerful tool that can be used to determine very low coverages with high precision is the use of radiolabels and LSC. By labeling the solution species, we could also distinguish between Ca and PO₄ species originating from the coating and from the solution.

The reversibility of the adsorption process was evaluated to correctly interpret the adsorption result. We determined the possible effect of the formation of nuclei on the adsorption results.

In the last part, we investigated possible desorption effects preceding the nucleation of CaP crystals. Firstly, we made a crude estimation by examining the precipitation of very thin coatings. We then refined these results by using radiolabels, and studied the possibility of reprecipitation as a mechanism for CaP nucleation.

As we mentioned in the introduction, it is of utmost importance to understand the adsorptive properties of the CaP coatings. Nucleation of CaP crystals occurs in the adsorption layer and is relevant to its bioactive potential. The composition of the adsorption layer is determined by the surface composition and coordination of surface species of the coating, and their charge. It is important to note that in equilibrium these properties do not affect the chemical potential but merely the surface free energy, and thus interact with the ability to form nuclei (refer to equation 5.3 in section 5.1.1).

Extensive research has been done on adsorption on oxide surfaces [162–164], but surface thermodynamic data of ionic adsorption on CaP are limited. General modeling of the adsorption phenomena is difficult because Ca²⁺, PO₄³⁻, and OH⁻ are all potential-determining ions. A simple complexation model with only acidity constants would be an oversimplification to obtain a reliable estimation of compositions in the adsorption layer. Other difficulties arise from the high IAP, the use of NaCl as a supporting electrolyte [149], surface complexation of the electrolyte, the use of thin films instead of powders, and polydentate surface complexation, as well as competitive complexation from Mg and CO₃.

Lack of a successful general approach to model ionic adsorption on CaP quantitatively has led us to study this matter empirically.

We will now discuss our observations mentioned above in more detail.

In response to the first issue, the surface properties of the CaP coatings, we found that a difference in bulk composition translates into a difference in surface composition and that a heat treatment after deposition does not give rise to a considerable change in surface composition. These findings are essential if we aim at tailoring the surface activation properties of our coatings by varying the bulk composition. It was shown that the CaP_{high} samples allowed the formation of crystals in SBF₂ within 2 hours, whereas the CaP_{low} samples remained inert. This can be attributed to the differences we found in surface composition, but there are probably also differences in surface structure and coordination.

We have seen from the LEIS data that CaP_{high} samples show lower Ca/P ratios in the adsorption layer than the coating Ca/P ratio. For the CaP_{low} samples it works the other

way around; the Ca/P ratio in the adsorption layer is higher than the Ca/P ratio for the coating. Thus we observed that the Ca/P ratio in the adsorption layer is inversely related to the Ca/P ratio of the coating surface. We were also not able to detect any Mg in the adsorption layer. At physiological conditions, it is known that only a few at.% of Mg can be incorporated in an apatite lattice [56, 118, 165, 166]. We have seen that incorporation of Mg in the adsorption layer is also not proportional to Ca.

Further, we quantified the amount of Ca and PO₄ species in the adsorbate. The use of radiolabels is obvious. The small coverages of Ca and PO₄ found in the adsorption layer make it difficult to distinguish between coating species and sorbed species; radiolabels can be used to mark the solution. β -decay of the labels can be measured very accurately by LSC. This approach led to the conclusion that in the adsorbate on the CaP_{high} coatings a Ca/P ratio was found that is comparable to phases that have been proposed as precursor phases in CaP crystal formation [62, 167–171]. However, Ca/P ratios in this range have also been reported for Ca deficient apatites. We also found that the total amount of Ca and PO₄ species in the adsorption layer is significantly higher for the CaP_{high} coatings than the CaP_{low} coatings. Again we found that the Ca/P ratio in the adsorption layer is inversely related to the Ca/P ratio of the coating surface.

We note that since the hydration enthalpy for Ca²⁺ is much more negative than for the most abundant PO₄ species (HPO₄²⁻ and H₂PO₄⁻), PO₄ is probably specifically sorbed as an innersphere complex, whereas Ca retains its hydration shell and binds electrostatically as an outersphere complex. This certainly explains the lower Ca/P ratio in the adsorption layer (Ca/P=1.24) as compared with the bulk solution (Ca/P=2.5).

We suggest a model in which Ca surface groups provide adsorption sites for PO₄ species. For CaP_{low} samples, the lack of adsorbed PO₄ groups at the surface could also result in a higher interface potential and less electrostatically bound Ca, resulting in less adsorbed Ca and PO₄ species in the adsorption layer as observed in table 6.2.

It is plausible to assume that in the presence of a negatively charged surface, the hydrogen PO₄ species and complexes (CaH₂PO₄, CaHPO₄, H₂PO₄, HPO₄), are even more abundant in the adsorption layer, compared to the more negative PO₄³⁻ containing species. Hydration enthalpies are also lower for the less ionized PO₄ species, and thus require less energy to be incorporated in a crystal lattice. This supports the idea of the formation of phases like DCPD and OCP that incorporate HPO₄²⁻ species in their lattice. None of the CaP phases have H₂PO₄⁻ in their lattice.

We have seen that the sorption of CaP on our coatings in the time span of the adsorption experiments is most likely due to adsorption of solution species, and not due to early nucleation processes. We conclude this from the large fraction of reversibly adsorbed markers as seen from figure 6.8. We can now conclude that the markers as measured in table 6.2 are indeed from adsorbed species and not likely to be contained in early nuclei. If markers would be contained in super critical nuclei, the markers would only very slowly be exchanged from the crystals or even be buried in the growing crystal, since the desorption of labels was performed in SBF₂.

Besides the adsorptive properties of the CaP coatings, we have also addressed the desorption processes of coating species during the induction time preceding the for-

mation of CaP crystals. As mentioned in the introduction, desorption has also been related to the nucleation process by means of supersaturation of the diffusive layer. For CaP precipitation no conclusive evidence can be found in literature supporting re-precipitation of CaP as mechanism to induce nucleation. We have clearly shown that desorption of coating species is negligible from our coatings during the induction time. We have seen that at most a few times 10^{13} at./cm² are released over a period of about 40-60 minutes. Even if all coating species were to be released in 1 s, the release rate would be orders of magnitude lower than the estimated minimum release rate of $\sim 10^{16}$ ions/(cm² s) required for supersaturation of the diffusive layer (refer to section 6.2.1). We can now reject the possibility of supersaturation of the diffusive layer and re-precipitation as a mechanism of CaP formation.

It should be stressed that these findings do not imply that no simultaneous dissolution and precipitation of CaP can be observed on CaP coatings. For the thin RF-sputtered CaP coatings in these experiments we have shown that dissolution of coating species does not occur, and thus can not induce precipitation. These coatings are very homogeneous in structure. In contrast, plasma sprayed coatings for example are known to be heterogeneous, due to amorphization of the outer particle shells during spraying. These lateral structural differences can give rise to simultaneous dissolution and nucleation of CaP crystals. It is even possible that the precipitation mechanism is enhanced by the dissolution of other parts of the coating, especially when diffusion is hampered. LeGeros [16] showed convincingly that there is a relation between the solubility of calcium phosphates and their bioactive potential. However, enhancement of the precipitation process does not explain why the activation for CaP nucleation on CaP coatings is favored over most other oxide surfaces now we know that dissolution of coating species is not strictly required.

6.7 Conclusions

Concluding, we have seen that changing the bulk composition of the coatings results directly in differences in surface composition. A heat treatment of 650°C crystallizes the coating but does not influence the surface composition.

The Ca/P ratio of the adsorption layer is inversely related to the Ca/P ratio of the coating. The Ca/P ratio of the adsorbate on CaP_{high} coatings is similar to Ca/P ratios for known precursor phases, especially OCP, and indicates that PO₄ is specifically sorbed. The Ca/P ratio for CaP_{low} samples is significantly higher and total Ca and PO₄ coverages were shown to be lower than for CaP_{high} samples. In the first 10 minutes sorption on CaP coatings in SBF₂ is due to adsorption of species onto the surface and is not contained in early CaP nuclei.

During the induction time preceding CaP nucleation and growth, no considerable desorption of coating species was observed. It was shown that oversaturation due to release of coating species is not the driving force in CaP precipitation.

Application in a Cell Model

7.1 Introduction

In this chapter we focus on the behavior of RF-sputtered CaP thin films in a rat bone marrow (RBM) cell model. Two issues are addressed. Firstly, we evaluate the cytocompatibility of these CaP coatings. We examine the known bioactive potential of this material in terms of cell response to the material and structure of the bone/material interface.

In addition, the crystal formation concepts, as described in chapter 5, are verified. We further explore the relative importance of nucleation and growth of a CaP layer on top of the coating surface compared to the other processes (e.g., protein adsorption, cell signaling etc.) involved in early bone formation.

To study the cytocompatibility of CaP thin films, we compare RF-sputtered CaP coatings with coatings of other well known skeletal replacement ceramics, like titania and alumina. These ceramics have been studied extensively as bulk and coating material for their osteoconductivity and structure of their interface with bone and were qualified as *bioinert* (refer to section 1.1.1). In some studies however, titania has also been shown to induce apatite formation (e.g., gel-derived titania [111]). As was mentioned earlier, it is known that *bioinert* ceramics like alumina and titania show contact osteogenesis. Bone is formed towards the material surface to form a close contact. Sometimes fibrous tissue is formed in between the newly formed bone and the ceramic. Of all CaP ceramics some are known to be *bioactive*. These are characterized by bonding osteogenesis and the formation of a directly bonded CaP layer on its surface. Bioactive materials show osteoconductive behavior, bone formation is guided along the surface; some are even osteoinductive, they induce bone formation even

when implanted in a non-osseous tissue.

In the previous chapters we have seen that the ability of CaP coatings to form CaP nuclei on their surface even in moderately oversaturated SBFs, can play an important role in understanding their bone-bonding behavior. On the other hand, it is known that there is also a substantial influence of cell mediated processes essential for bone formation. Some proteins that play a key role in early bone formation have a high affinity for CaP. These proteins can affect the mineralization process by promotion or inhibition of nucleation, or direct cell behavior as a signaling agent. Also conformational aspects of these proteins on CaP surfaces contribute to their functionality. It is also known that cell function can regulate local pH, calcium and phosphate levels by membrane pumps and hydrolysis of phosphate esters. In the experiments we try to distinguish between the cell mediated processes and nucleation/growth processes in the early formation of the material bone interface.

For both objectives we make use of osteogenic markers to study cellular response to the different surfaces. Cell proliferation is measured by the DNA content of the culture, differentiation by the activity of alkaline phosphatase (ALP) and production of osteocalcin. Mineralization is quantified by the total Ca content. The structure of the early coating bone interface is studied by SEM.

RF magnetron sputtering allows us to produce thin films of alumina, titania, and CaP with very similar coating thickness and morphology. By using relatively thin coatings (as compared to most other cell culture studies) with hardly any micro-roughness we are able to focus exclusively on the role of the surface chemistry on cell behavior and interfacial structure.

Before describing the experiments, we give a short outline of the osteogenic lineage and the quantitation of its markers. Then we proceed with the experimental design of the studies, followed by the results and discussion. This is done in two parts. Firstly, the biocompatibility of the coatings is investigated, thereafter we focus on the role of nucleation of CaP on the coating surface and the formation of a directly bonded calcified layer.

7.1.1 Introduction to osteogenesis

We present a short and somewhat simplified overview of the osteogenic lineage. For a review on osteoblastic differentiation we refer to Bianco et al. and Aubin [172, 173] and figure 7.1. Bone marrow stroma consists of a collection of progenitors of each mesenchymal cell type, like adipocytes, chondrocytes, myoblasts, fibroblasts, and osteoblasts. All these cell types are believed to originate from one type of multipotential stem cell, the bone mesenchymal stem cell (BMSC). The BMSC still has the ability of self renewal and to develop along different lineages into different cell types. BMSCs are the source for osteoprogenitor cells, a cell type with only limited self renewal and able to generate pre-osteoblasts. Two types of osteoprogenitor cells exist: one differentiates under normal culture conditions (ascorbic acid, β -glycerophosphate, fetal calf serum), the other needs certain stimulating factors like dexamethasone and bone

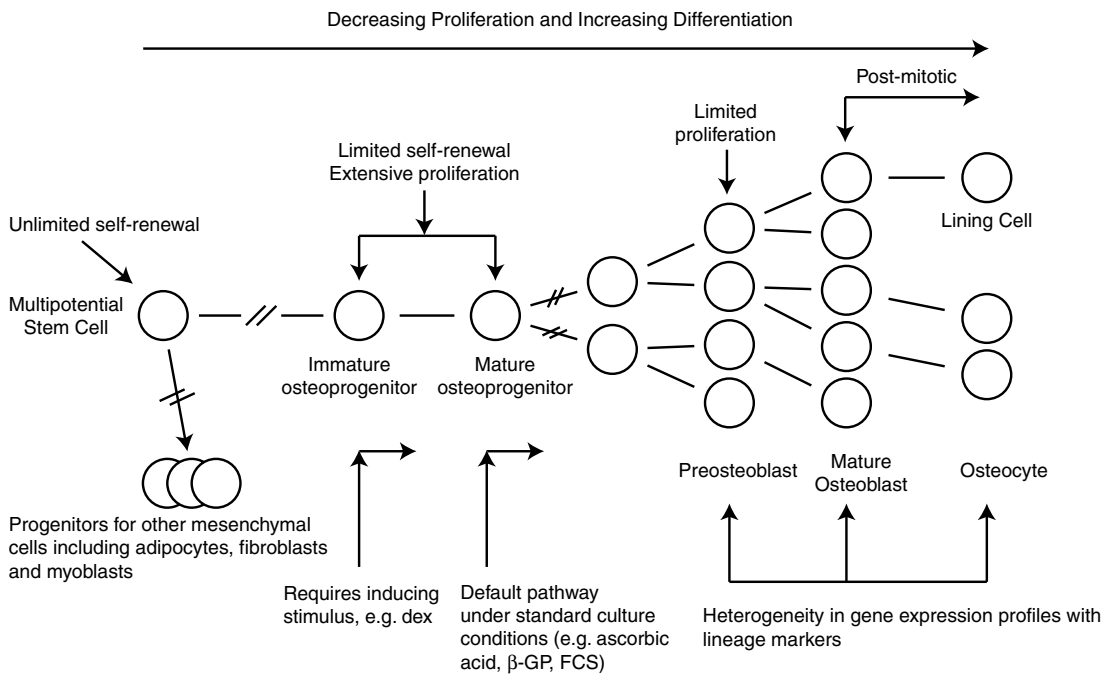


Figure 7.1: The osteogenic lineage, after Aubin [172], with permission.

Cell type	Collagen type I	Alkaline phosphatase	Osteocalcin	Bone sialoprotein	Osteopontin
BMSC	?	?	-	-	?
Osteoprogenitor (Immature)	-	-	-	-	±
Osteoprogenitor (Mature)	++	+	-	-	∓
Preosteoblast	++	++	-	-/+++	-/+
Osteoblast (Mature)	++	+++	-/+++	-/+++	-/+++
Osteocyte	-	-	-	-/+++	-/+++

Table 7.1: Marker expression for the different stages in the osteogenic lineage. {-, ∓, ±, +, ++, +++} marker expression levels from not detectable to very high, -/+++ indicates a broad heterogeneous spectrum of expression levels for individual cells. Aubin [172], with permission.

morphogenetic proteins. Preosteoblasts already stain for alkaline phosphatase, and can develop into mature osteoblasts which produce the extracellular matrix. Cell cultures have shown a limited viability *in vitro*. The different stages in the differentiation process towards mature osteoblasts are characterized by different expression of osteogenic markers. Some of the most important ones are listed in table 7.1 with their expression levels for the different stages in the lineage.

7.2 Materials and Methods

7.2.1 Cell culture

In the cell studies a rat bone marrow (RBM) cell model was used to evaluate the materials biocompatibility. *In vitro*, stromal cells from rat, mouse, and human bone marrow have been shown to give rise to mineralizing osteoblastic cultures. The RBM cell model has been well described. Rat bone marrow cells were isolated and cultured according to Maniopoulos [174]. Bone marrow cells were obtained from femora of male Wistar rats. Femora were washed in α Minimal Essential Medium (α -MEM) with 0.5 mg ml^{-1} gentamycin and $3 \text{ } \mu\text{g ml}^{-1}$ fungizone (Gibco). Then, epiphyses were cut off and the diaphyses flushed out with 15 ml α -MEM supplemented with 15% fetal calf serum (FCS), $50 \text{ } \mu\text{g ml}^{-1}$ ascorbic acid, $50 \text{ } \mu\text{g ml}^{-1}$ gentamycin, 10 mM Na β -glycerophosphate, and 10^{-8} M dexamethasone. This cocktail is addressed as *medium*. Cultures were incubated in a humidified air atmosphere at 37°C and 5% CO_2 . After 7 days of primary culture cells were detached by trypsin/ethylenediaminetetraacetic acid (EDTA), resuspended in medium to $2.0 \cdot 10^4$ cells ml^{-1} , and used in the experiments.

Substrates were seeded with 1 ml ($2.0 \cdot 10^4$ cells) of cell suspension at day 0 and cultured in 24-wells plates for the different time periods, again in a humidified air atmosphere at 37°C and 5% CO_2 . Medium was changed three times per week. Control substrates without cells were treated in the exact same way, using medium without suspended bone marrow cells.

7.2.2 Cell proliferation

Cell proliferation was quantified by means of its total DNA content, using a PicoGreen ds-DNA quantitation kit (Molecular Probes Inc, Eugene OR, USA). This method was reviewed by Singer [175]. For the DNA assay, the medium was removed and the cell layers were washed twice with phosphate buffered saline (PBS). Substrates were put in a 10 ml tube containing 1 ml milliQ water and stored at -20°C . For analysis, the 10 ml tubes were incubated at 37°C for one hour. After that the tubes were placed at -70°C for 2 hrs. After thawing, samples were sonicated for 10 min. After that samples were analyzed. PicoGreen reagent in dimethylsulfoxide (DMSO) was diluted 1:200 in 10 mM tris-HCl, 1 mM EDTA at pH 7.5. $100 \text{ } \mu\text{l}$ reagent was added to $100 \text{ } \mu\text{l}$ sample and incubated for 5 minutes in the dark to avoid photodegradation of the dye. Flu-

orescence was measured in a fluorescence plate reader (Bio-Tek) using an excitation filter of 365 nm and an emission filter of 450 nm. Results were compared to a standard curve of serial dilutions of bacteriophage lambda ds-DNA.

7.2.3 Cell differentiation

Alkaline phosphatase activity

Alkaline phosphatase (ALP) is an enzyme, which catalyzes the splitting of phosphate from mono-phosphoric esters and has maximum enzyme activity at pH 10.5. It is widely used as a marker of the osteoblastic phenotype. Quantitation is done using paranitrophenyl phosphate, which is hydrolyzed at pH 10.5 and 37°C by ALP to form the yellow paranitrophenol [176]. Medium was removed and samples were washed twice with PBS. Substrates were put in 10 ml tubes containing 1 ml milliQ water and stored at -20°C. For analysis, samples were warmed to room temperature and cell suspensions were sonicated and centrifuged at 2000 rpm. Buffer solution was made with 5 mM MgCl₂.6H₂O and 0.5 M 2-amino-2-methyl-1-propanol. 100 μl of 5 mM paranitrophenyl phosphate was added to 20 μl sample and 80 μl of buffer solution. Plates were incubated for 1 hour at 37°C. The hydrolysis reaction was stopped by addition of 100 μl 0.3 M NaOH. Plates were read in an ELISA plate reader at 405 nm. ALP analysis was performed on the same samples as used in the DNA determination.

Osteocalcin production

Osteocalcin is a protein specifically produced by mature osteoblasts [177] and has a high affinity for calcium phosphate and hydroxyapatite [178]. The majority of osteocalcin secreted by osteoblasts is deposited in the ECM. Osteocalcin was measured with an ELISA (enzyme-linked immunosorbent assay) kit (Biomedical Technologies Inc.), which was reviewed by Lee [179]. Cell layers were washed three times in PBS and collected by scraping in 1 ml of sample buffer, sonicated for 10 minutes and stored at -20°C. For analysis, 100 μl of sample was added to osteocalcin antibody coated polystyrene wells and incubated at 4°C for 18 hours. Plates were washed three times in PBS and 100 μl of donkey anti-goat IgG peroxidase was added and incubated for 1 hour at room temperature. Plates were then washed in PBS, 100 μl of substrate solution was added, and plates were incubated for 30 minutes. 100 μl stop solution was added and the plate was read at 450 nm in an ELISA plate reader. Results were compared to serial dilutions of an osteocalcin standard.

7.2.4 Mineralization

Mineralization was measured by the Ca content of the samples. Ion beam analysis (IBA) techniques could not be used after ~4 days of cell culture due to its limited probing depth. Ortho-cresolphthalein complexone (OCPC), a complexing indicator, was

used to quantify the Ca content [180] after 4 days. In alkaline solutions, the presence of Ca ions influences the deprotonation level of the OCPC molecules, indicated by a dramatic change in optical absorption, to show a deep purple color. 8-hydroxyquinoline can be added to eliminate the interference by Mg. Samples were washed three times in PBS, 1 ml 0.5 M acetic acid was added, and were incubated and put on a shaker for 24 hours. An OCPC solution was made by dissolving 80 mg OCPC to 75 ml milliQ water and adding 0.5 ml 0.5 M acetic acid and 0.5 ml 1 M KOH. Sample solution was obtained by mixing 5 ml OCPC solution with 5 ml 14.8 M ethanolamine/boric acid buffer (pH 11), 2 ml 8-hydroxyquinoline (5 g in 100 ml 95% ethanol), and 88 ml milliQ. 10 μ l sample was added to 300 μ l of sample solution. Plates were incubated at room temperature for 10 minutes and read in an ELISA plate reader at 570 nm. Results were compared to serial dilutions of a 1 mg ml⁻¹ CaCl₂·2H₂O standard.

7.2.5 Scanning electron microscopy

Samples were washed three times in PBS and fixated in 2% glutaraldehyde. Samples were then washed twice with 0.1 M Na-cacodylate buffer at pH 7.4, and subsequently dehydrated in a graded series of ethanol and dried in tetramethylsilane. Samples were sputter coated with carbon and examined with a Jeol 6310 scanning electron microscope. Images were acquired by detecting the emission of secondary electrons. An acceleration voltage of 15 kV was applied. Cross-sectional views of the interfaces were obtained by cracking the substrates and tilting the samples to an angle of 70°.

7.2.6 Coating application

Coatings were deposited on silicon (100) substrates with RF magnetron sputtering in 5.0·10⁻³ mbar Ar using one target and a rotating substrate holder. CaP coatings were sputtered for 30 minutes at 600 W from a target of granulated HAP. Here, an intermediate TiO₂ layer (30 s at 200 W) of ~10 nm was applied as a bonding layer to prevent delamination during immersion. Thick CaP coatings were obtained under the same conditions by sputtering for 5 hours. Alumina coatings were produced by sputtering for 30 minutes at 600 W from Al₂O₃ granules and titania coatings were obtained from a Ti target by sputtering for 5 minutes at 200 W. RBS measurements showed that all coatings had a thickness between 60 and 80 nm. CaP and TiO₂ coatings were post-annealed for 30 minutes at 650°C. Oxygen over metal ratios of Al₂O₃ and TiO₂ were shown to be stoichiometric within 10 at.% from RBS.

7.2.7 Statistical treatment

All cell culture data were graphed as mean \pm standard deviation. Outliers were removed using a Dixon's Q test with a confidence level of 90%. Normality was checked with a Kolmogorov and Smirnov test. Results were compared using an unpaired t-test,

or one-way ANOVA with a Tukey post-hoc test when comparing more than two sample groups. A p-value smaller than 0.05 was considered to be significant. Equality of the standard deviations was checked using Bartlett's method. When differences in standard deviations were found to be significant, t-tests were applied with a Welch correction, and ANOVA was performed non-parametrically (Kruskal-Wallis with a Dunn's post-hoc test). All tests were performed using GraphPad InStat (version 3.05 for Win 95/NT, GraphPad Software, San Diego California USA, www.graphpad.com, Copyright 1992-2000 GraphPad Software Inc.).

7.3 Part I: Biocompatibility

7.3.1 Setup of the study

In this first part, we address the biocompatibility of CaP thin films *in vitro*, and compare it to similar coatings of Al_2O_3 and TiO_2 , which are known to be bioinert. We evaluate cell behavior and structure of the bone material interface. The outline of the experiment is depicted schematically in figure 7.2.

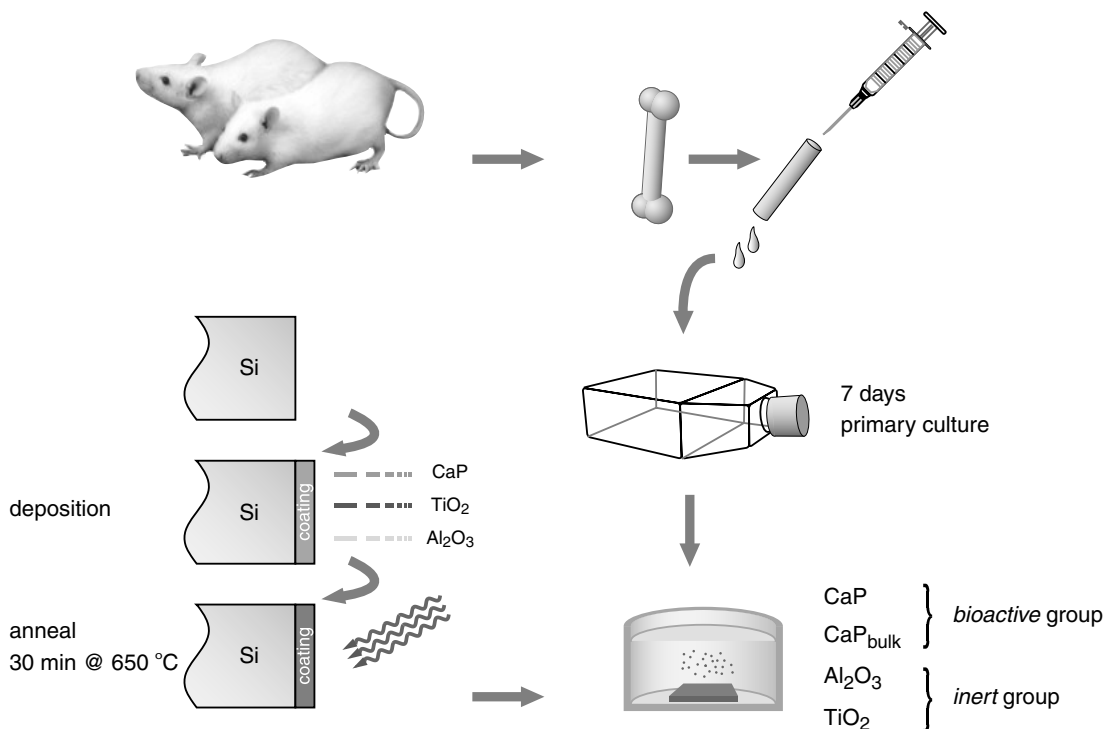


Figure 7.2: General setup of the cell experiments and the definitions of the sample groups in the biocompatibility experiment.

Coatings were produced as described in section 7.2.6 and the cell culture was conducted according to section 7.2.1. In table 7.2 the experimental design for this study is outlined. In this table, for each marker/technique and each culture period, the number of samples is given that were subjected to the analysis. In total, 4 different sample

Technique	Culture period					
	day 0	day 4	day 8	day 12	day 16	day 24
DNA	- / -	4 / -	4 / -	4 / -	4 / -	- / -
ALP	- / -	4 / -	4 / -	4 / -	4 / -	- / -
Osteocalcin	- / -	- / -	4 / -	4 / -	4 / -	- / -
OCPC	- / -	4 / -	4 / -	4 / 4	4 / -	4 / 4
SEM	- / -	- / -	3 / 3	- / -	3 / 3	- / -

Table 7.2: Experimental design for the biocompatibility experiment. Sample groups are: CaP, CaP_{bulk}, Al₂O₃, and TiO₂. For each technique and culture period the number of analyzed samples per sample group is given as · / ·; the first number is the number of samples in the cell culture, the second the number of samples in the control experiment without cells.

groups were used, i.e., thin CaP coatings (60-80 nm), thick CaP coatings ($\sim 2 \mu\text{m}$), Al₂O₃, and TiO₂. We refer to these groups as CaP, CaP_{bulk}, Al₂O₃, and TiO₂ respectively. The combination of the CaP sample groups (CaP and CaP_{bulk}) is also defined as the 'bioactive' group, and the combined Al₂O₃ and TiO₂ groups as the 'bioinert' group. The CaP_{bulk} sample group was added to investigate possible influences of coating thickness and substrate material. Along with the cell culture, a control experiment was conducted without RBM cells. The numbers of used control samples are also mentioned in table 7.2.

7.3.2 Results of the biocompatibility study

In figure 7.3 we present the results for the DNA content, the ALP activity and the osteocalcin production. The marker levels are plotted versus culture time for each of the

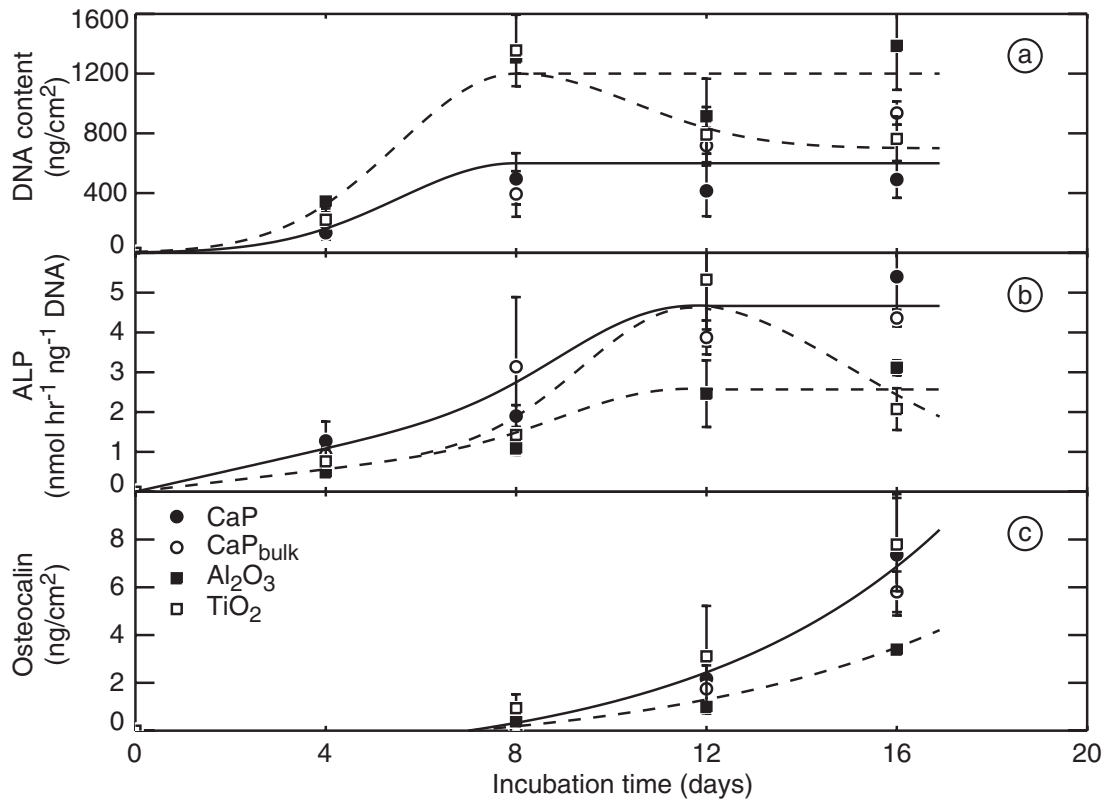


Figure 7.3: Osteogenic marker levels versus culture period for the different sample groups. All lines are to guide the eye. From top to bottom: **a)** DNA content. The solid line follows the 'bioactive' groups (CaP and CaP_{bulk}), broken lines are for the 'bioinert' groups (Al₂O₃ and TiO₂). **b)** ALP activity. Solid line for the 'bioactive' groups, broken lines for the 'bioinert' groups. **c)** Osteocalcin production. Solid line for the 'bioactive' groups and TiO₂, broken line for Al₂O₃.

four different sample groups. The solid lines are associated with the 'bioactive' sample groups (CaP and CaP_{bulk}), the broken lines with the 'bioinert' groups (Al₂O₃ and TiO₂).

In **a** the total DNA content is plotted as a marker for the proliferation of the cell population. For the CaP sample groups the proliferation behavior is quite similar. At day 8 we observe that the DNA content of the 'bioinert' groups (Al₂O₃ and TiO₂) is significantly higher than the 'bioactive' groups. After day 8 the upper broken line follows the Al₂O₃ data and the lower one the TiO₂ data. After 16 days of cell culture, the DNA content in the Al₂O₃ group is still significantly higher than for the 'bioactive'

group. The decrease in the DNA content after day 8 of the TiO₂ sample group is often observed in *in vitro* cell cultures. This could well be attributed to the limited viability of these cell cultures. However, also the detachment of cell layers after prolonged culture periods can account for this decrease. Consequently, we see that early proliferation is higher on the 'bioinert' sample groups as compared to the 'bioactive' sample groups.

In **b** the ALP activity per total DNA content is given as an early osteoblast phenotype marker. At day 4, 8, and 16 the ALP activities for the 'bioactive' sample groups together are significantly higher when compared to the combination of the 'bioinert' sample groups. At day 12, ALP levels of the 'bioactive' group is higher than the Al₂O₃ group.

Further, only for the TiO₂ specimens we noticed a decrease of ALP expression after 16 days of culture.

Figure 7.3 **c** shows the osteocalcin production, a marker for mature osteoblasts. From day 8 on, osteocalcin levels keep increasing for all sample groups. At day 16 levels for the CaP groups and for TiO₂ are significantly higher than for Al₂O₃. It is known that late markers for osteoblastic differentiation like osteocalcin and osteopontin show a maximum yield after the ALP activity starts decreasing. Owen et al. [181] found maximum ALP activity after 16 days and maximum osteocalcin levels at day 20. Similar results were found by Ter Brugge et al. [93]. This would suggest that osteocalcin levels would still rise after 16 days. An explanation for the simultaneous observation of high ALP activity and increasing osteocalcin levels could be the heterogeneity of the cell cultures.

In summary, we observed a decrease of early proliferation and an increase of early differentiation on the CaP sample groups compared to Al₂O₃. TiO₂ shows intermediate behavior with lower ALP activity at day 8 and 16 compared to the 'bioactive' group, but similar osteocalcin levels at all culture periods.

No significant difference could be found between the CaP and CaP_{bulk} sample groups for any of the markers at any culture period.

In figure 7.4 the increase in Ca content as measured with OCPC is plotted for each sample group at the different culture periods. For the 'bioactive' sample groups, Ca contributions due to the coatings were subtracted. We observed that until day 12 no increase in Ca occurs for all sample groups. Control groups did not show any significant increase in Ca content at any of the culture periods, and were omitted for clarity. From day 12 on, CaP accumulated in the cell cultures for all sample groups. The solid line follows both the 'bioactive' and the TiO₂ sample groups, the broken line corresponds to the Al₂O₃ data. We see that at day 24 CaP formation on Al₂O₃ is about 40% less than on the TiO₂ or the CaP sample groups. Since the DNA content of the Al₂O₃ sample group is higher as compared to the other sample groups (figure 7.3 **a**), differences are even more pronounced if Ca increase per cell would be plotted. Further, we notice that the start of CaP formation coincides with the start of osteocalcin production (figure 7.3 **c**), indicating the presence of mature osteoblasts and the formation of extracellular matrix (ECM).

SEM observations revealed that all coatings were still intact at day 8 and day 16 in

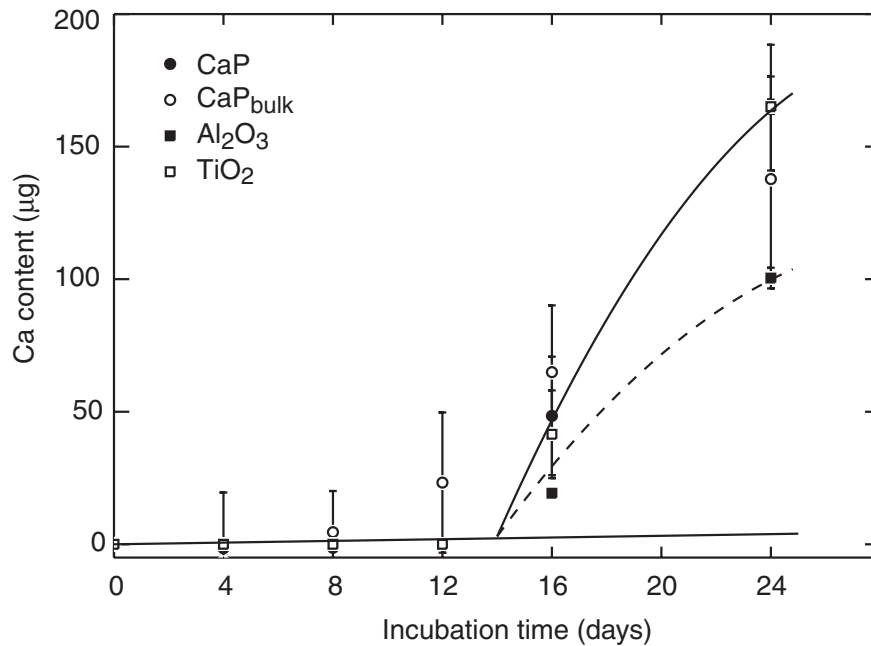


Figure 7.4: Increase in Ca content versus culture period for the different sample groups. All lines are to guide the eye. The solid line follows the CaP groups (CaP and CaP_{bulk}) and the TiO₂ sample group, broken lines are for the Al₂O₃ sample group. Ca increase of the CaP groups was corrected for the coating contribution. At day 24, CaP and TiO₂ data points overlap.

the control experiments without cells (not shown). No signs of coating deterioration, like the formation of dissolution pits, was observed. At day 8 no sign of calcification was found on any of the sample groups, neither directly bonded to the sample surface nor elsewhere, confirming the mineralization data of figure 7.4. No production of ECM could be observed at this point. Cells were completely spread by this time. Cell layers were not confluent yet. Only small differences could be observed between different sample groups.

Figure 7.5 shows the electron micrographs of the sample groups after 16 days of cell culture. Note the different magnification in **c**.

Abundant matrix production could be observed in the CaP sample groups (**a** and **b**), and in the TiO₂ sample group (**d**). Also bundles of collagen and globular CaP accretions can be seen (white spots). The presence of CaP was also verified by energy dispersive X-ray spectrometry (EDX). In the Al₂O₃ sample group (**c**), only limited collagen formation can be observed and no accretions of CaP are found. Lots of retracted cells can be seen, mutually connected by micropodia. These were also found, to a much lesser degree, on the TiO₂ coatings.

To obtain a better view of the interfacial structure of the samples, substrates were scratched on the backside and broken in half to get a freshly cleaved interface. In

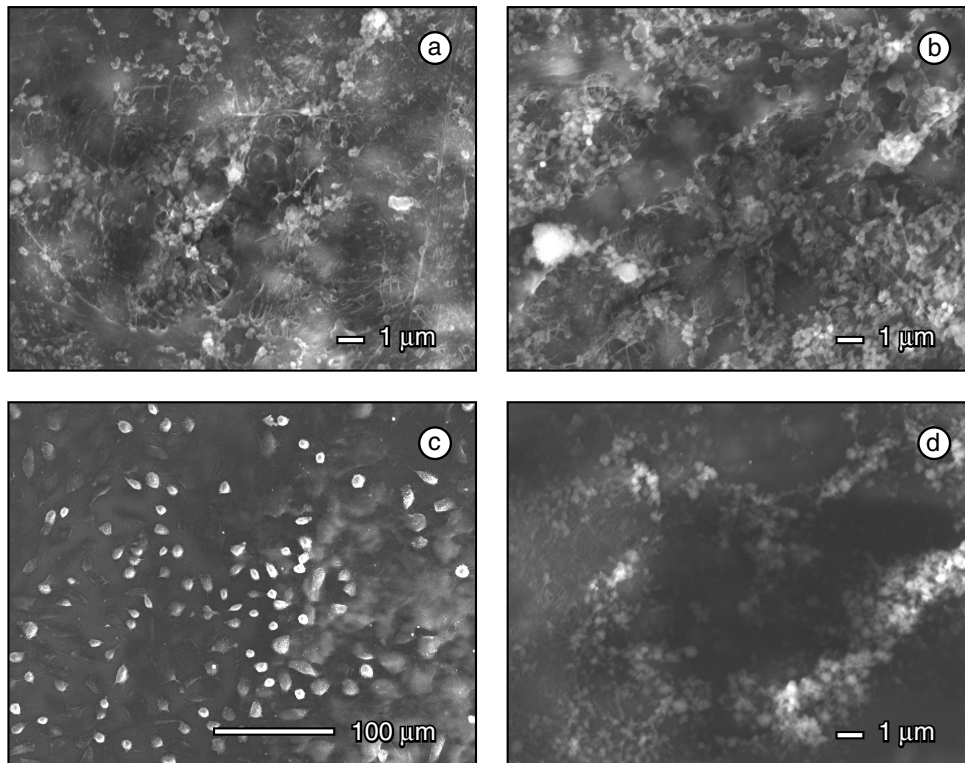


Figure 7.5: Top view electron micrographs of each sample group at day 16. **a)** CaP, **b)** CaP_{bulk}, **c)** Al₂O₃, and **d)** TiO₂. Magnification **a**, **b**, **d**: 5k, magnification **c**: 250.

figure 7.6 the same samples are shown as in figure 7.5, now tilted over 70°. In the figures the location of the coating is indicated by a broken line. Coating positions were checked with EDX. Spatial resolution of EDX is a few hundred nm. In figures **a** (CaP), **b** (CaP_{bulk}), and **d** (TiO₂) the presence of a CaP layer directly bonded to the coating is demonstrated. In figure **a** the different layers that build the interface of a bioactive material can easily be distinguished. First we have the original coating (~60 nm) on the lower side of the bright layer indicated by the broken line. Then there is a dense, directly bonded afibrillar CaP rich layer of ~800 nm covered with collagen fibers. On top, there is a confluent cell blanket. These layers can also be identified in figures **b** and **d**. The inset in figure 7.6 **d** shows the same TiO₂ sample as in **d** at a smaller magnification, indicating that in some places the cell blanket was detached from the interface layers. The same effect can be observed for the CaP_{bulk} sample in **b**, and is most likely caused by tearing off of the layers during the cracking of the substrates. Note that in these pictures, cell blankets consist of calcified cell multi-layers, and appear thicker than the corresponding layer for the CaP sample in **a**.

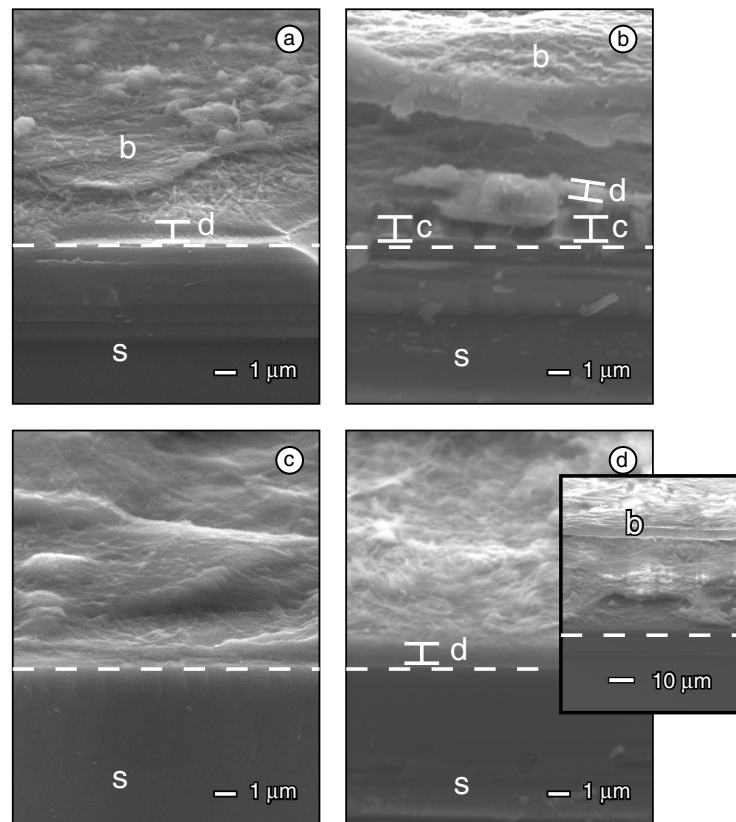


Figure 7.6: Side view electron micrographs of each sample group at day 16. **a)** CaP, **b)** CaP_{bulk}, **c)** Al₂O₃, and **d)** TiO₂. The inset shows the same TiO₂ sample at a 1k magnification. Broken lines indicate the position of the original coating. Bars in figure a,b, and d indicate the position of a directly bonded CaP rich layer as confirmed with EDX. Magnification: 5k. Annotations: s: substrate, b: cell blanket, c: original coating layer, d: directly bonded CaP layer.

However, the total calcium content in figure 7.4 gives much more accurate information since it is integrated over the entire sample surface and was performed in fourfold.

In contrast to the 'bioactive' groups and TiO₂, the layer directly adjacent to the Al₂O₃ coating contained little CaP as confirmed by EDX.

Two types of CaP sources can be identified. Firstly, we observed the globular accretions associated with the collagen network as presented in figure 7.5. Further, from side-view electron micrographs at day 16, a directly attached layer of CaP can be identified on the coating surface of the 'bioactive' sample groups and TiO₂. This layer is created between day 8 and day 16.

Thus, looking at the DNA, ALP, and osteocalcin levels we see that early prolifera-

tion is reduced, and early differentiation is enhanced in the CaP sample groups compared to Al_2O_3 . TiO_2 shows intermediate behavior with lower ALP activity at day 8 and 16 compared to the 'bioactive' group, but similar osteocalcin levels at all culture periods.

Summarizing, we can conclude the following from the results in this first part. We see reduced early proliferation, enhanced early differentiation, enhanced mature osteoblast activity, and abundant matrix formation in the bioactive CaP groups as compared to the bioinert Al_2O_3 . In contrast to the Al_2O_3 , the bioactive CaP groups show the formation of a directly bonded CaP rich layer. This layer is formed together with the calcification of the ECM in the presence of mature osteoblasts. TiO_2 shows intermediate behavior: early proliferation follows the bioinert Al_2O_3 , mature osteoblast activity, matrix production, and interfacial structure follow the bioactive CaP groups. Substrate or thin film effects could not be observed.

7.4 Part II: Effect of prenucleation

7.4.1 Setup of the study

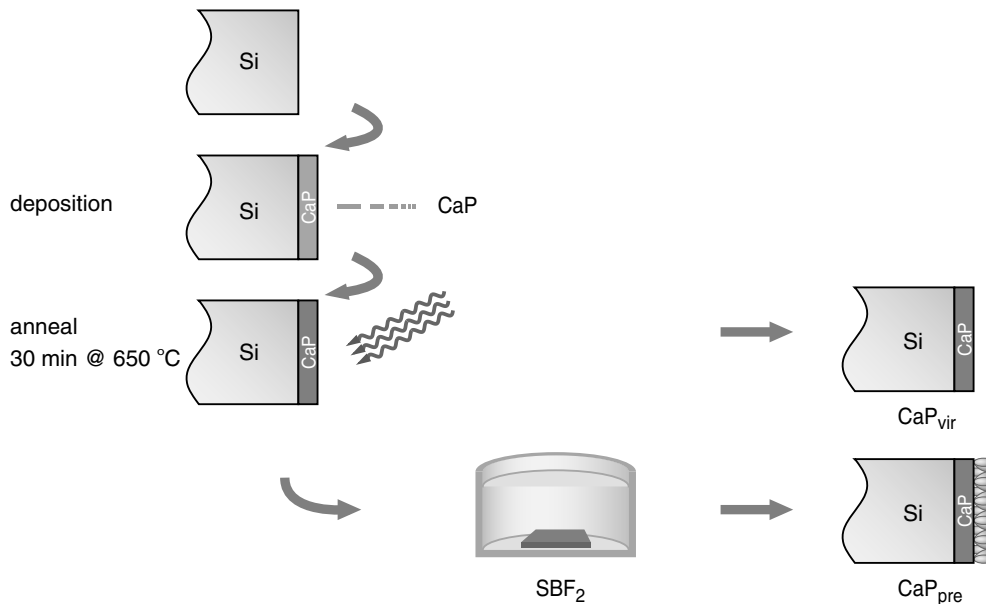


Figure 7.7: Setup of the second cell experiments (layer thicknesses not to scale).

In the second part of this chapter we examine the role of nucleation of CaP crystals on the CaP coating surface in the formation of the material bone interface. To study this we monitor the difference in cell behavior and interface structure between two sample groups: untreated RF-sputtered CaP coatings of $\sim 60\text{-}80$ nm, and samples which were pretreated for 2 hours in SBF₂. As we observed earlier, these conditions are sufficient to overcome the barrier for nucleation of CaP and the formation of crystals. Coatings were produced as described in section 7.2.6 and presented in figure 7.7. The cells were cultured according to the method described in section 7.2.1 and figure 7.2. In table 7.3 the experimental design for this study is given. Here, the number of samples that were subjected to the analysis is given for each marker/technique and each culture period.

The sample group that was not subjected to a pretreatment is addressed as reference or *virgin* (CaP_{vir}), the *pretreated* group as CaP_{pre} . Again, control experiments were performed under identical circumstances without cells. These numbers are also listed in table 7.3.

For the first two culture periods in this study, IBA was used to determine CaP apposition instead of OCPC. This was done to enhance the sensitivity of measuring small differences in CaP content for short immersion times.

Technique	Culture period					
	day 0	day 4	day 8	day 12	day 16	day 24
DNA	6 / -	6 / -	6 / -	6 / -	6 / -	- / -
ALP	6 / -	6 / -	6 / -	6 / -	6 / -	- / -
Osteocalcin	- / -	- / -	6 / -	6 / -	6 / -	- / -
OCPC	- / -	- / -	6 / 6	6 / 6	6 / 6	6 / 6
IBA	6 / 6	6 / 6	- / -	- / -	- / -	- / -
SEM	- / -	- / -	3 / 3	- / -	3 / 3	- / -

Table 7.3: Experimental design for the prenucleation experiment. Sample groups are: CaP_{vir}, CaP_{pre}. For each technique and culture period the number of analyzed samples per sample group is given as · / ·; the first number is the number of samples in the cell culture, the second the number of samples in the control experiment without cells.

7.4.2 Results of the prenucleation study

In figure 7.8 the results for the DNA content (**a**), ALP activity (**b**), and the osteocalcin production (**c**) are plotted. No significant differences in DNA content could be observed at any culture period. Up to day 12, levels for the CaP_{vir} group are very much comparable with the levels from the previous study (figure 7.3 **a**). Clear differences can be seen after day 12, where the DNA content drops to very low numbers. We attribute this phenomenon to the limited viability of the cell cultures or the detachment of cell layers. In contrast, for the 'bioactive' groups in the previous study, no decrease in DNA content was observed at any period.

Maximum ALP activity in this study was obtained between day 4 and 8, which is considerably earlier than in the biocompatibility study, where maximum activity was obtained after day 12. Constant ALP levels were observed then, whereas in this study ALP levels decreased. Differences between the CaP_{vir} and CaP_{pre} groups are not significant at any period.

For the osteocalcin production at day 8 and 12, comparable levels were found as in the previous study (figure 7.3 **c**). The production of osteocalcin appears to be influenced by the decrease in cell numbers as seen from the DNA. This may explain very well the stagnation in the production at day 16. The fact that osteocalcin levels do not vanish together with the DNA content can be explained from a high osteocalcin production per cell, and the affinity of osteocalcin for CaP [178]. This can also be inferred from the Ca content in the cell cultures after about day 8 (see figure 7.10). No significant differences in osteocalcin levels between the two sample groups were observed at any culture period.

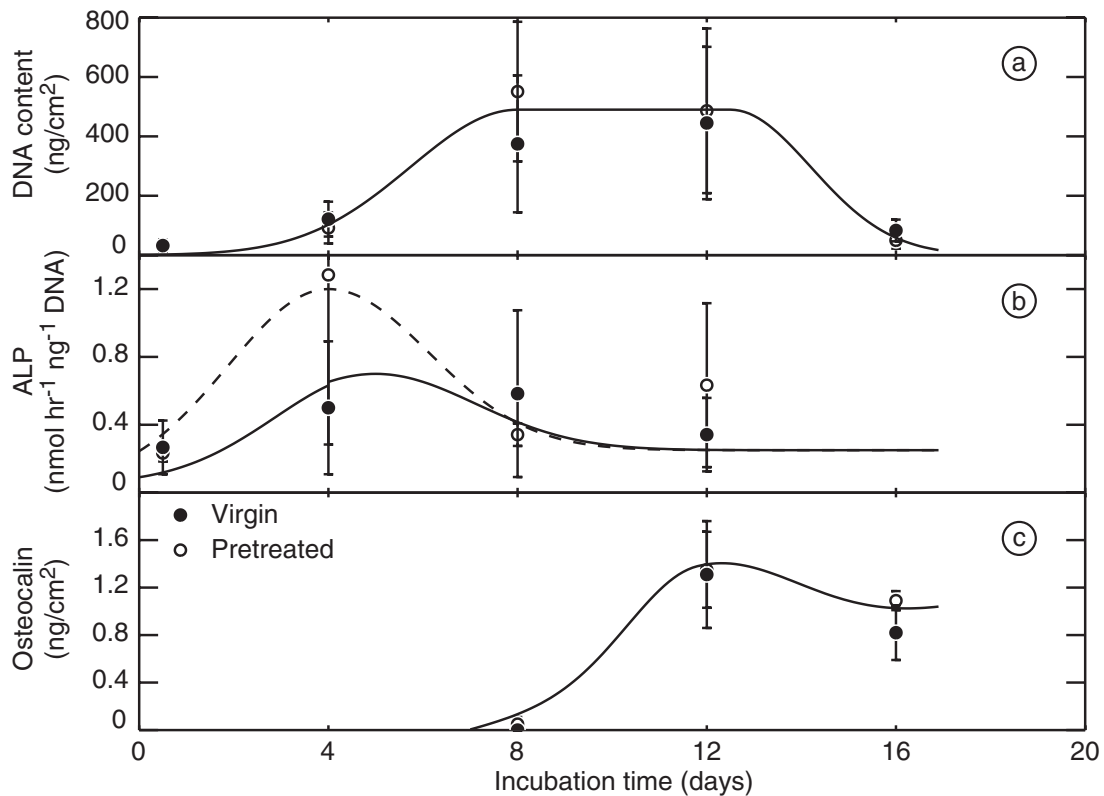


Figure 7.8: Osteogenic marker levels versus culture period for the untreated sample group (CaP_{vir}) and the pretreated group (CaP_{pre}). All lines are to guide the eye. From top to bottom: **a)** DNA content. **b)** ALP activity. The solid line follows the CaP_{vir} group, the broken line corresponds with the CaP_{pre} group. **c)** Osteocalcin production.

For the first two culture periods in this study, IBA was used to determine CaP apposition instead of OCPC, to enhance the sensitivity at short immersion times. Figure 7.9 shows ERD depth profiles for Ca, P, and O of the CaP_{pre} sample group after 4 days of culture. Open circles and broken lines correspond to the a CaP_{pre} sample that was provided with RBM cells for 4 days. Full circles and lines are for a corresponding as-prepared CaP_{pre} reference that was not used in the culture experiment. The apparent increase in P yield is due to the Si substrate signal that can not be separated from the P. Note the different probing depths for the different elements. We see that already after 4 days of cell culture the amount of CaP on top of the coating has increased markedly. CaP_{vir} samples did not show any increase in Ca or P signal (not shown). This observation is in agreement with what was found in section 5.3.1 for similar layers in SBF. Prenucleated samples showed gradual increase in CaP content over time, whereas CaP_{vir} samples remained inert. After day 4, the organic compound was increased to a thickness that exceeds by far the probing depth of IBA. Therefore, from day 8, Ca levels were determined with OCPC according to table 7.3, and displayed in figure 7.10.

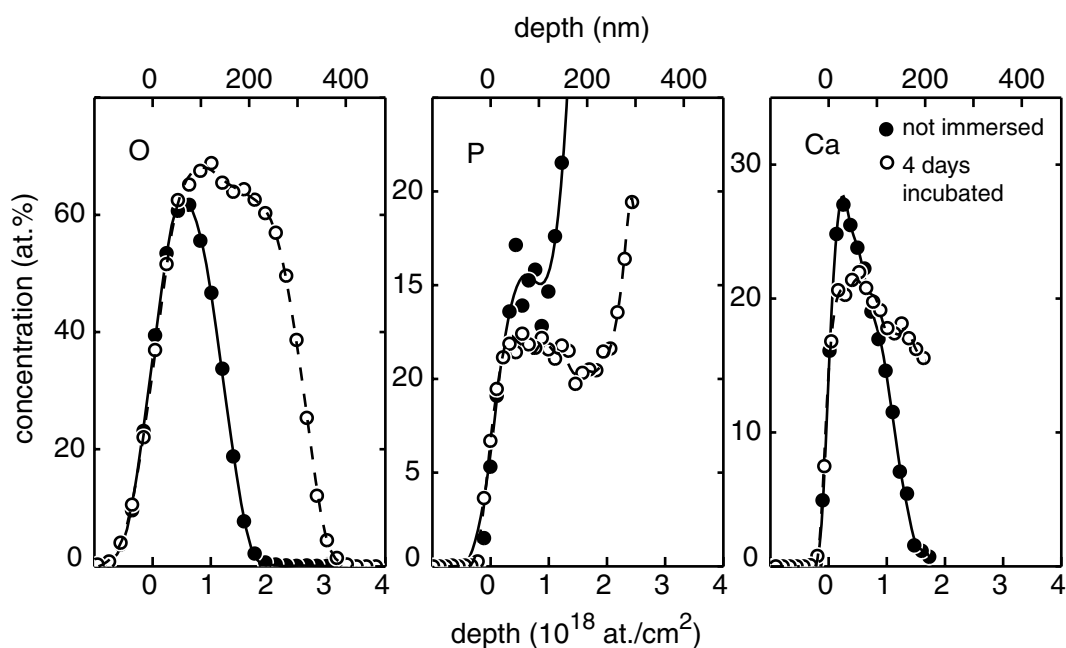


Figure 7.9: ERD depth profiles for the CaP_{pre} sample group for oxygen, phosphorus, and calcium (left to right). Full circles and solid line: a non-immersed CaP_{pre} reference. Open circles and broken line: CaP_{pre} sample after 4 days of cell culture. ERD: 66 MeV $^{63}\text{Cu}^{10+}$, $\phi=30^\circ$, $\alpha=20^\circ$.

Values at day 0 and 4 were determined from IBA. Evidently, the CaP_{vir} coatings without cells showed no increase in Ca content over the period of 24 days. On the contrary, CaP_{pre} samples show a gradually increasing Ca coverage when just incubated in culture medium. This is in agreement with the results from section 5.3.1 and similar to the observations from ERD in figure 7.9. We can estimate a linear growth rate of $\sim 1.4 \text{ nm hr}^{-1}$. This rate is quite comparable with the rate we found earlier for growth of these coatings in SBF (see section 5.3.1).

Further, evaluation of the cell cultured CaP_{vir} samples revealed no increase in Ca content up to day 8. After this period, a sharp increase can be noticed, similar to the behavior of these sample groups as found in the biocompatibility study (see figure 7.4). However, the time point at which this increase started was somewhat earlier in the current study. We see that the total Ca content at day 24 is quite similar for both studies. If we look at the CaP_{pre} samples in the cell culture we see at first the same gradual increase in CaP content as the CaP_{pre} samples in the control group without cells, but again at day 8 a sharp increase can be seen. This onset of 8 days correlates to the point where the ALP activity is decreased and the osteocalcin production starts increasing (see figure 7.8). Ca levels of the CaP_{pre} sample group are significantly higher at culture periods of 12, 16, and 24 days, and differ from the CaP_{vir} samples roughly by the amount that had grown on the pretreated coatings up to day 8.

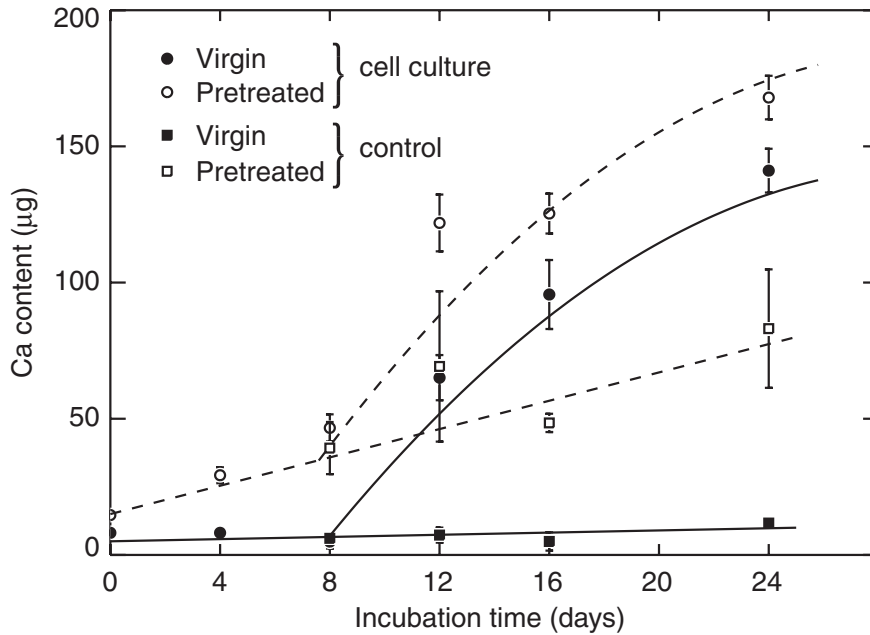


Figure 7.10: Total Ca content versus culture period. All lines are to guide the eye. The solid line follows the untreated CaP groups (CaP_{vir}), The broken line corresponds to the pretreated sample groups (CaP_{pre}). Circles are for samples that were cultured with cells, squares are controls, and were incubated without cells. Ca contents were not corrected for the contribution of the coating.

In figure 7.11 the electron micrographs of the cell culture for CaP_{pre} at day 8 (**a**) and day 16 (**b**), and for CaP_{vir} at day 8 (**c**) and day 16 (**d**) are depicted. After 8 days of culture on both the CaP_{vir} and the CaP_{pre} coatings, a confluent cell blanket is formed (**b**). On top of the CaP_{pre} coating a calcified layer can be observed in between the coating and the cell layer (**d**). After 16 days, for both the CaP_{vir} and the CaP_{pre} sample groups the presence of ECM can be seen, a network of collagen fibers with globular CaP accretions associated with it. For both groups we can now identify a directly bonded interfacial CaP layer. Collagen bundles are attached to this layer. Comparison of the directly bonded layers (**d**) on the CaP_{pre} coatings at day 8 and 16 reveals a clear increase in layer thickness from ~ 500 nm to ~ 1 μm . This observation is in agreement with the results found from the Ca content measurements in figure 7.10. If we compare the micrograph for the CaP_{vir} layer at day 16 with the CaP sample in the biocompatibility study (figure 7.6 **a**), we see in both studies the presence of a directly bonded CaP layer after 16 days. However, in the biocompatibility study still a large amount of cell material was present. In this study the ECM is present but cells are rare, which is in agreement with the sharp decrease in DNA after day 12 (figure 7.8).

In figure 7.12 the side-view electron micrographs are shown at day 16 for the cell cultured samples and the control experiments without cells. Comparison of the layer

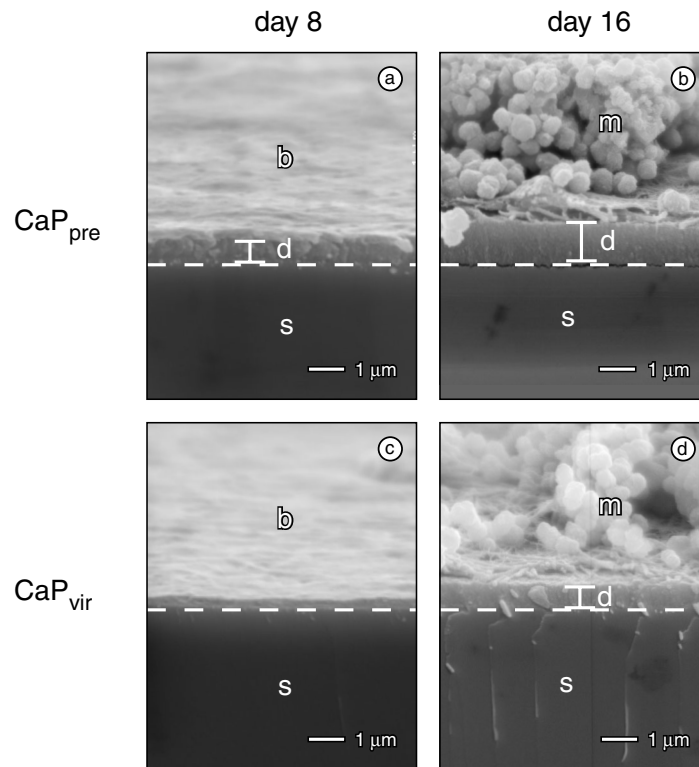


Figure 7.11: Side view electron micrographs at day 8 and 16 of the cell culture. Top row: CaP_{pre} at **a**) day 8 and **b**) day 16. Bottom row: CaP_{vir} at **c**) day 8 and **d**) day 16. Magnification: 10k. Annotations: s: substrate, b: cell blanket, d: directly bonded CaP layer, m: globular CaP accretions and collagen matrix.

thicknesses at day 16 between the CaP_{vir} and CaP_{pre} sample groups, shows that this layer is thicker for the CaP_{pre} sample group than for the CaP_{vir} group. In case of the CaP_{vir} samples without cells we do not see any apposition of CaP at all. Clearly, the formation of the directly bonded CaP layer is mediated by the activity of cells. Obviously, this also holds for the CaP accretions associated with the collagen network. For the CaP_{pre} control we can also see the presence of a surface CaP layer of comparable thickness as the cell cultured coatings.

Concluding the results in this second part: the early formation of a directly bonded CaP layer at the coating interface is obstructed by the absence of CaP nuclei; when cells start to form the ECM, they mediate the nucleation of CaP on the surface together with CaP accretions associated with the collagen network. On the other hand, if samples are pre-nucleated before incubation, immediate growth of the interfacial CaP layer commences. Again, after ECM formation, the rate of CaP apposition is increased, and CaP accretions associated with the collagen network appear.

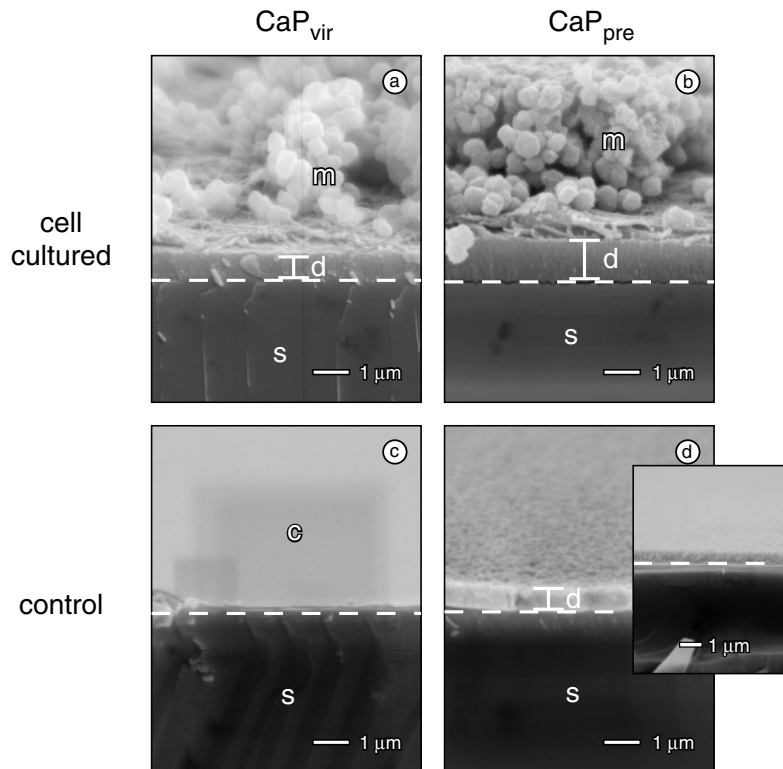


Figure 7.12: Side view electron micrographs of each sample group at day 16. Top row: cultured with cells, **a)** CaP_{vir} and **b)** CaP_{pre} . Bottom row: controls without cells, **c)** CaP_{vir} and **d)** CaP_{pre} . The inset shows a non-immersed CaP_{pre} sample. Magnification: 10k. Annotations: s: substrate, c: coating, d: directly bonded CaP layer, m: globular CaP accretions and collagen matrix.

7.5 Discussion

In the two studies described in this chapter we have evaluated the cellular response of RBM cells to thin films of RF magnetron sputtered CaP coatings and the construction *in vitro* of the interface between material and osteogenic cell layers. Firstly, we compared thin films of CaP to alumina and titania to address its biocompatibility, then we looked at the specific role of surface nucleation in the formation of the material/bone interface.

In the first part, we found that the bioactive nature of CaP was confirmed by enhanced differentiation markers, matrix production, and the formation of a directly bonded CaP rich layer. If we compare these results with those obtained with Al_2O_3 , a known bioinert material widely used in skeletal replacement, the differences are significant. We see reduced proliferation for the CaP groups, enhanced early differentiation markers and enhanced activity of mature osteoblasts (figure 7.3 **a**, **b**, and **c**). Enhanced

matrix production followed from the increased Ca contents (figure 7.4) and SEM (figure 7.6).

For TiO_2 we see intermediate behavior between the 'bioactive' sample groups (CaP) and the Al_2O_3 group. At day 8 of the biocompatibility study, DNA and ALP markers followed the Al_2O_3 group, whereas at day 12 the CaP groups were followed. Osteocalcin production and structure of the interface were similar to the CaP groups. In figure 7.6 **d** we found proof of the presence of a directly attached CaP layer, which is thought to be closely associated with the bioactivity of a bone-bonding material [103].

Another important conclusion can be drawn from the analysis of the CaP_{bulk} sample group. We do not see significant differences between this group and the thinner CaP group. Remember that the CaP_{bulk} samples are a factor of ~ 20 thicker than the CaP samples. So we see that substrate or thin film effects are negligible even for the thin coatings. We can not rule out a possible bulk effect for coating thicknesses much larger than $\sim 10 \mu\text{m}$.

For the bioinert Al_2O_3 , we saw significantly lower CaP apposition than for the other groups. This can be attributed to the absence of the directly bonded CaP layer found with the 'bioactive' materials. Further, mature osteoblast activity is lower and ECM production is less, also resulting in reduced CaP apposition.

From the prenucleation study we learned that the presence of a gradually growing CaP interface does not affect the cellular response (figure 7.8). Since the initial surface roughness of the CaP_{vir} and CaP_{pre} sample groups in this study is markedly different, also microroughness does not influence cell behavior here. There has been some debate on influence of micro-scaled surface roughness on proliferation and differentiation of rat cells [93].

If we compare the two studies, good agreement is found for the various osteogenic markers. However, we see that pronounced differences can be found per study in the average time at which the cell culture differentiates into mature osteoblasts as seen from a decrease in ALP activity and the increase in Ca levels, indicating calcification of the ECM (compare figures 7.3 and 7.8, and 7.4 and 7.10). As a marker for mature osteoblast activity, osteocalcin production can not be compared between the studies due to the sharp decrease in cell numbers at day 16 in the prenucleation study (figure 7.8 **a**). Similar observations have been reported before [99, 182]. Deviations may occur due to differences between individual rats or in the harvesting procedure, influencing the distribution of cell types in the cell population.

From both studies we see that irrespective of the material used, before the start of ECM formation by mature osteoblasts, no CaP is deposited in the cell cultures. After this differentiation period, cells mediate the formation of two types of CaP. One of globular accretions connected to the collagen bundles which is present on all materials but more abundant with the more bioactive materials. The other type of CaP is directly bonded to the coating interface. The latter is not formed on bioinert materials. From the control experiments we see that the ability to activate the formation of CaP crystals on the surface is mediated by cell activity. Without cells no CaP layer is formed on the coatings of any of the used materials even after two weeks. We can think of two

ways this process takes place. It can be direct, by providing the surface with proteins able to act as nucleation centers for CaP. It can also be indirect, by increasing ion activities locally to overcome the activation barrier. Possible mechanisms for this were discussed in section 7.1.

From ERD, OCPC, and SEM results in the prenucleation study we have clearly shown that if the nucleation step is taken and crystals are formed, no cell intervention is needed to have a gradually growing CaP layer on top of the coating right from the start of the cell culture. The cell blanket covering the coating does not hinder its growth; growth rates are comparable with rates in the control experiment. Also possible promoting and inhibitory processes do not have dramatic effects on the growth rate, or they cancel out, given the similar growth rates found under simulated conditions (see chapter 5).

The different mechanisms contributing to the formation of the interface structure of a CaP coating with and without pretreatment are summarized in figure 7.13. The

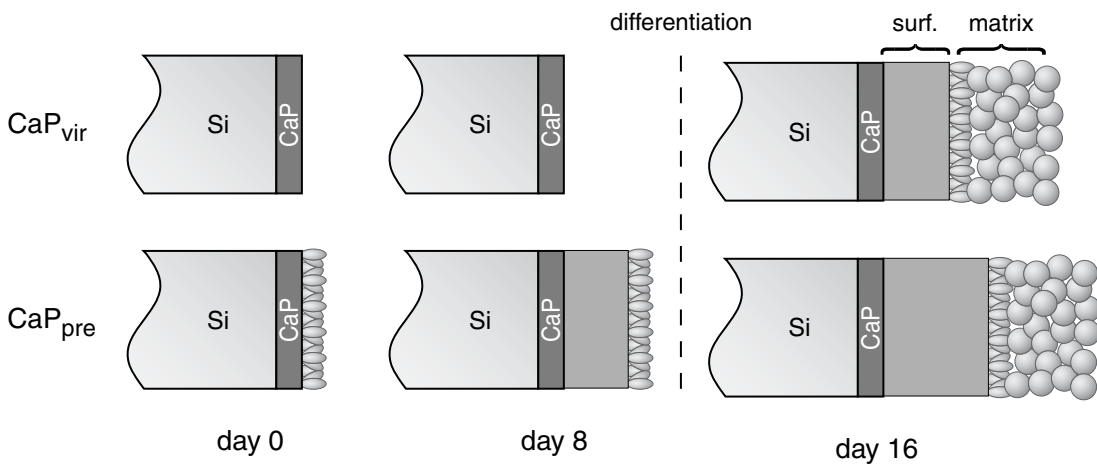


Figure 7.13: Formation of the interface structure for CaP_{vir} and CaP_{pre} samples. Only with the prenucleated samples a directly bonded CaP layer can grow from the start of the cell culture. For the CaP_{vir} samples nucleation has to be activated by cell mediation. This happens when more cells in the culture have differentiated into a mature osteoblastic phenotype and ECM is formed. Now the ECM can be calcified and globular accretions can be found connected to the collagen network.

pathway followed by the CaP_{vir} sample group is typical for the 'bioactive' sample groups and the TiO_2 sample group. The surface is inert until mature osteoblast activity is able to provide the free energy to nucleate the surface. Until then, the coating surface remains inert and unable to grow CaP crystals. The formation of the surface layer coincides with the formation and calcification of the ECM. From here, two types of CaP precipitation can be identified, one attached to the surface, the other as globular accretions attached to the collagen network. The two forms of CaP depositions are

connected in the sense that both are created at the same time. The pre-nucleated surface on the other hand, allows continuous growth of the directly bonded CaP rich layer from the start of the cell culture, long before the formation of the ECM. In fact, both types of CaP apposition have effectively been decoupled. Continuous growth proceeds until cell culture properties are dominated by mature ECM forming osteoblasts. Then, the growth rate is sharply increased. We suggest that the growth of the surface layer proceeds gradually and the increase is due to the calcification of the newly formed collagen network. Probably, growth of the surface layer comes to a halt only when diffusion is hampered by the coagulation of the ECM.

7.6 Conclusions

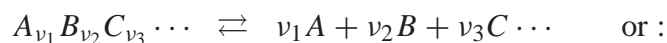
From the cytocompatibility study we conclude that the CaP coated samples show bioactive behavior when compared to the bioinert Al_2O_3 . This is apparent from both cell differentiation markers and the formation of a directly bonded CaP layer. The TiO_2 coated samples showed intermediate proliferation and differentiation behavior. However, on TiO_2 a directly bonded CaP layer could be identified. Further, from the pre-nucleation study it is clear that the early formation of a directly bonded CaP layer on CaP coatings is obstructed by the absence of CaP nuclei. After ~ 8 days, cell activity induces the nucleation of CaP crystals on both the surface and the ECM, and growth is enhanced. By pretreatment of the coatings growth of the directly bonded CaP layer is immediate. Hence, the formation of the interfacial CaP layer and the matrix associated CaP accretions can effectively be decoupled.

Thermodynamics of Dissolution and Precipitation of Sparingly Soluble Salts

To understand the equilibrium behavior of crystal growth and dissolution of sparingly soluble salts in aqueous media, it is important to understand the thermodynamics of this system. Firstly, we will derive an expression for the free energy change due the precipitation (or dissolution) process. We will show how this can be simplified to a widely used expressions for the free energy change. Also, we will introduce a *saturation index* that is closely related to the free energy and which shows directly whether the solution is oversaturated, undersaturated, or in equilibrium with the precipitate.

Let us now look in detail at the driving force for CaP precipitation and dissolution. We will focus on solutions with a ionic strength of about 0.1 M that is determined by an excess of non-interacting (*swamping*) electrolyte. This will guarantee that changes in the solution concentration of the lattice constituent ions (LCI) will hardly affect the overall ionic strength, and thus will not affect the activity coefficients for these ions. On the other hand, activity coefficients at a ionic strength of about 0.1 M can still be well approximated using the Davies equation.

We will look at a sparingly soluble crystal $A_{\nu_1}B_{\nu_2}C_{\nu_3} \cdots$ that dissolves according to the reaction \mathcal{R} , or precipitates according to $-\mathcal{R}$:



$$0 = \underbrace{\sum_j X_{j,v_j}}_{\text{products}} - \underbrace{X_{1,v_1} X_{2,v_2} X_{3,v_3} \cdots}_{\text{reactant}} \quad (\text{A.1})$$

with : $X_j = A, B, C \cdots$.

Here we followed the convention that the reaction proceeds from reactants towards its separated products.

The differential free energy change of this reaction under constant pressure and temperature will be:

$$d_r G = \sum_j \mu_j d\widehat{N}_j \quad p, T \text{ constant.} \quad (\text{A.2})$$

In table A.1 definitions are given for the used reaction quantities.

M_s	Solvent mass in kg.
N_j, n_j, m_j, a_j	Number of particles/number of moles of particles/molality/activity of lattice constituent ion (LCI) j . Note that $N_A M_s m_j = N_j$.
$\widehat{N}_j, (\widehat{n}_j), [\widehat{m}_j]$	Consumed amount (of moles) of LCI j [per kg solvent] via reaction \mathcal{R} .
$\widehat{N}, (\widehat{n}), [\widehat{m}]$	Consumed amount (of moles) of lattice cells [per kg solvent] via reaction \mathcal{R} .
$m_{j,b}$	Molality of LCI j in the solution of interest, so before precipitation.
$\Delta\widehat{m}_j$	Total amount of moles of consumed LCI j per kg solvent at equilibrium.
$\Delta\widehat{N}, (\Delta\widehat{n}), [\Delta\widehat{m}]$	Total amount of (moles) consumed lattice cells [per kg solvent] at equilibrium.
K_{sp}	Solubility product.
IAP	Ion activity product. $\log \text{IAP} = \sum_j \nu_j \log a_j$.
N_A	Avogadro's number.
$^\circ$	Standard state (refer to [183]).

Table A.1: Explanation of the used reaction quantities. A hat on variables and constants refers to quantities that react according to stoichiometric ratios ν_j between the LCIS.

To calculate the total free energy difference between the solution under consideration (b) and the equilibrium solution (eq) after a maximum consumption via reaction \mathcal{R} , we integrate expression (A.2) to get:

$$\begin{aligned} \Delta_r G &= \int_b^{eq} d_r G \\ &= \int_b^{eq} \sum_j \mu_j d\widehat{N}_j, \end{aligned}$$

(A.3)

and thus for the total molar free energy we may write:

$$\Delta_r G = \underbrace{\frac{M_s}{\Delta \hat{n}} \int_0^{\Delta \hat{m}_j} \sum_j \mu_j^\circ d\hat{m}_j}_{I_1} + \underbrace{\frac{M_s}{\Delta \hat{n}} \int_0^{\Delta \hat{m}_j} \sum_j RT \log a_j d\hat{m}_j}_{I_2}. \quad (\text{A.4})$$

Here we imposed the restraint that the reaction is stoichiometric, and we used that $N_A M_s \hat{m}_j = \hat{N}_j$, which is valid if the amount of solute is small compared with the solvent. First we will rewrite the activity in terms of the molalities of the solution LCIS:

$$\begin{aligned} a_j &= \gamma_j \frac{m_j}{m^\circ} = c_j m_j \\ a_j(\hat{m}_j) &= c_j (m_{j,b} + \alpha_j \hat{m}_j) \\ \text{with } \alpha_j &= \frac{m_{j,eq} - m_{j,b}}{\Delta \hat{m}_j} = \frac{v_{j,eff}}{v_j}. \end{aligned}$$

Here the α_j was introduced to account for the redistribution of other species (for example the P_i equilibrium). Note that the ionic activity coefficients γ_j will be independent of the reaction coordinate \hat{m} due to the indifferent swamping electrolyte. For the CaP solutions we will study, we checked that α_j is constant within 10% over a wide range of Ca and PO_4 concentrations. Therefore we will assume that α_j is independent of \hat{m} . Now we will address the integrals in expression (A.4):

$$\begin{aligned} I_1 &= \frac{M_s}{\Delta \hat{n}} \int_0^{\Delta \hat{m}_j} \sum_j \mu_j^\circ d\hat{m}_j \\ &= \frac{M_s \Delta \hat{m}_j}{\Delta \hat{n}} \sum_j v_j \mu_j^\circ = \sum_j v_j \mu_j^\circ. \end{aligned} \quad (\text{A.5})$$

In equilibrium, G will be minimal and hence:

$$\begin{aligned} \left[\frac{\partial_r G_j}{\partial \hat{n}} \right]_{p,T} &= \mu_j = 0 \\ \mu_j &= \mu_j^\circ + RT \log a_{j,eq} = 0 \\ \text{so : } \mu_j^\circ &= -RT \log a_{j,eq}. \end{aligned} \quad (\text{A.6})$$

Now, by inserting (A.6) in (A.5) we have:

$$\begin{aligned} I_1 &= -RT \sum_j v_j \log a_{j,eq} \\ &= -RT \log K_{sp}. \end{aligned} \quad (\text{A.7})$$

If we look back at equation A.4, we can now find an expression for the standard molar formation energy, $\Delta_f G$. The formation energy is given with respect to the standard state of the solution, i.e., all the solution activities will be 1. Since also the activities of the solid are 1, I_2 will vanish and we have:

$$\Delta_f G^\ominus = -RT \log K_{\text{sp}}. \quad (\text{A.8})$$

For I_2 in (A.4) we can derive the following:

$$\begin{aligned} I_2 &= \frac{M_s}{\Delta \widehat{n}} \int_0^{\Delta \widehat{m}_j} \sum_j RT \log a_j d\widehat{m}_j \\ &= \frac{M_s}{\Delta \widehat{n}} RT \sum_j \left[\frac{m_{j,b}}{\alpha_j} \log \frac{m_{j,b} + \alpha_j \Delta \widehat{m}_j}{m_{j,b}} + \right. \\ &\quad \left. \Delta \widehat{m}_j \log c_j (m_{j,b} + \alpha_j \Delta \widehat{m}_j) - \Delta \widehat{m}_j \right] \\ &= RT \sum_j \left[\underbrace{\frac{v_j}{\frac{a_{j,b}}{a_{j,eq}} - 1} \log \frac{a_{j,b}}{a_{j,eq}}}_I + \underbrace{v_j \log a_{j,b}}_{\text{II}} - \underbrace{v_j}_{\text{III}} \right]. \end{aligned} \quad (\text{A.9})$$

We can distinguish several different limits for $a_{j,b}$. First we have for $a_{j,b} \rightarrow a_{j,eq}$ that $\Delta_r G = 0$. Secondly, in the limit of large supersaturation $a_{j,b} \gg a_{j,eq}$, but still $|\log a_{j,b}| \gg 1$, we have that in expression (A.9) terms I and III will be small compared to term II, and thus inserting (A.7), (A.9) in (A.4):

$$\begin{aligned} \Delta_r G &= -RT \log K_{\text{sp}} + RT \sum_j v_j \log a_{j,b} \\ &= RT [\log \text{IAP} - \log K_{\text{sp}}] \end{aligned}$$

$$\text{and thus : } \Delta_{\text{diss}} G = \Delta_r G = RT \log \frac{\text{IAP}}{K_{\text{sp}}} \equiv RT \cdot \text{SI}. \quad (\text{A.10})$$

Here SI is the so called Saturation Index. With a positive SI the solution is supersaturated with respect to the corresponding phase. With a negative SI the solution is undersaturated, and with zero SI the solution is in equilibrium with the solid phase.

Remember that equation A.10 is valid only for the standard reaction direction, which is the dissolution of the solid. For the precipitation reaction ($-\mathcal{R}$ denoted with $-r$), the v_j 's in formula A.2 change sign, and thus $\text{IAP} \rightarrow 1/\text{IAP}$. Equation A.10 can be rewritten for precipitation as:

$$\Delta_{\text{prec}} G = \Delta_{-r} G = -RT \log \frac{\text{IAP}}{K_{\text{sp}}}. \quad (\text{A.11})$$

Bibliography

- [1] R.J.M. Perenboom, L.M. van Herten, and N. Hoeymans. Trends in gezonde levensverwachting: Nederland. Technical Report Rapportnummer: 2002.206, TNO Preventie en Gezondheid, 2002.
- [2] A.S. Greenwald, S.D. Boden, V.M. Goldberg, Y. Khan, C.T. Laurencin, and R.N. Rosier. Bone-graft substitutes: facts, fictions, and applications. *J. Bone Joint Surg.*, 83-A:98–103, 2001.
- [3] L.L. Hench and E.C. Ethridge. *Biomaterials, an Interfacial Approach*, volume 4 of *Biophysics and Bioengineering Series*. Academic Press, inc., London, 1982.
- [4] L.L. Hench. Bioceramics. *J. Am. Ceram. Soc.*, 81:1705–1728, 1998.
- [5] J. Black. *Biological Performance of Materials: Fundamentals of Biocompatibility*. Marcel Dekker, New York, 1999.
- [6] J.F. Osborn and H. Newesely. *Dental Implants*, chapter Dynamic Aspects of the Implant/Bone Interface. C. Hansen Verlag, Munich, 1980.
- [7] G. Heimke. The aspects and modes of fixation of bone replacements. In *Osseointegrated Implants*, pages 1–29. CRC Press, Boca Raton, FL., 1990.
- [8] D.F. Williams, J. Black, and P.J. Doherty. Second consensus conference on definitions in biomaterials. Number 10 in *Advances in Biomaterials*, pages 525 – 533, Chester, UK, 1991.
- [9] R.B. Martin. Biomaterials. In S.A. Berger, E.W. Goldsmith, and E.R. Lewis, editors, *Introduction to Bioengineering*, pages 339–360. Oxford University Press, 1996.
- [10] T.A. Horbett, B.D. Ratner, J.M. Schakenraad, and F.J. Schoen. Some background concepts. In B.D. Ratner, A.S. Hoffman, F.J. Schoen, and J.E. Lemons, editors, *Biomaterials Science*, pages 133–164. Academic Press, 1996.
- [11] S.L. Cooper and N.A. Peppas, editors. *Biomaterials: Interfacial Phenomena and Applications*, volume 199 of *Advances in Chemistry Series*. American Chemical Society, 1982.

- [12] K. Anselme. Osteoblast adhesion on biomaterials. *Biomaterials*, 21:667–681, 2000.
- [13] P. Ducheyne, T. Kokubo, and C.A. van Blitterswijk, editors. *Bone-bonding Biomaterials*. Reed Healthcare Communications, Leiderdorp, The Netherlands, 1992.
- [14] L. Vroman and A.L. Adams. Identification of rapid changes at plasma-solid interfaces. *J. Biomed. Mat. Res.*, 3:43–67, 1969.
- [15] K.K. Chittur. FTIR/ATR for protein adsorption to biomaterial surfaces. *Biomaterials*, 19:357–369, 1998.
- [16] R.Z. LeGeros. *Calcium Phosphates in Oral Biology and Medicine*, volume 15 of *Mono-graphs in Oral Science*. Karger, Basel, Switzerland, 1991.
- [17] J.C. Elliot. *Structure and Chemistry of the Apatites and Other Calcium Orthophosphates*, volume 18 of *Studies in Inorganic Chemistry*. Elsevier Science B.V., 1994.
- [18] S.V. Dorozhkin. A review on the dissolution models of calcium apatites. *Prog. Crystal Growth Charact.*, 44:45–61, 2002.
- [19] M.B. Fawzi, J.L. Fox, M.G. Dedhiya, W.I. Higuchi, and J.J. Hefferren. A possible second site for hydroxyapatite dissolution in acidic media. *J. Colloid Interface Sci.*, 67:304–311, 1978.
- [20] J.L. Fox, W.I. Higuchi, M.B. Fawzi, and M-S. Wu. A new two-site model for hydroxyapatite dissolution in acidic media. *J. Colloid Interface Sci.*, 67, 1978.
- [21] W.I. Higuchi, E.Y. Cesar, P.W. Cho, and J.L. Fox. Powder suspension method for critically re-examining the two-site model for hydroxyapatite dissolution kinetics. *J. Pharmac. Sci.*, 73:146–153, 1984.
- [22] J. Christoffersen, M.R. Christoffersen, and N. Kjaergaard. The kinetics of dissolution of calcium hydroxyapatite in water at constant pH. *J. Crystal Growth*, 43:501–511, 1978.
- [23] J. Christoffersen and M.R. Christoffersen. Kinetics of dissolution of calcium hydroxyapatite II. Dissolution in non-stoichiometric solutions at constant pH. *J. Crystal Growth*, 47:671–679, 1979.
- [24] J. Christoffersen. Kinetics of dissolution of calcium hydroxyapatite III. Nucleation-controlled dissolution of a polydisperse sample of crystals. *J. Crystal Growth*, 49:29–44, 1980.
- [25] J. Christoffersen and M.R. Christoffersen. Kinetics of dissolution of calcium hydroxyapatite IV. The effect of some biologically important inhibitors. *J. Crystal Growth*, 53:42–54, 1981.
- [26] M.R. Christoffersen and J. Christoffersen. Kinetics of dissolution of calcium hydroxyapatite VII. The effect of fluoride ions. *J. Crystal Growth*, 67:107–114, 1984.
- [27] S. Mafé, J.A. Manzanares, H. Reiss, J.-M. Thomann, and Ph. Gramain. Model for the dissolution of calcium hydroxyapatite powder. *J. Phys. Chem.*, 96:861–866, 1992.
- [28] Ph. Gramain, J.-M. Thomann, M. Gumpper, and J.-C. Voegel. Dissolution kinetics of human enamel powder I. Stirring effects and surface calcium accumulation. *J. Colloid Interface Sci.*, 128:370–381, 1989.
- [29] J.-M. Thomann, J.-C. Voegel, M. Gumpper, and Ph. Gramain. Dissolution kinetics of human enamel powder II. A model based on the formation of a self-inhibiting surface layer. *J. Colloid Interface Sci.*, 132:403–412, 1989.

- [30] J.-M. Thomann, J.-C. Voegel, and Ph. Gramain. Kinetics of dissolution of calcium hydroxyapatite powder III. pH and sample conditioning effects. *Calcif. Tissue Int.*, 46:121–129, 1990.
- [31] J.-M. Thomann, J.-C. Voegel, and Ph. Gramain. Kinetics of dissolution of calcium hydroxyapatite powder IV. Interfacial calcium diffusion controlled process. *Colloids Surf.*, 54:145–159, 1991.
- [32] J.-M. Thomann, J.-C. Voegel, and Ph. Gramain. Quantitative model for the dissolution of calcium hydroxyapatite with a permselective ionic interface. *J. Colloid Interface Sci.*, 157:369–374, 1993.
- [33] J.A. Budz and G.H. Nancollas. The mechanisms of dissolution of hydroxyapatite and carbonated apatite in acidic solutions. *J. Crystal Growth*, 91:490–496, 1988.
- [34] E.M. Burke and G.H. Nancollas. Relation of lattice ion solution composition to octacalcium phosphate dissolution kinetics. *Colloids Surf.*, 150:151–160, 1999.
- [35] L.J. Shyu, L. Perez, S.J. Zawacki, J.C. Heughebaert, and G.H. Nancollas. The solubility of octacalcium phosphate at 37°C in the system $\text{Ca}(\text{OH})_2\text{-H}_3\text{PO}_4\text{-KNO}_3\text{-H}_2\text{O}$. *J. Dent. Res.*, 62:398–400, 1983.
- [36] J. Zhang and G.H. Nancollas. Kinetics and mechanisms of octacalcium phosphate dissolution at 37°C. *J. Phys. Chem.*, 96:5478–5483, 1992.
- [37] W.C. Chen and G.H. Nancollas. The kinetics of dissolution of tooth enamel – A constant composition study. *J. Dent. Res.*, 65:663–668, 1986.
- [38] H.G. Linge and G.H. Nancollas. A rotating disc study of the dissolution of dental enamel. *Calc. Tiss. Res.*, 12:193–208, 1973.
- [39] E.P. Paschalis, J. Tan, and G.H. Nancollas. Constant composition dissolution kinetics studies of human dentin. *J. Dent. Res.*, 75:1019–1026, 1996.
- [40] A. Ebrahimpour, J. Zhang, and G.H. Nancollas. Dual constant composition method and its application to studies of phase transformation and crystallization of mixed phases. *J. Crystal Growth*, 113:83–91, 1991.
- [41] H. Hohl, P.G. Koutsoukos, and G.H. Nancollas. The crystallization of hydroxyapatite and dicalcium phosphate dihydrate; representation of growth curves. *J. Crystal Growth*, 57:325–335, 1982.
- [42] J. Zhang and G.H. Nancollas. Interpretation of dissolution kinetics of dicalcium phosphate dihydrate. *J. Crystal Growth*, 125:251–269, 1992.
- [43] G.H. Nancollas and B.E. Tucker. Dissolution kinetics characterization of hydroxyapatite coatings on dental implants. *J. Oral Implant.*, 20:221–226, 1994.
- [44] R. Boistelle and I. Lopez-Valero. Growth units and nucleation: the case of calcium phosphates. *J. Crystal Growth*, 102:609–617, 1990.
- [45] C. Combes, M. Freche, and C. Rey. Nucleation and crystal growth of dicalcium phosphate dihydrate on titanium powder. *J. Mater. Sci. Mater. Med.*, 6:699–702, 1995.
- [46] P.G. Koutsoukos and G.H. Nancollas. Crystal growth of calcium phosphates – Epitaxial considerations. *J. Crystal Growth*, 53:10–19, 1981.
- [47] Y. Liu, W. Wu, G. Sethuraman, and G.H. Nancollas. Intergrowth of calcium phosphates: an interfacial energy approach. *J. Crystal Growth*, 174:386–392, 1997.

- [48] W. Wu and G.H. Nancollas. Interfacial free energies and crystallization in aqueous media. *J. Colloid Interface Sci.*, 182:365–373, 1996.
- [49] W. Wu, H. Zhuang, and G.H. Nancollas. Heterogeneous nucleation of calcium phosphates on solid surfaces in aqueous solution. *J. Biomed. Mat. Res.*, 35:93–99, 1997.
- [50] M.R. Christoffersen, J. Dohrup, and J. Christoffersen. Kinetics of growth and dissolution of calcium hydroxyapatite in suspensions with variable calcium to phosphate ratio. *J. Crystal Growth*, 186:283–290, 1998.
- [51] G.H. Nancollas and W. Wu. Biomineralization mechanisms: a kinetics and interfacial energy approach. *J. Crystal Growth*, 211:137–142, 2000.
- [52] B.N. Bachra and H.R.A. Fischer. The effect of some inhibitors on the nucleation and crystal growth of apatite. *Calc. Tiss. Res.*, 3:348–357, 1969.
- [53] F. Abbona and A. Baronnet. A XRD and TEM study on the transformation of amorphous calcium phosphate in the presence of magnesium. *J. Crystal Growth*, 165:98–105, 1996.
- [54] T.A. Fuierer, M. LoRe, S.A. Puckett, and G.H. Nancollas. A mineralization adsorption and mobility study of hydroxyapatite surfaces in the presence of zinc and magnesium ions. *Langmuir*, 10:4721–4725, 1994.
- [55] Y. Xu, F.W. Schwartz, and S.J. Traina. Sorption of Zn^{2+} and Cd^{2+} on hydroxyapatite surfaces. *Environ. Sci. Technol.*, 28:1472–1480, 1994.
- [56] F. Barrère, P. Layrolle, C.A. van Blitterswijk, and K. de Groot. Biomimetic calcium phosphate coatings on Ti_6Al_4V : a crystal growth study of octacalcium phosphate and inhibition by Mg^{2+} and HCO_3^- . *Bone*, 25:107S–111S, 1999.
- [57] S. Ban, M. Matsuura, N. Arimoto, J. Hayashizaki, Y. Itoh, and J. Hasegawa. Factors affecting the transformation of octacalcium phosphate to apatite in vitro. *Dental Materials Journal*, 12:106–117, 1993.
- [58] G.K. Hunter, P.V. Hauschka, A.R. Poole, L.C. Rosenberg, and H.A. Goldberg. Nucleation and inhibition of hydroxyapatite formation by mineralized tissue proteins. *Biochem. J.*, 317:59–65, 1996.
- [59] A. Zieba, G. Sethuraman, F. Perez, G.H. Nancollas, and D. Cameron. Influence of organic phosphonates on hydroxyapatite crystal growth kinetics. *Langmuir*, 12:2853–2858, 1996.
- [60] F. Abbona, H.E. Lundager Madsen, and R. Boistelle. The initial phases of calcium and magnesium phosphates precipitated from solutions of high to medium concentrations. *J. Crystal Growth*, 74:581–590, 1986.
- [61] T.P. Feenstra and P.L. de Bruyn. Formation of calcium phosphates in moderately supersaturated solutions. *J. Phys. Chem.*, 83:475–479, 1979.
- [62] M.J.J.M. van Kemenade and P.L. de Bruyn. A kinetic study of precipitation from supersaturated calcium phosphate solutions. *J. Colloid Interface Sci.*, 118:564–585, 1987.
- [63] K. de Groot, editor. *Bioceramics of Calcium Phosphate*. CRC Press Inc., Boca Raton, FL., 1983.
- [64] L.G. Ellies, D.G.A. Nelson, and J.D.B. Featherstone. Crystallographic changes in calcium phosphates during plasma-spraying. *Biomaterials*, 13:313–316, 1992.
- [65] M.J. Filiaggi, R.M. Pilliar, and N.A. Coombs. Post-plasma-spraying heat treatment of

- the HA coating/Ti₆Al₄V implant system. *J. Biomed. Mat. Res.*, 27:191–198, 1993.
- [66] P. Frayssinet, F. Tourenne, N. Rouguet, P. Conte, C. Delga, and G. Bonel. Comparative biological properties of HA plasma-sprayed coatings having different crystallinities. *J. Mater. Sci. Mater. Med.*, 5:11–17, 1994.
- [67] S-W. Ha, K-L. Eckert, M. Petitmermet, J. Mayer, E. Wintermantel, C. Baerlocher, and H. Gruner. Chemical and morphological changes of vacuum-plasma-sprayed hydroxyapatite coatings during immersion in simulated physiological solutions. *J. Am. Ceram. Soc.*, 81:81–88, 1998.
- [68] B. Koch, J.G.C. Wolke, and K. de Groot. X-ray diffraction studies on plasma-sprayed calcium phosphate-coated implants. *J. Biomed. Mat. Res.*, 24:655–667, 1990.
- [69] R. McPherson, N. Gane, and T.J. Bastow. Structural characterization of plasma-sprayed hydroxylapatite coatings. *J. Mater. Sci. Mater. Med.*, 6:327–334, 1995.
- [70] J. Weng, Q. Liu, J.G.C. Wolke, D. Zhang, and K. de Groot. The role of amorphous phase in nucleating bone-like apatite on plasma-sprayed hydroxyapatite coatings in simulated body fluid. *J. Mater. Sci. Let.*, 16:335–337, 1997.
- [71] P. Ducheyne, W. Van Raemdonck, J.C. Heughebaert, and M. Heughebaert. Structural analysis of hydroxyapatite coatings on titanium. *Biomaterials*, 7:97–103, 1986.
- [72] C.S. Kim and P. Ducheyne. Compositional variations in the surface and interface of calcium phosphate ceramic coatings on Ti and Ti₆Al₄V due to sintering and immersion. *Biomaterials*, 12:461–469, 1991.
- [73] M. Shirkanzadeh. Electrochemical preparation of bioactive calcium phosphate coatings on porous substrates by the periodic pulse technique. *J. Mater. Sci. Let.*, 12:16–19, 1993.
- [74] M. Yoshinari, K. Ozeki, and T. Sumii. Properties of hydroxyapatite-coated Ti₆Al₄V alloy produced by the ion-plated method. *The Bulletin of Tokyo Dental College*, 32:147–156, 1991.
- [75] T.S. Chen and W.R. Lacefield. Crystallization of ion beam deposited calcium phosphate coatings. *J. Mater. Res.*, 9:1284–1290, 1994.
- [76] X. Li, J. Weng, W. Tong, C. Zuo, X. Zhang, P. Wang, and Z. Liu. Characterization of hydroxyapatite film with mixed interface by Ar⁺ ion beam enhanced deposition. *Biomaterials*, 18:1487–1493, 1997.
- [77] M. Yoshinari, Y. Ohtsuka, and T. Dérand. Thin hydroxyapatite coating produced by the ion beam dynamic mixing method. *Biomaterials*, 1994.
- [78] J.L. Arias, M.B. Mayor, J. Pou, B. León, and M. Pérez-Amor. Stoichiometric transfer in pulsed laser deposition of hydroxylapatite. *Appl. Surf. Sci.*, 154-155:434–438, 2000.
- [79] L. Clèries, J.M. Fernández-Pradas, G. Sardin, and J.L. Morenza. Application of dissolution experiments to characterise the structure of pulsed laser-deposited calcium phosphate coatings. *Biomaterials*, 20:1401–1405, 1999.
- [80] C.M. Cotell, D.B. Chrisey, K.S. Grabowski, J.A. Spragus, and C.R. Gossett. Pulsed laser deposition of hydroxyapatite thin films on Ti₆Al₄V. *Journal of Applied Biomaterials*, 3:87–93, 1992.
- [81] M. Jelínek, V. Olšan, L. Jastrabík, V. Studnička, V. Hnatowicz, J. Kvítek, V. Havránek, T. Dostálová, I. Zergioti, A. Petrakis, E. Hontzopoulos, and C. Fotakis. Effect of pro-

- cessing parameters on the properties of hydroxylapatite films grown by pulsed laser deposition. *Thin Solid Films*, 257:125–129, 1995.
- [82] C.M. Lopatin, V.B. Pizziconi, and T.L. Alford. Crystallization kinetics of sol-gel derived hydroxyapatite thin films. *J. Mater. Sci. Mater. Med.*, 12:767–773, 2001.
- [83] R. Viitala, M. Jokinen, T. Peltola, K. Gunnelius, and J.B. Rosenholm. Surface properties of in vitro bioactive and non-bioactive sol-gel derived materials. *Biomaterials*, 83:89–95, 2002.
- [84] F. Barrère, P. Layrolle, C.A. van Blitterswijk, and K. de Groot. Physical and chemical characteristics of plasma-sprayed and biomimetic apatite coating. In H. Ohgushi, G.W. Hastings, and T. Yoshikawa, editors, *Bioceramics. Proceedings of the Twelfth International Symposium on Ceramics in Medicine*, volume 12, pages 125–128. World Scientific Publishing Co, Pte. Ltd., 1999.
- [85] H.-M. Kim, Y. Kim, S.-J. Park, C. Rey, H.M. Lee, M.J. Glimcher, and J.S. Ko. Thin film of low-crystalline calcium phosphate apatite formed at low temperature. *Biomaterials*, 21:1129–1134, 2000.
- [86] F. Li, Q.L. Feng, F.Z. Cui, H.D. Li, and H. Schubert. A simple biomimetic method for calcium phosphate coating. *Surface and Coatings Technology*, 154:88–93, 2002.
- [87] T.P. Niesen and M.R. De Guire. Review: Deposition of ceramic thin films at low temperatures from aqueous solutions. *Journal of Electroceramics*, 6:169–207, 2001.
- [88] S. Swann. Magnetron sputtering. *Phys. Technol.*, 19:67–75, 1988.
- [89] B. Window. Recent advances in sputter deposition. *Surface and Coatings Technology*, 71:93–97, 1995.
- [90] J.A. Jansen, J.G.C. Wolke, S. Swann, J.P.C.M. van der Waerden, and K. de Groot. Application of magnetron sputtering for producing ceramic coatings on implant materials. *Clin. Oral Impl. Res.*, 4:28–34, 1993.
- [91] J.E.G. Hulshoff, K. van Dijk, J.E. de Ruijter, F.J.R. Rietveld, L.A. Ginsel, and J.A. Jansen. Interfacial phenomena: an in vitro study of the effect of calcium phosphate (Ca-P) ceramic on bone formation. *J. Biomed. Mat. Res.*, 40:464–474, 1998.
- [92] S. Nakamura, M. Ohgaki, T. Kobayashi, J.-I. Hamagami, and K. Yamashita. Biological evaluation and surface properties of bonelike hydroxyapatite thin films prepared by RF-sputtering method. In H. Ohgushi, G.W. Hastings, and T. Yoshikawa, editors, *Bioceramics. Proceedings of the Twelfth International Symposium on Ceramics in Medicine*, volume 12, pages 467–470. World Scientific Publishing Co. Pte. Ltd, 1999.
- [93] P.J. Ter Brugge, J.G.C. Wolke, and J.A. Jansen. Effect of calcium phosphate coating crystallinity and implant surface roughness on differentiation of rat bone marrow cells. *J. Biomed. Mat. Res.*, 60:70–78, 2002.
- [94] K. van Dijk, H.G. Schaeken, C.H.M. Marée, J. Verhoeven, J.C.G. Wolke, F.H.P.M. Habraken, and J.A. Jansen. Influence of Ar pressure on r.f. magnetron-sputtered $\text{Ca}_5(\text{PO}_4)_3\text{OH}$ layers. *Surface and Coatings Technology*, 76-77:206–210, 1995.
- [95] K. van Dijk, H.G. Schaeken, J.G.C. Wolke, and J.A. Jansen. Influence of annealing temperature on RF magnetron sputtered calcium phosphate coatings. *Biomaterials*, 17:405–410, 1996.
- [96] J.G.C. Wolke, J.P.C.M. van der Waerden, K.de Groot, and J.A. Jansen. Stability of

- radiofrequency magnetron sputtered calcium phosphate coatings under cyclically loaded conditions. *Biomaterials*, 18:483–488, 1997.
- [97] K. Yamashita, T. Arashi, K. Kitagaki, S. Yamada, and T. Umegaki. Preparation of apatite thin films through RF-sputtering from calcium phosphate glasses. *J. Am. Ceram. Soc.*, 77:2401–2407, 1994.
- [98] B. Feddes, J.G.C. Wolke, J.A. Jansen, and A.M. Vredenberg. Initial deposition of calcium phosphate ceramic on polystyrene and polytetrafluoroethylene by RF magnetron sputtering deposition. *J. Vac. Sci. Technol. A*, 21:363–368, 2003.
- [99] P.J. Ter Brugge, R. Torensma, J.E. de Ruijter, C.G. Figdor, and J.A. Jansen. Modulation of integrin expression on rat bone marrow cells by substrates with different surfaces. *Tissue Eng.*, 8:615–626, 2002.
- [100] T. Kokubo, S. Ito, Z.T. Huang, T. Hayashi, S. Sakka, T. Kitsugi, and T. Yamamuro. Ca, P-rich layer formed on high-strength bioactive glass-ceramic A-W. *J. Biomed. Mat. Res.*, 24:331–343, 1990.
- [101] T. Kokubo, H. Kushitani, S. Sakka, T. Kitsugi, and T. Yamamuro. Solution able to reproduce in vivo surface-structure changes in bioactive glass-ceramic A-W. *J. Biomed. Mat. Res.*, 24:721–734, 1990.
- [102] H.-M Kim, T. Miyazaki, T. Kokubo, and T. Nakamura. Revised simulated body fluid. In *Bioceramics. Proceedings of the Thirteenth International Symposium on Ceramics in Medicine*, volume 13 of *Key Engineering Materials*, pages 47–50, Switzerland, 2000. Trans Tech Publications.
- [103] P. Ducheyne and Q. Qiu. Bioactive ceramics: the effect of surface reactivity on bone formation and bone cell function. *Biomaterials*, 20:2287–2303, 1999.
- [104] P.A. Campbell, H.C. Gledhill, S.R. Brown, and I.G. Turner. Vacuum plasma sprayed hydroxyapatite coatings on titanium alloy substrates: surface characterization and observation of dissolution processes using atomic force microscopy. *J. Vac. Sci. Technol. B*, 14:1167–1172, 1996.
- [105] E. Chang, W.J. Chang, B.C. Wang, and C.Y. Yang. Plasma spraying of zirconia-reinforced hydroxyapatite composite coatings on titanium. Part II. Dissolution behaviour in simulated body fluid and bonding degradation. *J. Mater. Sci. Mater. Med.*, 8:201–211, 1997.
- [106] C.Y. Yang, B.C. Wang, E. Chang, and B.C. Wu. Bond degradation at the plasma-sprayed HA coating/Ti₆Al₄V alloy interface: an in vitro study. *J. Mater. Sci. Mater. Med.*, 6:258–265, 1995.
- [107] J.G.C. Wolke, K. de Groot, and J.A. Jansen. Dissolution and adhesion behaviour of radio-frequency magnetron-sputtered Ca-P coatings. *J. Mater. Sci.*, 33:3371–3376, 1998.
- [108] E.Y. Kawachi, C.A. Bertran, and L.T. Kubota. Interface potential of calcium phosphate in simulated body fluid. *Biomaterials*, 19:2329–2333, 1998.
- [109] K. Hata and T. Kokubo. Growth of a bonelike apatite layer on a substrate by a biomimetic process. *J. Am. Ceram. Soc.*, 78:1049–1053, 1995.
- [110] H.-M. Kim, K. Kishimoto, F. Miyaji, T. Kokubo, T. Yao, Y. Suetsugu, J. Tanaka, and T. Nakamura. Composition and structure of the apatite formed on PET substrates in

- SBF modified with various ionic activity products. *J. Biomed. Mat. Res.*, 46:228–235, 1999.
- [111] P. Li, I. Kangasniemi, K. de Groot, and T. Kokubo. Bonelike hydroxyapatite induction by a gel-derived titania on a titanium substrate. *J. Am. Ceram. Soc.*, 77:1307–1312, 1994.
- [112] J. Li, H. Liao, and M. Sjöström. Characterization of calcium phosphates precipitated from simulated body fluid of different buffering capacities. *Biomaterials*, 18:743–747, 1997.
- [113] F. Miyaji, H.-M. Kim, S. Handa, T. Kokubo, and T. Nakamura. Bonelike apatite coating on organic polymers: novel nucleation process using sodium silicate solution. *Biomaterials*, 20:913–919, 1999.
- [114] J.L. Ong, L.C. Lucas, G.N. Raikar, R. Connatser, and J.C. Gregory. Spectroscopic characterization of passivated titanium in a physiologic solution. *J. Mater. Sci. Mater. Med.*, 6:113–119, 1995.
- [115] J.L. Ong, G.N. Raikar, and T.M. Smoot. Properties of calcium phosphate coatings before and after exposure to simulated biological fluid. *Biomaterials*, 18:1271–1275, 1997.
- [116] M.T. Pham, W. Matz, H. Reuther, E. Richter, and G. Steiner. Hydroxyapatite nucleation on Na ion implanted Ti surfaces. *J. Mater. Sci. Let.*, 19:1029–1031, 2000.
- [117] M.T. Pham, M.F. Maitz, W. Matz, H. Reuther, E. Richter, and G. Steiner. Promoted hydroxyapatite nucleation on titanium ion-implanted with sodium. *Thin Solid Films*, 379:50–56, 2000.
- [118] A.C. Tas. Synthesis of biomimetic Ca-hydroxyapatite powders at 37°C in synthetic body fluids. *Biomaterials*, 21:1429–1438, 2000.
- [119] P.E. Wang and T.K. Chaki. Hydroxyapatite films on silicon single crystals by a solution technique: texture, supersaturation and pH dependence. *J. Mater. Sci. Mater. Med.*, 6:94–104, 1995.
- [120] H.B. Wen, J.G.C. Wolke, J.R. de Wijn, Q. Liu, F.Z. Cui, and K. de Groot. Fast precipitation of calcium phosphate layers on titanium induced by simple chemical treatments. *Biomaterials*, 18:1471–1478, 1997.
- [121] J. Weng, Q. Liu, J.G.C. Wolke, X. Zhang, and K. de Groot. Formation and characteristics of the apatite layer on plasma-sprayed hydroxyapatite coatings in simulated body fluid. *Biomaterials*, 18:1027–1035, 1997.
- [122] W.-Q. Yan, T. Nakamura, K. Kawanabe, S. Nishigochi, M. Oka, and T. Kokubo. Apatite layer-coated titanium for use as bone bonding implants. *Biomaterials*, 18:1185–1190, 1997.
- [123] L.C. Feldman and J.W. Mayer. *Fundamentals of Surface and Thin Film Analysis*. Elsevier Science Publishers B.V., Amsterdam, The Netherlands, 1986.
- [124] J.R. Tesmer and M. Nastasi. *Handbook of Modern Ion Beam Analysis*. Materials Research Society, 1995.
- [125] W.M. Arnold Bik and F.H.P.M. Habraken. Elastic recoil detection. *Rep. Prog. Phys.*, 56:859–902, 1993.
- [126] L.R. Doolittle. A semiautomatic algorithm for Rutherford backscattering analysis. *Nucl.*

- Instr. Meth. in Phys. Res. B*, 15:227–234, 1986.
- [127] J.F. Ziegler, J.P. Biersack, and U. Littmark. *The Stopping and Range of Ions in Solids*. Pergamon, New York, 1985.
- [128] J.F. Ziegler. Ziegler90. Stopping power tables contained in TRIM90. Corrected stopping powers based on Ziegler85, 1990.
- [129] H. Timmers, T.R. Ophel, and R.G. Elliman. Simplifying position-sensitive gas-ionization detectors for heavy ion elastic recoil detection. *Nucl. Instr. Meth. in Phys. Res. B*, 161-163:19–28, 2000.
- [130] H.C. van de Hulst. *Light Scattering by Small Particles*. Structure of Matter. John Wiley and Sons, Inc., New York, 1957.
- [131] P.A. Ngankam, P. Schaal, J.-C. Voegel, and F.J.G. Cuisinier. Heterogeneous nucleation of calcium phosphate salts at a solid/liquid interface examined by scanning angle reflectometry. *J. Crystal Growth*, 197:927–938, 1999.
- [132] F. Brunet, D.R. Allan, S.A.T. Redfern, R.J. Angel, R.Miletich, H.J. Reichmann, J. Sergeant, and M. Hanfland. Compressibility and thermal expansivity of synthetic apatites, $\text{Ca}_5(\text{PO})_3\text{X}$ with $\text{X} = \text{OH}, \text{F}$ and Cl . *Eur. J. Mineral.*, 11:1023–1035, 1999.
- [133] E.D. Eanes and J.L Meyer. The maturation of crystalline calcium phosphates in aqueous suspensions at physiologic pH. *Calc. Tiss. Res.*, 23:259–269, 1977.
- [134] D.L. Parkhurst and C.A.J. Appelo. User's guide to PHREEQC (version 2). A computer program for speciation, batch-reaction, one-dimensional transport, and inverse geochemical calculations. Technical Report 99-4259, 310, U.S. Geological Survey, 1999.
- [135] S.R. Charlton and D.L. Parkhurst. PhreeqcI – A graphical user interface to the geochemical model PHREEQC. Technical Report FS-031-02, 2 p, U.S. Geological Survey, 2002.
- [136] A.H. Truesdell and B.F. Jones. WATEQ, a computer program for calculating chemical equilibria of natural waters. *U.S. Geological Survey, Journal of Research*, 2:233–274, 1974.
- [137] A.M. Hartley, W.A. House, M.E. Callow, and B.S.C. LeadBeater. Coprecipitation of phosphate with calcite in the presence of photosynthesizing green algae. *Wat. Res.*, 31:2261–2268, 1997.
- [138] W. Ostwald. Studie über die Bildung und Umwandlung fester Körper. *Zeit. Physik. Chem.*, 22:289–330, 1897.
- [139] R. Boistelle and J.P. Astier. Crystallization mechanisms in solution. *J. Crystal Growth*, 90:14–30, 1988.
- [140] W.E. Brown and L.C. Chow. Thermodynamics of apatite crystal growth and dissolution. *J. Crystal Growth*, 53:31–41, 1981.
- [141] M. Iijima, H. Kamemizu, N. Wakamatsu, T. Goto, Y. Doi, and Y. Moriwaki. Precipitation of octacalcium phosphate at 37°C and at pH 7.4: in relation to enamel formation. *J. Crystal Growth*, 112:467–473, 1991.
- [142] W. White and G.H. Nancollas. Quantitative study of enamel dissolution under conditions of controlled hydrodynamics. *J. Dent. Res.*, 56:524–530, 1977.

- [143] V.E. Levich, editor. *Physicochemical Hydrodynamics*. Prentice Hall, Englewood Cliffs, New Jersey, 1962.
- [144] J. Zhang and G.H. Nancollas. Dissolution deceleration of calcium phosphate crystals at constant undersaturation. *J. Crystal Growth*, 123:59–68, 1992.
- [145] A.G. Walton. *The Formation and Properties of Precipitates*, volume 23 of *Chemical Analysis, a Series of Monographs on Analytical Chemistry and its Applications*. Interscience Publishers, John Wiley and Sons, New York/London/Sydney, 1967.
- [146] A.E. Nielsen. *Kinetics of Precipitation*, volume 18 of *International Series of Monographs on Analytical Chemistry*. Pergamon Press, 1964.
- [147] S. Lazić and Z. Vukovic. Ion exchange of strontium on synthetic hydroxyapatite. *J. Radioanal. Nucl. Chem.*, 149:161–168, 1991.
- [148] W. Wu and G.H. Nancollas. Nucleation and growth of octacalcium phosphate on titanium oxide surfaces. *Langmuir*, 13:861–865, 1997.
- [149] L.C. Bell, A.M. Posner, and J.P. Quirk. The point of zero charge of hydroxyapatite and fluorapatite in aqueous solutions. *J. Colloid Interface Sci.*, 42:250–261, 1973.
- [150] S. Chander and D.W. Fuerstenau. Interfacial properties and equilibria in the apatite-aqueous solution system. *J. Colloid Interface Sci.*, 70:507–516, 1979.
- [151] R.O. James and T.W. Healy. Adsorption of hydrolyzable metal ions at the oxide-water interface. *J. Colloid Interface Sci.*, 40(1):42–81, 1972.
- [152] P. Somasundaran and Y.H.C. Wang. *Adsorption on and Surface Chemistry of Hydroxyapatite*, chapter Surface Chemical Characteristics and Adsorption Properties of Apatite, pages 129–149. Plenum Press, New York, 1984.
- [153] L. Wu, W. Forsling, and P.W. Schindler. Surface complexation of calcium minerals in aqueous solution: 1. Surface protonation at fluorapatite-water interfaces. *J. Colloid Interface Sci.*, 147:178–185, 1991.
- [154] L. Wu and W. Forsling. Surface complexation of calcium minerals in aqueous solution: 3. Ion exchange and acid-base properties of hydrous fluorite surfaces. *J. Colloid Interface Sci.*, 174:178–184, 1995.
- [155] C.C. Chusuei, D.W. Goodman, D.R. Justes M.J. Van Stipdonk, and E.A. Schweikert. Calcium phosphate phase identification using XPS and time-of-flight cluster SIMS. *Ann. Chem.*, 71:149–153, 1999.
- [156] G.W. Simmons and B.C. Beard. Characterization of acid-based properties of the hydrated oxides on iron and titanium metal surfaces. *J. Phys. Chem.*, 91:1143–1148, 1987.
- [157] D.N. Misra. Interaction of some coupling agents and organic compounds with hydroxyapatite: hydrogen bonding, adsorption and adhesion. *J. Adhesion Sci. Technol.*, 8:87–99, 1994.
- [158] S. Lazić. Microcrystalline hydroxyapatite formation from alkaline solutions. *J. Crystal Growth*, 147:147–154, 1995.
- [159] A. Lebugle, B. Sallek, and A. Tai Tai. Surface modification of monetite in water at 37°C: characterisation by XPS. *J. Mater. Chem.*, 9:2511–2515, 1999.
- [160] R.A. Griffin and J.J. Jurinak. The interaction of phosphate with calcite. *Soil Sci. Soc. Am. Proc.*, 37:847–850, 1973.

- [161] F. Monteil-Rivera, M. Fedoroff, J. Jeanjean, L. Minel, M. Barthes, and J. Dumonceau. Sorption of selenite (SeO_3^{2-}) on hydroxyapatite: an exchange process. *J. Colloid Interface Sci.*, 221:291–300, 2000.
- [162] M.A. Anderson and A.J. Rubin, editors. *Adsorption of Inorganics at Solid-Liquid Interfaces*. Ann Arbor Science, 1981.
- [163] A. Kitahara and A. Watanabe, editors. *Electrical Phenomena at Interfaces: Fundamentals, Measurements, and Applications*. Dekker, New York, 1984.
- [164] C.P. Huang, C.R. O'Melia, and J.J. Morgan, editors. *Aquatic Chemistry: Interfacial and Interspecies Processes*, volume 244 of *Advances in Chemistry Series*. American Chemical Society, Washington D.C., 1995.
- [165] R.Z. LeGeros. *Tooth enamel IV : Proceedings of the Fourth International Symposium on the Composition, Properties and Fundamental Structure of Tooth Enamel*, chapter Incorporation of Magnesium in Synthetic and in Biological Apatites, pages 32–36. Elsevier, Amsterdam, 1984.
- [166] E.D. Eanes and S.L. Rattner. The effect of magnesium on apatite formation in seeded supersaturated solutions at pH =7.4. *J. Dent. Res.*, 60:1719–1723, 1981.
- [167] J. Christoffersen, M.R. Christoffersen, W. Kibaczyc, and F.A. Andersen. A contribution to the understanding of the formation of calcium phosphates. *J. Crystal Growth*, 94:767–777, 1989.
- [168] J.C. Heughebaert and G.H. Nancollas. Mineralization kinetics: the role of octacalcium phosphate in the precipitation of calcium phosphates. *Colloids Surf.*, 9:89–93, 1984.
- [169] M.S.-A. Johnsson and G.H. Nancollas. The role of brushite and octacalcium phosphate in apatite formation. *Critical Reviews in Oral Biology and Medicine*, 3:61–82, 1992.
- [170] G.H. Nancollas. The involvement of calcium phosphates in biological mineralization and demineralization processes. *Pure & Appl. Chem.*, 64:1673–1678, 1992.
- [171] A.T.-C. Wong and J.T. Czernuszka. Transformation behaviour of calcium phosphate 1. Theory and modelling. *Colloids and Surfaces A: Physicochemical and Engineering Aspects*, 78:245–253, 1993.
- [172] J.E. Aubin. Bone stem cells. *J. Cell. Biochem. Suppls*, 30/31:73–82, 1998.
- [173] P. Bianco, M. Riminucci, S. Gronthos, and P. Gehron Robey. Bone marrow stromal cells: nature, biology and potential applications. *Stem Cells*, 19:180–192, 2001.
- [174] C. Maniopoulos, J. Sodek, and A.H. Melcher. Bone formation in vitro by stromal cells obtained from bone marrow of young adult rats. *Cell Tissue Res.*, 254:317–330, 1988.
- [175] V.L. Singer, L.J. Jones, S.T. Yue, and R.P. Haugland. Characterization of PicoGreen reagent and development of a fluorescence-based solution assay for double-stranded DNA quantitation. *Anal. Biochem.*, 249:228–238, 1997.
- [176] R.Z. McComb, G.N. Bowers, and S. Posen. *Alkaline Phosphatase*, volume 15. Plenum Press, New York, 1979.
- [177] S. Kasugai, R. Todescan, T. Nagata, K.L. Yao, W.T. Butler, and J. Sodek. Expression of bone-matrix proteins associated with mineralized tissue formation by adult rat bone-marrow cells in vitro - inductive effects of dexamethasone on the osteoblastic phenotype. *J. Cell. Physiol.*, 147:111–120, 1991.

- [178] K. Flade, C. Lau, M. Mertig, and W. Pompe. Osteocalcin-controlled dissolution-precipitation of calcium phosphate under biomimetic conditions. *Chem. Mater.*, 13:3596–3602, 2001.
- [179] A.J. Lee, S. Hodges, and R. Eastell. Measurement of osteocalcin. *Ann. Clin. Biochem.*, 37:432–446, 2000.
- [180] H.J. Gitelman. An improved automated procedure for the determination of calcium in biological specimens. *Anal. Biochem.*, 18:521–531, 1967.
- [181] T.A. Owen, M. Aronow, V. Shalhoub, L.M. Barone, L. Wilming, M.S. Tassinari, M. Kennedy, S. Pockwinse, J.B. Lian, and G.S. Stein. Progressive development of the rat osteoblast phenotype in vitro: reciprocal relationships in expression of genes associated with osteoblast proliferation and differentiation during formation of the bone extracellular matrix. *J. Cell. Physiol.*, 143:420–430, 1990.
- [182] S.C. Dieudonne, J. van den Dolder, J.E. de Ruijter, H. Paldan, T. Peltola, M. van 't Hof, R.P. Happonen, and J.A. Jansen. Osteoblast differentiation of bone marrow stromal cells cultured on silica gel and sol-gel-derived titania. *Biomaterials*, 23:3041–3051, 2002.
- [183] A.D. McNaught and A. Wilkinson. *Compendium of Chemical Terminology: IUPAC Recommendations (The IUPAC 'Gold Book')*. Blackwell Science, Oxford, UK, 1997.

Summary

Calcium phosphate (CaP) ceramics are known for their excellent bone-bonding properties and corrosion resistance when used as an implant material. A property often observed with bioactive, i.e., bone inducing, biomaterials is the formation of a directly bonded CaP precipitate. In this work we have investigated the physicochemical interactions between thin (~ 100 nm) RF-sputtered CaP coatings and simulated physiological environments. Especially, the formation of CaP crystals at the surface of these coatings was studied, both in simulated body fluids and in a rat bone-marrow (RBM) cell-model.

In the first part of this thesis we introduced the RF-sputter technique and characterized the applied coatings that were used throughout this work. Using RF magnetron sputtering it is possible to produce thin, dense, homogeneous, and well-adhering CaP coatings on polished silicon (100) substrates. A heat treatment of 30 minutes at 650°C was applied to crystallize the coatings in an apatite structure. It was observed that only in a small range of process-parameters (sputter power, coating thickness, and anneal temperature) stable coatings could be produced that did not delaminate. Coatings with a graded Ca/P ratio could be obtained by varying the sputter power over two sputter targets with different compositions. Variation of the bulk composition of the coating controls the surface composition. A heat treatment does not change the surface composition.

As-deposited coatings are amorphous and dissolve in Kokubo's simulated body fluid (SBF), a solution with the same ionic concentrations as human blood plasma, but without any organic additives. Also in more concentrated SBF (SBF_x, which is SBF with x times the Ca and PO₄ concentrations) like SBF₂ the coatings were found to dissolve. The CaP coatings dissolve stoichiometrically and with a constant rate of $4.3 \cdot 10^{15}$ at./cm² min⁻¹ in SBF₁ and $0.70 \cdot 10^{15}$ at./cm² min⁻¹ in SBF₂. The dissolution process is diffusion-limited in both SBF₁ and SBF₂ at room temperature.

Heat-treated CaP coatings remain inert for days when immersed in SBF. Within a

Ca/P range of 1.4 to 3, these coatings show the formation of a CaP precipitate when immersed in SBF_x with $x > 1.4$ for several hours. At room temperature the formation of these CaP crystals is preceded by an induction period of 40-60 minutes during which almost no apposition of CaP is found. After this induction period, growth of the CaP crystals is possible in both SBF_2 and SBF_1 . Immersion in SBF_2 of other RF-sputtered ceramics, like Al_2O_3 , TiO_2 , and SiO_2 , did not result in the formation of a CaP precipitate.

Within minutes after immersion, rod-shaped CaP sediments of ~ 100 nm from the solution were found to adhere on the coating surface (with a coverage of $26 \cdot 10^{15}$ at./ cm^2). It was found that these sediments are not formed at the CaP surface upon immersion, but are already present in the SBF_2 . No sediments are found when coatings are immersed in SBF_1 . Immersion of coatings in SBF_2 diluted to SBF_1 also did not show any deposits and thus revealed the dynamical dissolution and formation of these particles. During the induction period sediments were found to agglomerate and evolve to a more sheetlike shape.

The length of the induction period depends strongly on the temperature of the solution. The presence of an induction period can be explained in terms of classical nucleation. By measuring the induction time at different temperatures an activation energy for the formation of CaP nuclei could be estimated. Only after completion of the induction period growth is possible in SBF_1 .

The growth rate after the induction period is $\sim 12 \cdot 10^{15}$ at./ $\text{cm}^2 \text{ min}^{-1}$ in SBF_2 and $0.16 \cdot 10^{15}$ at./ $\text{cm}^2 \text{ min}^{-1}$ in SBF_1 . Further, growth in SBF_1 and SBF_2 is likely to be controlled by surface processes. Orientation of the coatings in the solution does not influence the formation of growth of the crystals.

Upon immersion, the first interaction between CaP coatings and simulated body fluids will be the adsorption of ions from the solution. It is the coating surface combined with the adsorption layer that determines the surface chemistry of the material. By the use of low energy ion scattering (LEIS) and by radioactive labeling of the SBFs, the composition of the adsorption layer on CaP coatings was investigated. The initial adsorption process is rapid (within a minute). For CaP coatings with a high Ca/P ratio (~ 1.6), the Ca coverage in the adsorption layer was determined to be $(1.15 \pm 0.16) \cdot 10^{15}$ ions/ cm^2 , the PO_4 coverage $(0.93 \pm 0.13) \cdot 10^{15}$ ions/ cm^2 , and the Ca/P ratio 1.24 ± 0.02 . For CaP coatings with a low Ca/P ratio (~ 0.8), the Ca coverage in the adsorption layer was $(0.54 \pm 0.14) \cdot 10^{15}$ ions/ cm^2 , the PO_4 coverage $(0.25 \pm 0.05) \cdot 10^{15}$ ions/ cm^2 , and the Ca/P ratio 2.17 ± 0.10 . Thus, we see that the Ca/P ratio of the adsorption layer is inversely related to the Ca/P ratio of the coating surface. From immersion studies in SBF_2 we found that the coatings with a high Ca/P ratio showed the formation of a precipitate within two hours, whereas the coatings with a low ratio did not. We found that the adsorption of ions is highly reversible. Further, the effect of adsorption by sediments attached to the surface is limited.

A mechanism proposed to explain the formation of CaP crystals on CaP coatings involves the dissolution and subsequent reprecipitation of coating species. It was suggested that dissolution of ions from the coating would temporarily increase the ion

concentration in the diffusive layer, resulting in the precipitation of new and more stable CaP crystals. By labeling the surface with radioactive Ca and PO₄ isotopes, we were able to show that a maximum of 2% of the surface Ca and PO₄ species is dissolved during the induction period preceding crystal formation, and showed that the mechanism inducing crystal formation does not involve desorption and reprecipitation of coating species.

In the last chapter of this thesis, the cytocompatibility of RF-sputtered coatings was addressed. Thin films of CaP, TiO₂, and Al₂O₃ were compared in a rat bone-marrow (RBM) cell-culture study. In contrast to CaP, both TiO₂ and Al₂O₃ are known to be bioinert. However, there is still discussion on the biocompatibility of TiO₂. It was found that cell behavior on CaP coatings significantly differed from Al₂O₃. CaP coatings showed decreased early proliferation, increased differentiation, and increased mature osteoblast activity compared to Al₂O₃. Results for TiO₂ were intermediate compared to CaP and Al₂O₃. That is, early proliferation followed the Al₂O₃ results, whereas the mature osteoblast activity and the matrix production confirmed the CaP findings.

From day 8-12 on, cells start differentiating towards mature, extracellular matrix (ECM) forming osteoblasts. The ECM consists of bundles of collagen fibers that are calcified with globular CaP accretions. Coinciding, both the CaP and TiO₂ coatings showed the formation of a directly bonded CaP layer (~1 μm after 16 days), quite similar to the precipitate grown in simulated body fluids. The formation and growth of this layer is cell mediated. This layer was absent on the Al₂O₃ surface. The directly bonded CaP layer is thought to be indicative of bone-bonding bioactivity.

In simulated body fluids we showed that the presence of CaP nuclei, obtained by 40-60 minutes pre-immersion in SBF₂, is required to allow growth in SBF₁. Therefore, we also studied the effect of pre-immersion in a RBM cell-model. The coatings that were not pre-immersed showed the formation of a directly bonded CaP layer after about 8 days, again after the start of osteoblast-differentiation. However, the pre-immersed samples allowed the growth of a this layer without an offset. Thus by applying CaP nuclei, the formation of the directly bonded CaP layer has been decoupled from the ECM calcifications.

Samenvatting

Van calciumfosfaat (CaP) keramiek is bekend dat het uitstekende bot-hechttings eigenschappen vertoont en corrosie bestendig is wanneer het gebruikt wordt als een implantaat materiaal. Een eigenschap die vaak wordt waargenomen bij bioactieve, d.w.z. bot-inducerende, biomaterialen is de vorming van een direct gebonden calciumfosfaat laag. In dit werk hebben we de fysisch-chemische interacties onderzocht tussen dunne (~ 100 nm) RF-gesputterde calciumfosfaat coatings en nagebootste fysiologische omgevingen. In het bijzonder, de vorming van CaP kristallen aan het oppervlak van deze coatings is bestudeerd, zowel in gesimuleerde lichaamsvloeistof (SBF) als in een rattenbeenmerg celmodel.

In het eerste deel van dit proefschrift introduceren we de RF-sputter techniek en karakteriseren we de aangebrachte coatings die in dit werk worden gebruikt. RF magnetron sputterdepositie maakt het mogelijk om dunne, compacte, homogene en goed hechtende CaP coatings op gepolijste silicium (100) substraten aan te brengen. Een hitte behandeling van 30 minuten bij 650°C werd gebruikt om de coatings te kristalliseren en een apatiet structuur te verkrijgen. Alleen binnen een klein bereik van procesparameters (sputter vermogen, coating dikte en temperatuur van de hitte-behandeling) kunnen stabiel coatings worden geproduceerd die niet loslaten. Coatings met verschillende Ca/P verhoudingen kunnen gemaakt worden door het sputtervermogen te variëren over twee sputter-targets van verschillende samenstelling. Variatie van de bulk compositie reguleert de samenstelling van het oppervlak. Een hitte-behandeling verandert de samenstelling van het oppervlak niet.

Direct na het aanbrengen van de coatings zijn deze amorf en lossen ze op in Kokubo's gesimuleerde lichaamsvloeistof (SBF), een oplossing met dezelfde ionenconcentraties als menselijk bloed plasma maar zonder enige organische toevoegingen. Ook in meer geconcentreerde SBF (SBF_x , dit is SBF met x maal de Ca en PO_4 concentraties) zoals SBF_2 lossen de coatings op. De CaP coatings lossen stoichiome-

trisch op en met een constante oplosnelheid van $4.3 \cdot 10^{15}$ at./cm² min⁻¹ in SBF₁ en $0.70 \cdot 10^{15}$ at./cm² min⁻¹ in SBF₂. Bij kamertemperatuur is de oplosnelheid in zowel SBF₁ als SBF₂ diffusie-bepaald.

Hitte-behandelde CaP coatings blijven dagenlang inert als ze in de SBF gedompeld worden. Op coatings met een Ca/P ratio binnen het bereik van 1.4 tot 3 zien we na enkele uren onderdompelen in SBF_x met $x > 1.4$, de vorming van een CaP neerslag. Bij kamertemperatuur wordt de vorming van deze CaP kristallen voorafgegaan door een inductieperiode van 40-60 minuten, waarin nauwelijks afzetting van CaP wordt gevonden. Na deze inductieperiode is groei mogelijk in zowel SBF₂ als SBF₁. Het onderdompelen van andere RF-gesputterde keramieken zoals Al₂O₃, TiO₂ en SiO₂, resulteert niet in de vorming van een CaP neerslag.

Binnen enkele minuten na het onderdompelen van de coatings hechten zich staafvormige CaP sedimenten van ~ 100 nm uit de vloeistof aan het coating oppervlak (met een bedekking van $26 \cdot 10^{15}$ at./cm²). Deze sedimenten worden niet aan het coating oppervlak gevormd bij het onderdompelen, maar zijn al aanwezig in de SBF₂. Op coatings gedompeld in SBF₁ werden geen sedimenten gevonden. Wanneer coatings worden ondergedompeld in tot SBF₁ aangelengde SBF₂, worden ook geen sedimenten gevonden. Dit geeft aan dat de sedimenten bijzonder dynamisch gevormd worden en weer oplossen. Tijdens de inductieperiode klitten de sedimenten samen en nemen een meer plaatachtige vorm aan.

De lengte van de inductieperiode hangt sterk af van de temperatuur van de oplossing. De aanwezigheid van een inductieperiode kan worden verklaard in termen van klassieke nucleatie. Door het meten van de inductietijd bij verschillende temperaturen kan een schatting worden gemaakt van de activeringsenergie voor de vorming van CaP nuclei. Slechts na het voltooien van de inductieperiode is groei mogelijk in SBF₁.

De groeisnelheid na de inductieperiode is $\sim 12 \cdot 10^{15}$ at./cm² min⁻¹ in SBF₂ en $0.16 \cdot 10^{15}$ at./cm² min⁻¹ in SBF₁. De groei in SBF₁ en SBF₂ wordt waarschijnlijk gecontroleerd door oppervlakte processen. De vorming of de groei van de kristallen wordt niet beïnvloed door de oriëntatie van de coatings in de oplossing.

Wanneer een CaP coating wordt ondergedompeld in een gesimuleerde lichaamsvloeistof, zullen er als eerste ionen uit de oplossing adsorberen aan het coatingoppervlak. De combinatie van het coatingoppervlak en de geadsorbeerde vloeistoflaag bepalen de oppervlaktechemie van het materiaal. Door gebruik te maken van lage energie ionenverstrooiing (LEIS) en door het radioactief labelen van de SBFs, kon de samenstelling van de adsorptielaag op de CaP coatings worden onderzocht. In de adsorptielaag op CaP coatings met een hoge Ca/P ratio (~ 1.6) bedraagt de Ca bedekking $(1.15 \pm 0.16) \cdot 10^{15}$ ions/cm², de PO₄ bedekking $(0.93 \pm 0.13) \cdot 10^{15}$ ions/cm², en de Ca/P ratio 1.24 ± 0.02 . Voor de adsorptielaag op CaP coatings met een lage Ca/P verhouding (~ 0.8) vonden we een Ca bedekking van $(0.54 \pm 0.14) \cdot 10^{15}$ ions/cm², een PO₄ bedekking van $(0.25 \pm 0.05) \cdot 10^{15}$ ions/cm², en een Ca/P ratio van 2.17 ± 0.10 . We zien dat de Ca/P ratio van de adsorptielaag een inverse relatie heeft met de Ca/P ratio van het coating oppervlak. Uit experimenten in SBF₂ bleek dat de coatings met een hoge Ca/P ratio wel binnen twee uur een neerslag laten zien van CaP kristallen, terwijl

coatings met een lage Ca/P ratio inert blijven. De adsorptie van ionen is reversibel. Verder bleek dat het effect van sedimenten op de adsorptie van ionen beperkt is.

Eén van de mechanismen die is voorgesteld om de vorming van CaP kristallen op CaP coatings te verklaren omvat het oplossen en vervolgens weer neerslaan van ionen uit de coating. Deze ionen zouden in oplossing gaan en tijdelijk de ionenconcentraties in de diffusielaag verhogen. Dit zou de neerslag induceren van nieuwe, meer stabiele CaP kristallen. Door het labelen van het oppervlak met radioactieve Ca en PO₄ isotopen, lieten we zien dat maximaal 2% van de oppervlakte Ca en PO₄ groepen in oplossing gaat tijdens de inductieperiode die voorafgaat aan de vorming van kristallen. We tonen aan dat desorptie en het opnieuw neerslaan van ionen uit de coating niet verantwoordelijk zijn voor de vorming van CaP kristallen.

In het laatste hoofdstuk van dit proefschrift bestuderen we de cytocompatibiliteit van de RF-gesputterde coatings. Dunne lagen van CaP, Al₂O₃ en TiO₂ werden met elkaar vergeleken in een rattenbeenmerg celkweekexperiment. In tegenstelling tot CaP is van zowel TiO₂ als Al₂O₃ bekend dat ze bioinert zijn. Over de biocompatibiliteit van TiO₂ bestaat nog wel onduidelijkheid. We vonden dat het celgedrag op CaP coatings aanmerkelijk verschilde met Al₂O₃. CaP coatings lieten een verminderde proliferatie, een verhoogde differentiatie en een verhoogde activiteit van osteoblasten zien ten opzichte van de Al₂O₃ coatings. De resultaten voor TiO₂ liggen tussen die van CaP en Al₂O₃ in. De vroege proliferatie volgt het gedrag dat voor Al₂O₃ werd gevonden, terwijl de osteoblast activiteit overeenkomt met de CaP resultaten.

Vanaf dag 8-12 beginnen cellen te differentieren tot volgroeide osteoblasten die extracellulaire matrix (ECM) produceren. De ECM bestaat uit bundels van collageenstrengen met bolvormige calcificaties. Tegelijkertijd vormt zich op zowel de CaP als TiO₂ coatings een direct gebonden CaP laag (~1 µm na 16 dagen), die sterk lijkt op de laag die in gesimuleerde lichaamsvloeistof wordt gevormd. Het ontstaan en groeien van deze laag wordt gestuurd door cellen. Deze laag werd niet gevonden op het Al₂O₃ oppervlak. Aangenomen wordt dat de direct gebonden CaP laag indicatief voor bioactiviteit.

In gesimuleerde lichaamsvloeistoffen toonden we aan dat de aanwezigheid van nucleatiepunten, die verkregen kunnen worden door een 40-60 minuten voorbehandeling in SBF₂, vereist is om groei te bewerkstelligen in SBF₁. Om deze reden bestudeerden we ook de invloed van een dergelijke voorbehandeling in een celkweekexperiment. Op het oppervlak van de coatings die niet voorbehandeld werden vormde zich na ongeveer acht dagen een direct gebonden CaP laag, weer na de osteoblast-differentiatie. De samples die wel voorbehandeld waren lieten wel onmiddellijke groei van deze laag zien, zonder een inductietijd. Zodoende kan door het aanbrengen van CaP nucleatiepunten de vorming van een direct gebonden CaP laag worden losgekoppeld van de calcificaties van de ECM.

Dankwoord

Samenspelen is pas fijn! Dit onderzoek is alleen mogelijk geweest dankzij de input, het enthousiasme, de kritiek en gezelligheid van een grote groep mensen. Hier zou ik het bij kunnen laten, maar een aantal mensen verdient zeker een speciaal woord van dank.

Arjen, allereerst wil ik je bijzonder bedanken voor de energie die je de afgelopen jaren in mij hebt gestoken. Ik heb enorm veel van je geleerd, en van je visie op het bedrijven van wetenschap zal ik nog een leven lang plezier hebben. Ook je constructieve en altijd optimistische houding heb ik gewaardeerd.

John, bedankt voor al je inspanningen en ideeën. Je kijk op het veld van de biomaterialen heeft ook bij mij respect gewekt. Je hebt laten zien dat er in de wetenschap meer te koop is dan alleen natuurkunde. Dank ook voor de precisie, de snelheid maar vooral ook de humor waarmee je mijn ideeën en manuscript van commentaar voorzag.

Joop, je was er altijd als er weer eens experimenteel gedonder was. Bedankt ook voor je hulp bij het SEMmen en XRDen. Grenzeloos is je relativiseringsvermogen, je interesse voor persoonlijke zaken en je inzet bij een potje sumoworstelen.

Tot slot Frans, bedankt voor je interesse voor m'n werk door de jaren heen en voor je commentaar bij het manuscript. Mede door jou is de charme van het experimenteren er niet helemaal van af gegaan.

Verder gaat mijn dank ook uit naar de leden van de manuscriptcommissie, Werner van der Weg, John Kelly en Klaas de Groot voor het kritisch lezen van dit werk.

Een aantal mensen wil ik danken voor hun experimentele hulp. Arnoud Denier van der Gon voor zijn hulp met de LEIS metingen. Helaas heeft hij het voltooiën van mijn proefschrift niet meer mee kunnen maken. Verder dank ik Arnout Imhof voor de dynamische lichtverstrooiing, Theo Hey en Siewart Oldenburg voor de radionuclide experimenten en Hans Meeldijk voor de hoge resolutie elektronenmicroscopie.

Veel dank ben ik verschuldigd aan Anja de Ruijter voor alle hulp bij het uitvoe-

ren van de celexperimenten en de analyses. Je bijdrage is cruciaal geweest voor dit onderzoek.

Jan-Paul, Theo en Ruurd wil ik danken voor hun technische hulp en know-how. Ik besef dat ik af en toe best een lastige klant moet zijn geweest. Jullie oplossingen waren zonder uitzondering altijd inventief.

Bram Edens en Channah in 't Veld dank ik voor hun hulp en enthousiasme aan het begin van mijn onderzoeksperiode. Ze hebben meer dan hun deel aan experimentele moeilijkheden op hun bord gekregen.

Het voordeel van betrokken zijn in een samenwerking tussen twee onderzoeksgroepen is dat ik kennis heb kunnen maken met twee verschillende onderzoeksculturen. Ik ben altijd met ontzettend veel plezier in Nijmegen geweest. Zowel de inhoudelijke als de meer off-topic discussies heb ik erg gewaardeerd. Dus Diederik, Edwin, Frank, Harry, Henriette, Jack, Jacky, Johan, Juliette, Marijke, Martijn, Petra, Sander, Suzanne, Quinten, Olga, Weibo en Yonggang, bedankt voor de gezelligheid.

Maar ook in Utrecht was het natuurlijk goed toeven. Alberto, Eddy, Jeroen, Marlijn, Mirela, Nicolae, Pedro, Renée, Sander, Tonnis, Yurii, bedankt! Wim, bedankt voor al die dingen die je me in de jaren hebt bijgebracht m.b.t. signaalverwerking en ionenbundels. De rest van de groep Surfaces, Interfaces and Devices wil bedanken voor de leuke sfeer tijdens koffiepauzes en lunches. Riny, bedankt voor de (mentale) ondersteuning.

De versnellergroep wil ik bedanken voor alle bundels en hun grote flexibiliteit: Henk, Gerard, Ruud en in het bijzonder Flip voor al zijn 3 MV werk. Alle medewerkers van de Wetenschapswinkel Natuurkunde bedank ik voor de gezellige uurtjes.

For my short but productive stay at the University of Technology, Sydney I want to thank Besim Ben-Nissan and his group for their hospitality.

Bas is al deze jaren mijn *partner in crime* geweest. De brainstormsessies, uitjes in Nijmegen, gemiste treinen en pizza in het sputterapparaat, ik zal ze niet vlug vergeten. Jammer dat je niet bij de promotie kan zijn, maar ik hoop dat Ellen en jij een geweldige tijd in Zuid-Amerika zullen hebben.

Voor de gezellige uurtjes en de potjes bier de afgelopen jaren bedank ik Arthur, Bruno, P.B., Albert, Jasper, Job, Jurriaan, Marcel, René, Edo en Plien, de honkballers en iedereen die hier ook bij had moeten staan.

En ja, het blijft toch je familie. . . Paps en mams bedankt voor het SVR-gevoel, Peter en Sas voor het 180-gevoel, Richard en Marie-Louise voor het (G/g)amma-gevoel, Jorinde en Roald voor het wasabi-gevoel, Martijn en Jenny voor het la-la-la-student-gevoel en Wim en Marijke voor het bienvenue-en-france-gevoel. Wim, bedankt voor je interesse en het minutieus doorspitten van het manuscript. Peter, bedankt voor je creatieve input bij het ontwerpen van de kaft.

De laatste zin in een dankwoord is traditioneel voor datgene dat echt belangrijk is in je leven. Dus Sil, bedankt voor alles wat je bent. Zonder jou had ik dit niet kunnen doen, daarom is deze voor jou. . .

Curriculum Vitae

Edwin van der Wal werd op 1 november 1972 geboren in Bennekom, gemeente Ede. In 1991 behaalde hij zijn VWO diploma aan het Wageningse Lyceum te Wageningen. Aansluitend begon hij de studie natuurkunde aan de Universiteit Utrecht. In 1993 haalde hij het propedeutisch examen en het doctoraalprogramma Experimentele Natuurkunde. Tijdens zijn doctoraal volgde hij bijvakken op het gebied van atoomfysica en computationele fysica. Het afstudeeronderzoek werd uitgevoerd in de sectie grenslaagfysica van het Debye instituut, en afgerond met een scriptie getiteld: 'Hydrogen storage in thin FeTi/Pd bilayers'. In augustus 1998 werd het doctoralexamen afgelegd met het judicium 'met genoegen'.

Vanaf oktober 1998 was Edwin aangesteld als onderzoeker in opleiding binnen het STW project 'Regeneratieve Bot Implantaten'. Het project was een samenwerkingsverband tussen de afdeling Biomaterialen van de medische faculteit van de Katholieke Universiteit Nijmegen en de groep 'Surfaces Interfaces and Devices' van het Debye Instituut waar Edwin zijn standplaats had. De resultaten van het verrichte onderzoek werden op diverse internationale conferenties gepresenteerd en hebben geleid tot dit proefschrift. Tijdens zijn promotie periode is Edwin werkzaam geweest bij de Wetenschapswinkel Natuurkunde op het gebied van Geluid en Trillingen, en begeleidde hij computerpractica voor eerste- en tweedejaars natuurkundestudenten.

Notations

RF	Radio frequency	16
CaP	Calcium phosphate	9
CaP _{bulk}	Bulk CaP : a thick $\sim 2 \mu\text{m}$ CaP coating	102
CaP _{vir}	Virgin CaP coating, i.e., not pretreated	109
PT	Pretreatment, usually 1-2 hours in SBF ₂ at room temperature	53
CaP _{pre}	Pretreated CaP coating, refer to PT	109
CaP _{high}	CaP coating with a high Ca/P ratio of ~ 1.6	81
CaP _{low}	CaP coating with a low Ca/P ratio of ~ 0.8	81
IAP	Ion activity product	37
K _{sp}	Solubility product	37
SI	Saturation index	37
S	Solubility	37
EDL	Electrical double layer	74
GCSG	Gouy-Chapman-Stern-Graham model for the EDL	74
IHP	Inner Helmholtz plane	75
OHP	Outer Helmholtz plane	75
HBP	Human blood plasma	17
SBF	Simulated body fluid according to Kokubo	17
SBF ₁	SBF with the normal Ca and PO ₄ concentrations	22
SBF ₂	SBF with twice the Ca and PO ₄ concentrations	22
SBF _x	SBF with x times the Ca and PO ₄ concentrations	22
SBF*	SBF labeled with radionuclides	79
Ca-stock	Calcium stock solution for the preparation of SBFs	22
P-stock	PO ₄ stock solution for the preparation of SBFs	22
SBF ₁ -s	SBF ₁ supplement for the preparation of SBF ₁ from stock solutions	22

HAP	Hydroxyapatite	13
OCF	Octacalcium phosphate	13
TCP	Tricalcium phosphate	13
TTCP	Tetracalcium phosphate	13
DCPD	Dicalcium phosphate dihydrate	13
DCPA	Dicalcium phosphate anhydrate	13
MCPM	Monocalcium phosphate monohydrate	13
MCPA	Monocalcium phosphate anhydrate	13
CDHA	Calcium deficient hydroxyapatite	13
ACP	Amorphous calcium phosphate	13
pyro	Calcium pyrophosphate	13
XRD	X-ray diffraction	29
SEM	Scanning electron microscopy	52
EDX	Energy dispersive X-ray spectrometry	105
IBA	Ion beam analysis	23
RBS	Rutherford backscattering spectrometry	23
ERD	Elastic recoil detection	23
SLS	Static light scattering	26
XPS	X-ray photoelectron spectroscopy	88
LEIS	Low energy ion scattering	77
LSC	Liquid scintillation counting	78
BMSC	Bone mesenchymal stem cell	96
RBM	Rat bone marrow	98
ECM	Extracellular matrix	12
α -MEM	α minimal essential medium	98
PBS	Phosphate buffered saline	98
ELISA	Enzyme-linked immunosorbent assay	99
ALP	Alkaline phosphatase	99
OCPC	Ortho-cresolphthalein complexone	99
CTE	Coefficient of thermal expansion	35
SIE	Spectral index of external standard	80
t_{infl}	Inflection time	28
τ	Induction time	51
PHREEQC	Computer code for speciation calculations	38
RUMP	Computer code for IBA spectrum simulation	25

